TERNARY ALLOY NANOPARTICLES FOR POLYMER ELECTROLYTE FUEL CELL ELECTROCATALYSIS

By

James Stewart Walker

A thesis submitted to the University of Birmingham for the degree of

DOCTOR OF PHILOSOPHY

Centre for Hydrogen and Fuel Cell Research

School of Chemical Engineering

College of Engineering and Physical Sciences

University of Birmingham

February 2020

Abstract

The commercialisation of polymer electrolyte fuel cells has been slow, despite the potential role that they could play in the global energy transition that is underway. The economic viability of these fuel cells has been limited by the expensive catalysts used in their electrodes, which are typically composed of platinum metal nanoparticles. Significant research effort has been devoted to developing novel catalysts with reduced platinum content, often through alloying platinum with cheaper metals.

This work concerns methods developed to prepare novel catalyst nanoparticles composed of varying mixtures of ruthenium, selenium and platinum. Further, this report elaborates on subsequent efforts to characterise those nanoparticles physically and chemically, to understand how their composition and morphology was influenced by the parameters of the synthetic reactions used in their preparation. The prepared nanoparticles were also subjected to heat and acid treatments, intended to optimise their surfaces for enhanced catalysis, and the methods used for these treatments are described, alongside further characterisation work aimed at understanding the utility and impact of those treatments.

Finally, the culmination of this work is in the electrocatalytic testing of those catalyst nanoparticles. These experiments were developed to ascertain the degree to which the prepared materials showed promise as possible alternative catalysts.

“Je crois que l’eau sera un jour employée comme combustible, que l’hydrogène et l’oxygène, qui la constituent, utilisés isolément ou simultanément, fourniront une source de chaleur et de lumière inépuisables et d’une intensité que la houille ne saurait avoir.”

Jules Verne, ‘L’Île Mystérieuse,’ 1874.

…..

“I believe that water will one day be employed as fuel, that hydrogen and oxygen which constitute it, used singly or together, will furnish an inexhaustible source of heat and light, of an intensity of which coal is not capable.”

Jules Verne, ‘The Mysterious Island,’ 1874.

For Richard, the 21st century Jules Verne.

Acknowledgements

Thanks are due to a great many individuals who supported this work. Firstly, I am immensely grateful for the continual support and guidance of my supervisors Professor Paula Mendes and Dr Neil Rees. The studies described herein were enriched thoroughly by contributions from a number of collaborators, particularly Drs Michael Fay and Emily Smith at the University of Nottingham, Dr Eric Prestat at SuperSTEM, and Douglas Carswell at the University of Durham. A huge thank you also goes to John Hooper for his consistently wizard-like problem solving capabilities.

Outwith the laboratory, my time at the University of Birmingham was made immeasurably more rewarding by my participation in public engagement with research activities. For that, I will forever be grateful to Jon Wood and Dr Caroline Gillett, who encouraged me, and Aimee and Coralie, who were the ideal collaborators.

Finally, to those who listened to my tantrums when gloveboxes exploded, heating mantles melted, and errant nanoparticles turned eagerly anticipated microscopy sessions into abject nightmares, thank you. To Aimee, Rhi, Pete, Bea, my Mum and brother (despite his jokes about me needing to get a “real job”), my dear friend and cheerleader Victoria, and my now husband, Richard, my greatest advocate and compass, thank you all for your unwavering support, your sympathetic ears, your pep talks, and your eventually effective thesis related nagging.

Publications Arising from this Work

1. Walker, James S. ‘Why isn’t heat the ‘hot topic’ in energy system decarbonization?’ Journal of Science Policy and Governance, **2017**, 11 (1).
2. Walker, James S.; Rees, Neil V.; Mendes, Paula M. ‘Progress towards the ideal core@shell nanoparticle for fuel cell electrocatalysis,’ Journal of Experimental Nanoscience, **2018**, 13 (1), 258-271.

Table of Contents

List of Figures

List of Tables

List of Equations

1 Introduction

1.1 Background and Context

Globally, demand for energy is growing year on year. This trend is predominantly driven by continued economic growth in the global south, including in highly populous nations such as China and India. Energy use in these countries is increasing to meet growth in demand for goods, services, mobility and comfort from emerging consumer classes. Forecasts, Figure 1, show that this upward trend in energy demand is likely to continue well into this century [1].

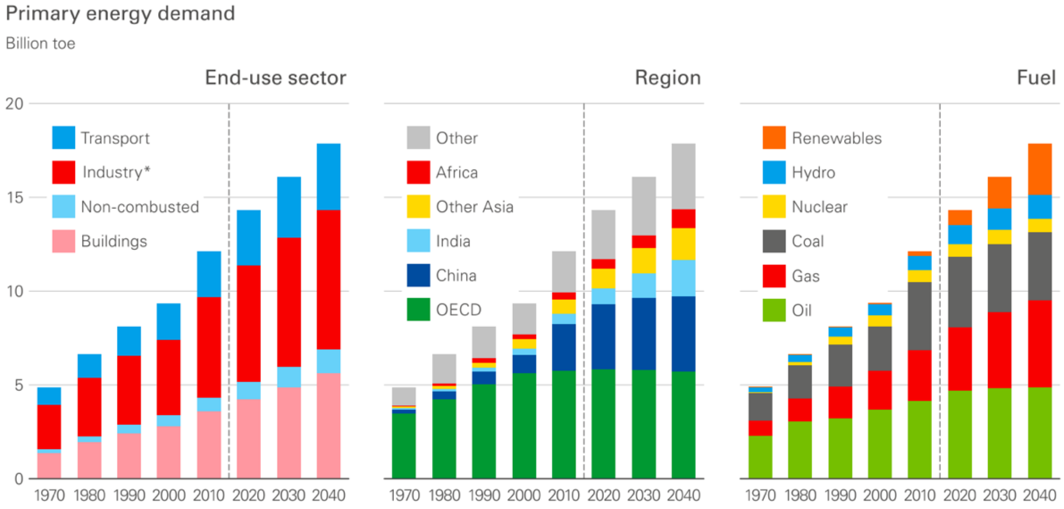

Figure 1. Forecasts for energy demand towards 2040 in terms of sectors, left, regions, middle, and fuels used, right. Where 'toe' refers to tonnes of oil equivalent. Reproduced from BP Energy Outlook 2019, [1].

The forecasts shown in Figure 1 also suggest that towards 2040 an increasing proportion of energy demand will be met by renewable energies. However, fossil fuels including coal, gas and oil will still be used to produce the majority of global energy, as they are today [1]. Combusting fossil fuels to produce energy causes the release of carbon dioxide (CO_2), which is typically emitted into the air. CO_2 is a “greenhouse gas,” which refers to its role in the chemistry of the earth’s atmosphere, where accumulated gases reflect radiated heat back at the earth, giving rise to global warming phenomena. Atmospheric CO_2 concentration is increasing as a result of continued emissions arising due to human activity, including fossil fuel combustion, and so global warming is exacerbating. Global temperature increases are expected to alter climates and weather patterns throughout the world, with potentially significant consequences for natural ecosystems and human populations. As a result, growing political and social movements have been advocating for action to reduce global CO_2 emissions through, for example, reducing rates of fossil fuel combustion [2].

2015 saw the signing of an historic United Nations Framework Convention on Climate Change (UNFCCC) agreement following negotiations between representatives from 195 countries. The so called ‘Paris Agreement’ has ushered in an era of unprecedented consensus on the need for action to reduce global emissions of CO_2 and other greenhouse gases. Under the agreement, signatory governments agreed to set ‘locally determined contribution’ targets for nationally appropriate decarbonisation actions. The parties to the agreement also collectively agreed to work to ensure that global warming is restricted to “well below” two ° C of average temperature rise [3].

In most cases, these targets commit those signatory governments to increasing the share of energy generated from renewable sources in their respective countries. The International Renewable Energy Agency (IRENA) recently published a roadmap for renewable energy deployment towards 2050, in which they forecast currently expected renewable generation deployments, and compared these against estimates for required capacity to meet Paris Agreement decarbonisation goals, Figure 2. The proportion of total primary energy supply generated from renewable sources is forecast to increase significantly in both cases. However, the figure clearly shows the gap between currently planned developments, the 'Reference Case,' and the actions required for compliance with currently stated commitments, as per the 'REmap Case,' [4].

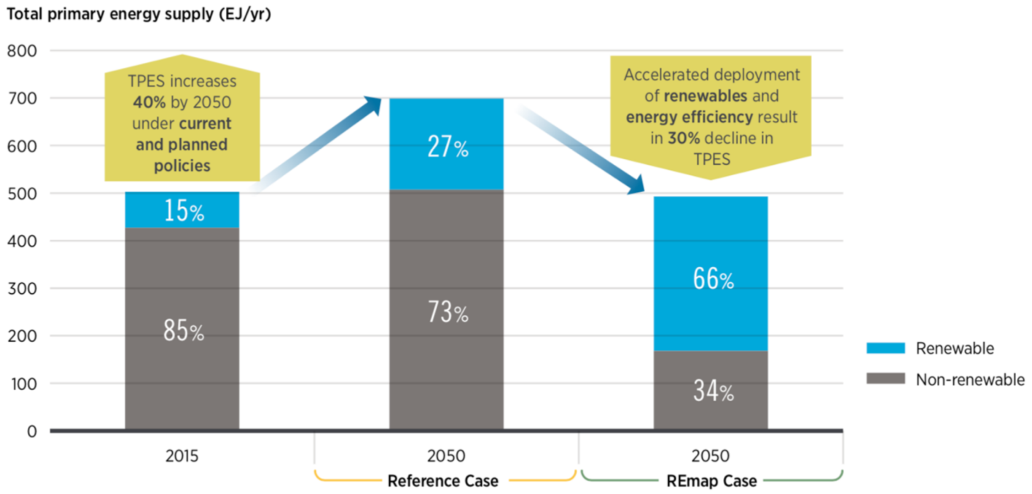

Figure 2. Forecasts for the proportion that renewable energy will make up of global energy supply by 2050. TPES refers to total primary energy supply. The reference case forecasts forward currently planned renewable energy developments. The 'REmap case' refers to the renewable energy deployments required to achieve targeted decarbonisation. Reproduced from IRENA Global Energy Transformation REmap, [4].

These figures relate to total energy supply across all energy vectors, including heat, and cover all end use sectors such as transport and industry. Meanwhile, renewable generation already meets a larger proportion of electricity demand in a number of developed countries, particularly in the European Union (EU). Data from the EU's statistics service, Eurostat, shows that 30.7% of electricity consumed within the bloc came from renewable sources in 2017.

Furthermore, some individual member states have made more progress than this, with renewable generation accounting for 72.2% of electricity consumed in Austria in the same period, relative to 65.9% and 60.4% in Sweden and Denmark, respectively. In the United Kingdom (UK), the figure is 28.1% [5] (though in Scotland, for example, the figure is far higher, with 74.6% of 2018 electricity consumption met by renewable generation [6]). 2018 data for the UK as a whole, prepared by the Department for Business, Energy and Industrial Strategy, show that 11% of the country's total energy consumption was met by renewable sources of energy. Of this total, 31% of electricity, 7.3% of heat and 6.2% of transport energy consumption could be considered renewable [7]. In the meantime, the UK's Committee on Climate Change (CCC), which provides expert advice to the UK and devolved governments on decarbonisation, published a 2019 progress audit for the country. This audit recommended for the UK governments to adopt more stringent targets aimed at delivering "net-zero" greenhouse gas emissions balances by 2050 (and by 2045 in Scotland). The CCC's net-zero recommendation was accompanied by substantial analysis on potential roadmaps and scenarios for how these systems could be delivered, including through enhanced rates of renewable generation deployments in the energy system, and in particular in the heating and transport sectors [8]. The CCC's recommendations were accepted by the relevant governments and have already been adopted in law at UK [9] and Scottish Government [10] levels, mandating that sufficient action be taken to deliver net-zero status by 2050 and 2045 in the relevant territories, respectively. The UK is not alone in forging this path, however, and at a recent UNFCCC conference it was announced that 73 nations already party to the Paris Agreement have further committed to achieving net-zero emissions by 2050 [11].

Delivering net-zero-emission societies will require radically different approaches to the way energy is produced, transported, stored and used, across all sectors of human activity. As noted, progress in deploying renewable technologies in heating and transport has been slower than in electricity, and as such the actions required to decarbonise these sectors has attracted significant interest recently. While electricity generated from renewable sources can be transported and used in exactly the same way as electricity generated from fossil sources, the same cannot be said for renewable forms of energy in the other sectors. Heating and transport are inherently more challenging to decarbonise in part due to the dominance and incumbency in these sectors of fossil fuel-fed technologies, and their supporting infrastructure. For example, a full 80% of UK homes are connected to the gas grid [12], and use gas powered appliances for space and water heating. Similarly, in transport, IRENA's analysis showed that in 2015 96% of global energy use in transport came from fossil fuel sources [4], with expansive petrol and gasoline refuelling infrastructure networks a common feature of modern road systems and urban environments. Fossil fuels are cheap commodities which for now at least are readily available [2], and displacing them in heating and transport will be challenging for policy makers. That said, battery electric vehicles (BEVs) are emerging at pace, with some 2 million sales in 2018 and an anticipated global market share of 30% in the passenger vehicle segment by 2040 [13]. There are technical difficulties associated with BEV range, which scales with battery size, and these limit scope for applications in haulage and other professional driving and transportation contexts.

Given these challenges, hydrogen has garnered significant attention as a potential energy supply vector. Proponents of hydrogen as a fuel point to its abundance and high energy density. Some suggest that hydrogen is an ideal replacement for natural gas, given that the only emission arising from its combustion or use in fuel cells is water. The CCC published a detailed review of emerging potential roles for hydrogen in the future UK energy system in 2018. In that report, the CCC pointed to a ‘hybridised’ future where hydrogen complements electrification in sectors such including heating and transport. Furthermore, the CCC highlighted a significant potential role for hydrogen to be used in sectors and applications which are especially difficult to decarbonise, including industrial heat production and heavy duty transportation, as well as in longer distance public transport provision [14]. These pathways depend on widespread deployment of low carbon hydrogen production capacities, either involving significant retrofit of existing steam methane reformation plants with carbon capture and storage equipment, or in development of electrolysis at scale. The electrolysis pathway also depends on sufficient supply of decarbonised electricity, such as to ensure that the hydrogen produced would itself be ‘low emission,’ [14]. Electrolysis itself is the focus of interest within the energy industry given the potential for so called ‘Power-to-Gas’ solutions to contribute to addressing integration challenges associated with increasing shares of renewable generation, which is inherently intermittent given changes in weather patterns. Power-to-Gas refers to the production of hydrogen, using electrolysers supplied by (likely renewable) electricity, in order to essentially store that electricity for use at a later date or in another context. Power-to-Gas installations are in development which will for example use tidal- or offshore wind-generated electricity to produce hydrogen in remote locations, which will then be shipped to centres of demand or even exported for use in providing energy in the power, heat or transport sectors [15].

A number of initiatives are underway in the UK and elsewhere to study and demonstrate the potential future hydrogen-based energy system solutions thus far described. A government funded programme in the UK have been reviewing the critical dependencies of hydrogen-based heating [16], and this is being tested on the ground in the industrial use case in the HyNet programme in the north west of England [17] and in a gas network blending programme at Keele University [18]. In the latter case, university buildings, including halls of residence, are being supplied with a mixed blend of 20% hydrogen within 80% natural gas. The developers aim to demonstrate that this gas blend is safe to use in existing gas appliances. In transport, hydrogen-powered fuel cell vehicles have been introduced in public and private passenger transport contexts in a number of locations. Fuel cell buses have successfully been incorporated into fleets operating in London, Aberdeen and other cities around the world [19]. Toyota launched the first major mass market fuel cell passenger vehicle, the Mirai, in 2014 [20]. Though these vehicles are currently niche inclusions in the relevant contexts, deployment figures continue to grow as a result of sustained investment, particularly in the wider EU under the Hydrogen Mobility Europe programme. This programme has dramatically increased the availability of hydrogen refuelling infrastructure throughout Europe, for example. By the end of the programme’s second phase in 2022, 49 public hydrogen refuelling stations will have been introduced on roads in Western Europe, including 6 in the UK [21]. Fuel cells can be used to efficiently generate electricity from hydrogen, among other possible fuels. Generically, fuel cells are defined as machines that convert the chemical energy stored in fuels to electrical energy through electrochemical reactions. Fuel cells are regarded as efficient electricity generation devices because their operation is not limited by the Carnot efficiency; that is to say that because the underpinning reactions and intermediate steps associated with their use do not involve the concomitant production of heat or mechanical work, they can achieve higher round trip efficiencies than conventional, combustion-based energy generation approaches. As electrochemical devices, fuel cells are often compared to batteries. The biggest differentiating factor between these devices is that with fuel cells, fuel must be supplied on an ongoing basis in order to facilitate continuous use [22]. In general terms fuel cell unit cells consist of two electrodes, separated by an electrolyte or membrane, with opposite redox electrochemical reactions occurring at each electrode. These unit cells can be arranged in parallel in stacks, encased by gas flow and current collection components in real world devices. A number of fuel cell types have been developed, with differing intended fuels and applications [22]. They are typically named and described by the type of electrolyte used within the unit cells, and can be categorised as laid out in Table 1.

Table 1. Comparison of differing types of fuel cell which have been developed, characterised by material and operational parameters and characteristics. Prepared using data from [22] *and* [23].

	Typical Materials						
Name	**Electrolyte**	**Electrodes**	**Catalyst**	**Charge Carrying Species**	**Operating Temperature Range (° C)**	**Typical System Efficiencies (%)**	**Intended Applications**
Polymer Electrolyte (PEFC)	Hydrated polymeric membrane, e.g perfluorosulphonic acid	Carbon	Platinum group metals, alloys	H^+	< 120	~60	Portable power and transportation (especially heavy duty vehicles)
Alkaline (AFC)	Potassium hydroxide solution in a porous matrix	Transition metals	Platinum group metals, alloys	OH^-	< 100	~60	Military and space, as well as backup power
Phosphoric Acid (PAFC)	Immobilised phosphoric acid in a silicon matrix	Carbon	Platinum group metals, alloys	H^+	150 - 200	~40	Distributed electricity generation
Molten Carbonate (MCFC)	Immobilised liquid molten carbonate in lithium matrix	Nickel and nickel oxide	Electrode material	CO_3^{2-}	600 - 700	~50	Electricity utility and distributed generation, as well as combined heat and power
Solid Oxide (SOFC)	Ceramic perovskites	Perovskite and perovskite/metal composites	Electrode material	O^{2-}	500 - 1000	~60	Electricity utility and distributed generation, as well as combined heat and power

Despite the advantages thus far described for fuel cells, their commercialisation as energy generation technologies has been relatively slow. The appeal of the range of fuel cell types summarised in Table 1 has been impeded by a number of challenges which have been the focus of significant research and development efforts in academic and industrial laboratories alike. Material challenges including catalyst poisoning and coking have impeded the PEFC and MCFC/SOFC fuel cell types, respectively, as a result of the fuels used. Further, developers of these devices have struggled to compete on cost with incumbent generation technologies due to the expensive components used in each case [22]. In particular, a myriad of potential candidate catalysts have been developed for use in PEFCs, AFCs and PAFCs, given the significant cost of the platinum group metal catalysts currently used in commercial models of these fuel cells. Efforts towards developing novel candidate catalyst materials are surveyed in the literature review which follows.

1.2 Literature Review

1.2.1 Introduction

Nanoparticles are defined by the International Organization for Standardization (ISO) technical standard 80004-2 [24] as materials for which all three of their external dimensions are in the nanoscale (1-100 nm). The ISO standard goes on to elaborate that materials in the nanoscale "often have properties that are not simple extrapolations of the properties of their larger form." That is to say, such nanomaterials exhibit physical and chemical properties not otherwise observed for macroscale objects of the same material. These unique properties have inspired significant scientific interest and research effort in a range of fields of human endeavour. Indeed, nanoparticles now find applications as diverse as in drug delivery [25], chemical sensing [26], and in protective "self-cleaning" coatings [27]. Another key application for nanoparticles is in catalysis, and particularly in electrocatalysis. In a recent review, Seh *et al* highlighted the crucial role for electrocatalysis in securing a "clean energy" future [28]. In their work, the authors refer to one of the key lines of development in electrocatalysis being work to increase the number of (catalytically) active sites on a given electrode. One strategy towards doing so is the use of nanoparticulate catalysts, which by definition will have a greater number of active sites gram for gram compared to a bulk material, due to their high surface area to mass ratio. This is an intrinsic property of nanoparticles; due to their nanoscale dimensions, a greater proportion of their mass is exposed to the surface than an equivalent macroscale bulk material. With this in mind, nanoparticle (electro)catalysts have been the subject of significant research endeavour in recent years.

One particular application of nanoparticulate electrocatalysts is in catalysing the reactions required for the operation of low temperature fuel cells, such as the polymer electrolyte fuel cell (PEFC). A PEFC consists of an anode and cathode separated by a polymer membrane, typically composed of a fluorinated polymer such as Nafion. At the anode, hydrogen fuel is dissociated in contact with the catalyst layer to produce two hydrogen (H^+) ions, and two electrons (e^-) in the hydrogen evolution reaction (HER), Figure 3. It is generally accepted that the reaction proceeds along a three step pathway, firstly involving adsorption of molecular hydrogen onto the catalyst surface. Once adsorbed, the molecule dissociates to liberate an ion and electron, alongside an adsorbed atom, which is further dissociated in a fast charge-transfer process [29]. The liberated ions diffuse through the proton-conducting polymer membrane while the electrons are forced through an external circuit to generate electricity. At the cathode side of the PEFC, the electrons and protons recombine with oxygen ions (O^{2-}), generated by the catalytic reduction of molecular oxygen (O_2) at the cathode catalyst, to produce water (H_2O), Figure 3. The oxygen reduction reaction (ORR) proceeds via two potential pathways, which are often referred to as 'direct' and 'indirect'. Direct oxygen reduction occurs in a four electron pathway in which oxygen molecules adsorbed onto the catalyst surface are reduced directly to form water, without the formation of hydrogen peroxide (H_2O_2). The indirect pathway involves first the formation of adsorbed hydrogen peroxide, which either decomposes to re-form adsorbed oxygen, desorbs into the solution, or is further reduced to eventually form water [29, 30]. In another fuel cell type, the direct methanol fuel cell (DMFC), the anode HER reaction is replaced with the methanol oxidation reaction (MOR), in which methanol is oxidised to liberate protons [31].

$$\text{a)} \quad \text{Anode: } H_2 \rightarrow 2H^+ + 2e^-$$

$$\text{b)} \quad \text{Cathode: } O_2 + 4H^+ + 4e^- \rightarrow 2H_2O$$

Figure 3. a) The hydrogen evolution reaction (HER), which occurs at the PEFC anode, and b) the oxygen reduction reaction (ORR), which occurs at the PEFC cathode.

Vignarooban and co-workers reflected on the “critical role” that electrocatalysts play in determining the utility, durability and cost of PEFCs [32]. The catalysts are typically composed of platinum (Pt) or other noble metals either dispersed directly on a carbon support or alloyed with other metals. As shown in Figure 4, Pt, like other platinum group metals, is an expensive resource [33]. Demand for Pt outstrips supply and the cost of the catalyst continues to limit the potential for fuel cells to become competitive with incumbent technologies. Physical approaches such as electrospraying [34] and sputtering [35] have been used to attempt to reduce platinum utilisation in PEFC electrodes with some success. However, the most significant research effort has been dedicated to developing novel nanoparticle electrocatalysts with reduced platinum loading, particularly through alloying.

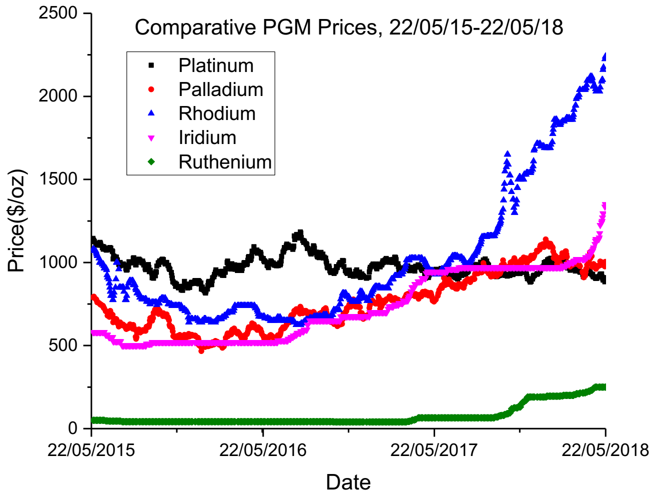

Figure 4. Daily price per ounce for five platinum group metals graphed using data recorded between May 2015 and May 2018 by Johnson Matthey Precious Metals Management [33]. Average per ounce prices in this period were: platinum $976.19, palladium $762.34, rhodium $1028.32, iridium $733.60 and ruthenium $76.40.

Alloying can increase the intrinsic activity of catalyst nanoparticles [28], as well as influencing their durability. One category of alloy nanoparticles, specifically core@shell systems, has garnered significant attention from researchers. In these nanoparticles, a thin layer of one material is deposited on top of a core composed of another material. This category of nanoparticles is of particular interest in catalysis, as a layer of an expensive, catalytically active metal such as Pt can be layered on top of a core composed of a cheaper metal. The most obvious benefit of doing so is economic; a high surface area of active metal can be realised with lower mass of that metal. As is highlighted in a number of other reviews, however, there are catalyst issues other than cost impeding fuel cell commercialisation, including catalyst durability and activity [30, 36–38]. The ideal core@shell catalyst system would confer economical savings while also realising enhanced durability and activity, however, and progress towards achieving these concurrent aims is the focus of this review.

1.2.2 Core@Shell Nanoparticle Configuration

1.2.2.1 Element Selection: d-Block Deliberations

Junliang Zhang and co-workers were among the first to report the use of core@shell nanoparticles to reduce platinum loading in fuel cell electrocatalysis. Using a metal deposition technique previously developed within the same group [39], they used galvanic displacement to replace a copper adlayer with a monolayer of platinum on palladium (Pd) [40], on alloy noble and non-noble metal cores [41], and on a range of crystalline transition metal cores [42]. They reported high activity relative to commercially available carbon-supported platinum (Pt/C) catalysts for their core@shell nanoparticles in ex-situ electrochemical testing, with reduced platinum loading.

In the intervening years, elements from all four corners of the transition metal block have been investigated as potential core materials. While Malacrida *et al* [43] prepared Pt-lanthanide alloys with Pt shells, and reported enhanced catalytic activity, most of the research effort has been focussed on the elements in the top corners of the d-block. Although describing alloys rather than core@shell particles, an oft-cited report which established the now ubiquitous ‘Volcano Plot’ (Figure 5) highlighted the high potential activity of Pt_3Y [44]. The volcano arranges Pt-based transition metal alloys according to literature-derived values for their kinetic current density, plotted against their computationally predicted oxygen adsorption energy. Knowledge of the oxygen adsorption energy of these nanoelectrocatalysts is crucial when attempting to predict their catalytic activity. The ideal oxygen reduction reaction (ORR) (Figure 5) catalyst will bind sufficiently strongly to oxygen to catalyse the reduction, but sufficiently weakly such as to encourage a high catalytic turnover.

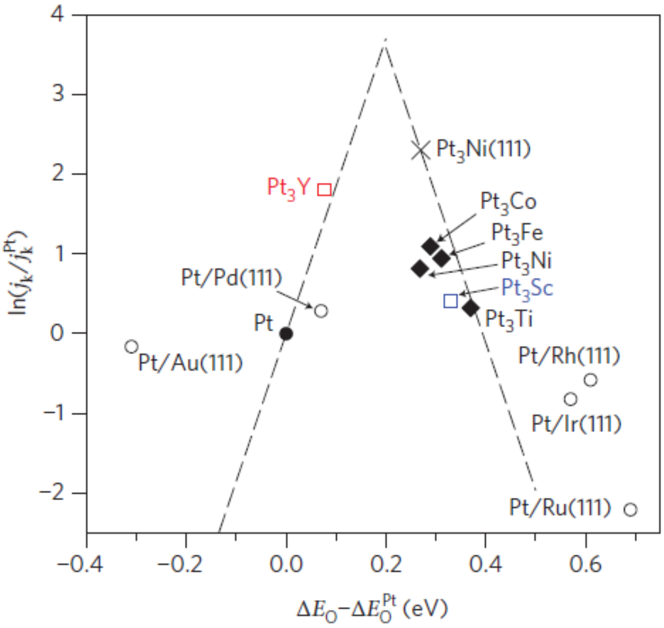

Figure 5. Kinetic current densities (ln(j_k/j_k^{Pt}) vs. oxygen adsorption energies ΔE_O - ΔE_O^{Pt} (eV) for a range of bimetallic transition metal-platinum alloys. Reproduced from [44] with permission from Springer Nature.

In this study, it was observed that, as predicted, Pt_3Y and Pt_3Sc alloys kinetically outperformed Pt/C in electrochemical testing. Accordingly, the early transition metals (Sc, Y, Ti) garnered significant attention from researchers looking to prepare highly active electrocatalysts – including those focussing on core@shell morphologies.

In no small part due to its low cost relative to Pt, Ti in particular has proven to be a popular candidate core/alloy material. In 2011, Jennings *et al* [45] highlighted the gulf between costs for the two elements – with approximate costs of £9.28 kg^{-1} for Ti and £35000.00 kg^{-1} for Pt in July 2011 – and examined Ti@Pt cluster ORR kinetics using Density Functional Theory (DFT) calculations. Pure

Pt and Ti clusters were studied, as were $Pt_{32}Ti_6$ and Pt_6Ti_{32} configurations. The kinetic current densities and oxygen adsorption energies calculated for Pt_3Ti, as shown on the volcano plot, Figure 5, do not predict it to be the ideal catalyst [44]. However, the authors of this study [45] noted the variance in electronic properties expected of nanoparticle catalysts, relative to metallic bulk compositions of the same alloys. Indeed, the Pt-Ti clusters studied "exhibited favourable properties" when compared to the pure Pt clusters. Namely, the $Pt_{32}Ti_6$ clusters bound hydroxyl groups less strongly than pure Pt clusters in simulation and this feature would be expected to confer enhanced ORR kinetics. Comprising 85% Pt and 15% Ti, though, it was conceeded that these clusters would be unlikely to offer significant economic advantages over the commercially available Pt/C catalysts [45].

The authors additionally drew attention to propensity of Ti to form strong bonds with oxygen. Accordingly, Ti@Pt clusters have been experimentally elusive. Instead, Pt@TiO_2 clusters have been prepared solvothermally [46] and generated using a magnetron sputtering gas condensation cluster source [47]. It appears that the TiO_2 shell forms preferentially vis-à-vis the alternative Ti@Pt configuration, likely due to the affinity of Ti for oxygen. While TiO_2 has been employed in photocatalysis, the search for the ideal core composition for ORR electrocatalysis must continue elsewhere.

Similar issues befell attempts to employ another cheap metal, chromium, as a core material in catalyst particles. Cr@Pt proved to be unattainable due to the formation of Cr oxides alongside pure Pt nanoparticles [48]. Instead, the same group prepared non-segregated Pt-Cr alloys, which showed enhanced durability relative to Pt/C in electrochemical testing [49].

Shifting focus towards the other end of the d-block, two interesting observations were made following studies of prepared Cu@Pt particles. Firstly, Cu@Pt nanoparticles with varying Pt shell thickness were prepared using ethylene glycol both as solvent and reducing agent [50]. Although none of the particles demonstrated catalytic activity superior to that of commercial Pt/C catalysts, the authors noted a relationship between catalytic activity and shell thickness; the Cu@Pt particles with the thinnest Pt shells were the most catalytically active. In another work, Cu@Pt particles were prepared via sequential reduction of Cu and then Pt precursors on carbon. In initial electrochemical testing, the catalytic performance of the particles was similarly inferior to that of Pt/C, however the particles showed enhanced sustained activity over 1000 cycles [51]. This durability enhancement requires further study.

In terms of achieving catalytic activity enhancements, a recent review of iron-containing Pt-based catalysts for fuel cell applications highlighted favourable weakening of Pt-O bonds, attributed to metal lattice shrinkage in Pt-Fe alloys [52]. This effect was demonstrated experimentally in 2013 when Jang *et al* [53] prepared Fe@Pt nanoparticles with varying elemental composition via ultra-sound assisted polyol synthesis. In this study, $Fe(acac)_3$ and $Pt(acac)_2$ were mixed in a range of molarity ratios in ethylene glycol and sonicated. The particles formed were characterised using a range of microscopy and spectroscopy techniques, including X-ray diffraction (XRD). XRD was used to confirm the formation of a Pt shell on an Fe core due to the absence of characteristic iron or iron oxide peaks (Figure 6). The researchers additionally performed a DFT analysis of oxygen binding with results suggesting weakened Pt-O bond formation for the formed particles. This expectation was confirmed by electrochemical measurements which showed that clusters with compositions $Fe_{1.2}$@Pt (i.e 55% Fe), with Pt monolayers were up to 6.5 times more active for the ORR than commercial Pt/C.

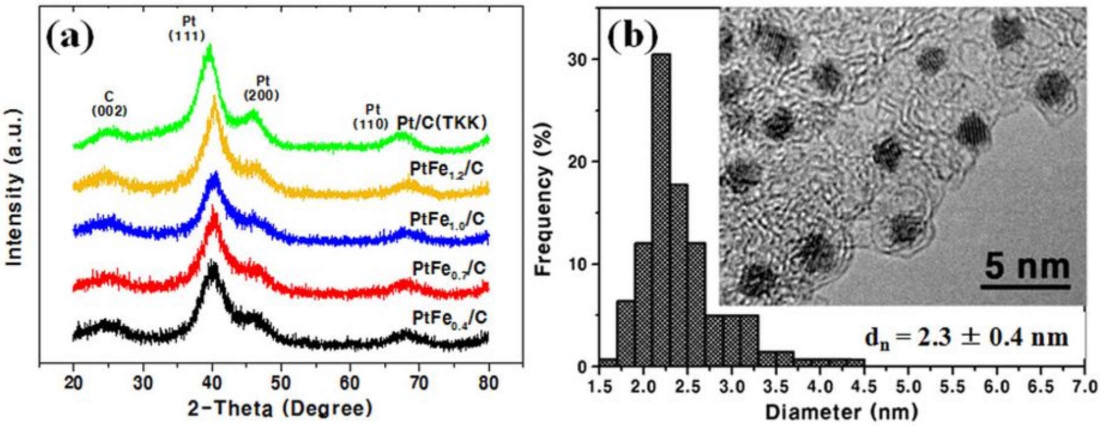

Figure 6. a) X-ray diffraction patterns for a range of Fe@Pt samples showing clear shifted Pt peaks in the alloyed samples but no iron or iron oxide peaks, and b) a TEM image with sizing measurements on Fe@Pt nanoparticles. Reproduced from [53] *under Creative Commons license (CC BY-NC 3.0).*

Other work has focussed on incorporating nickel and cobalt into Ni@Pt, Co@Pt and indeed Ni-Co@Pt particles. Marking a step-change in approach, the synthesis of ordered core-shell nanoparticles with Pt_3Co bimetallic cores coated by a 2-3 atom thick layer of Pt was reported in early 2013 [54]. In this study, the researchers heat-treated a batch of their Pt_3Co@Pt nanoparticles at 700 °C under a flow of H_2 gas to engender ordering in the lattice structure of the Pt_3Co

core alloy. Physical and electrochemical characterisation results for an annealed sample, denoted Pt_3Co/C-700 and an un-treated sample, Pt_3Co/C-400 were compared. Annular dark field scanning transmission electron microscopy (ADF-STEM) and electron energy loss spectroscopy (EELS) were used to map the elemental composition of the clusters and to confirm the formation of a Pt shell in each case. XRD measurements of the annealed samples highlighted increased lattice contraction and the pronouncement of (100) and (110) crystal phases, confirming the increased ordered crystallinity associated with this treatment. In initial electrochemical testing, both samples outperformed conventional Pt/C catalysts but of most interest is the trend identified after significant electrochemical cycling. After 5000 cycles, the electrochemically active surface area (ECSA) was measured for both samples, alongside further ‘post-mortem’ physical characterisation. The authors noted that the electrochemical activity measured for Pt_3Co/C-700 remained constant after these cycles, and EELS measurements and images confirmed that the nanoparticles remained well dispersed on the carbon supports. A 30% reduction in ECSA was observed for the Pt_3Co/C-400 samples in the same timeframe. These results highlight the potential for improving catalyst durability through inducing molecular/crystalline ordering.

Ni@Pt particles have proven to be particularly popular catalyst candidates. Early work focused on the preparation of Ni@Pt particles with varying surface coverages of Pt through a modified polyol process [55]. Catalysts with monolayer

Pt shells were found to be the most active, with the researchers showing that increased coverage of Pt did not confer enhanced activity or durability.

Other researchers have exploited the difference in nobility between Pt and Ni to prepare ‘de-alloyed’ catalysts. Corroding the catalysts either electrochemically, using potential cycling, or chemically, using acid, results in the selective removal of the less noble metal (in this case Ni) from the surface layers, producing particles with Pt-enriched surfaces. A recent review [56] discussed the balancing act in dealloying, in which catalyst activity gains can be associated with losses in durability. Corrosive dealloying encourages sub-surface reorganisation of Ni which can engender optimised strain upon the Pt shell, thus enhancing catalytic activity. However, corroded particles can also exhibit porosity on the nanoscale, which makes them vulnerable to additional degrees and mechanisms of degradation. Studies [57, 58] have shown that initial particle composition in terms of Pt:Ni ratio has a significant influence on eventual Pt shell thickness following dealloying. $PtNi_3$ particles have shown the most significant enhancements in catalyst activity when compared to commercial Pt/C, relative to PtNi and $PtNi_5$. This observation is made despite $PtNi_3$ particles having the thickest Pt shells. These findings led the authors to elaborate on prior conclusions that catalytic activity scaled simply with shell thickness. Through aberration-corrected STEM imaging and EELS measurements (Figure 7), the configuration of the particles was analysed. In particular, the researchers were interested in how platinum:nickel density varied across the profile of their particles and this is shown in the EELS line scans shown in panels b-d, f-h and j-l in Figure 7. In the

PtNi case (b-d) distinct core and shell components are observed with relatively smooth profiles. In the $PtNi_3$ and $PtNi_5$ particles (f-h and j-l, respectively), however, the line profiles show clear bumps, indicating areas of higher and lower concentration of Ni in the ‘core.’ The researchers thus describe the formation of Ni-enriched inner shells in their $PtNi_3$ and $PtNi_5$ particles. They surmise that enhanced strain is exerted upon the Pt outer shells by the inner Ni layers, enhancing catalytic activity, and that this effect is most significant in the $PtNi_3$ system.

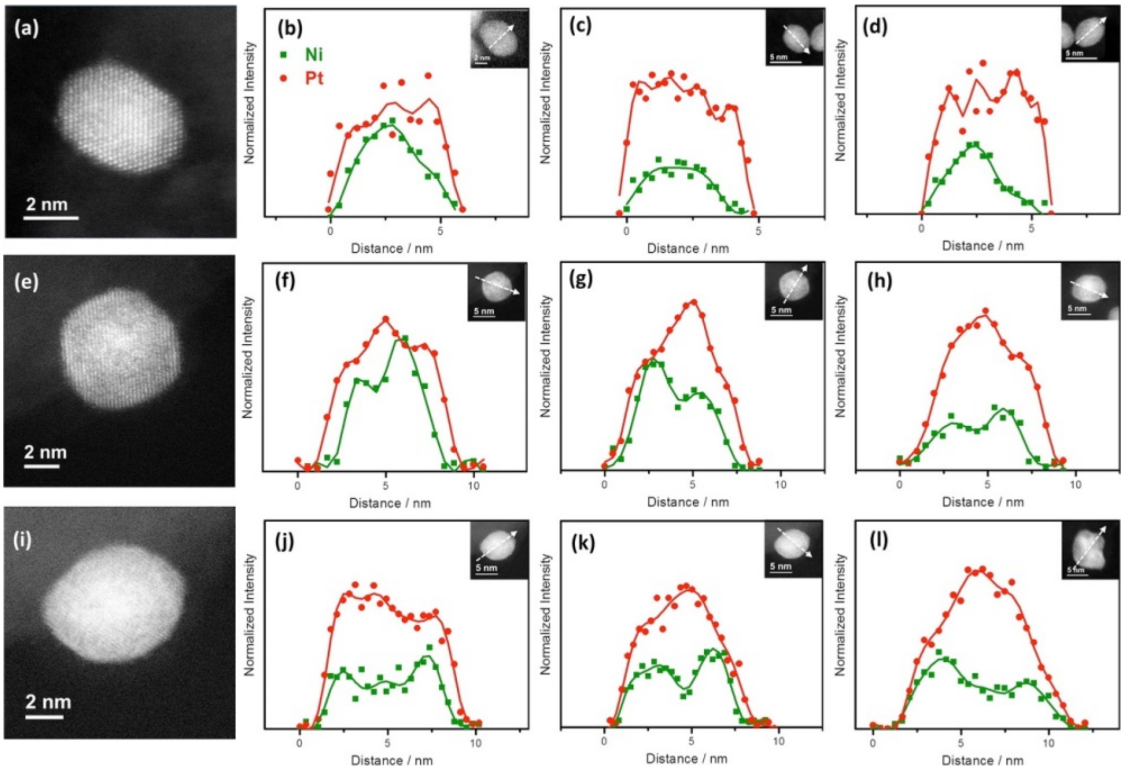

Figure 7. HAADF-STEM images and EELS line profiles of D-PtNi (a–d), D-$PtNi_3$ (e–h), and D-$PtNi_5$ (i–l) nanoparticles. Reprinted with permission from [57]. Copyright © 2012 American Chemical Society.

A number of studies focussing on the preparation and characterisation of PtNiCo alloys, and NiCo@Pt particles have followed. Ternary alloys, and bimetallic alloys coated with Pt, demonstrating high catalytic activity and durability have been widely reported but the mechanism for these improvements is ill understood. In one particular work, Pt-Ni, Pt-Co and Pt-Ni-Co alloys were prepared, with thin Pt ‘skin’ outer layers deposited electrochemically [59]. In their synthesis, the researchers first electro-deposited Ni or Co (or both Co and Ni in the Pt-Co-Ni case) onto a glassy carbon electrode surface. The coated electrodes were subsequently immersed in K_2PtCl_6 solution to permit replacement of Co and Ni with Pt, prior to a voltammetric dealloying step in which potential was applied across the −0.3−1.5 V range to form a stable Pt outer surface. “A few layers” of Pt, with thickness of “a few nanometres,” were deposited, so the authors suggest that total platinum loading was low in each case [59]. These layers were characterised physically and electrochemically, and activity enhancements over Pt/C were observed in the range Pt-Ni-Co > Pt-Co > Pt-Ni. The authors concede that further work will be required to understand the origin of the degree to which ORR activity is enhanced for their ternary alloy, but they surmise that interactions between Co and Ni contribute additionally to electronic d-band effects and lattice constant mismatch such as to further weaken Pt-O bond strengths at the surface of their electrode.

Lattice mismatch and the associated surface strain are oft-cited, frequently poorly explained phenomena which are crucial to the development of ideal core-shell electrocatalysts. In further computational studies, Jennings and colleagues sought to understand these effects and predict which metal-platinum (M@Pt) combination would realise the theoretical optimum structure. In his doctoral research [60], Jennings highlighted a triumvirate of properties which contribute to the stability of any intermetallic cluster structure – those being the surface area exposed, the surface energy of those external facets, and the internal strain associated with atomic rearrangements. These strain effects are particularly significant in clusters composed of metals of varying sizes and electronegativities. Larger atoms, and those which are more electronegative, are more inclined to adopt positions at the surface of a given cluster.

The size factor accounts for the mismatching of crystal lattices when shell layers of platinum form atop core surfaces with varying atomic radii. These strain contributors influence Pt-Pt bond length at the cluster surface, with knock-on impacts upon adsorbate binding energies in that shorter Pt-Pt bonding results in weaker Pt-O binding. These effects were examined and illustrated experimentally by Strasser and colleagues [61] when they studied the constructive effect of compressive strain in Cu@Pt electrocatalytic clusters. In low energy electron diffraction experiments, the researchers observed a broadening of the electronic d-band of their Cu@Pt clusters, and ascribed this to enhanced overlap between metal electronic clouds with decreasing atomic distances. The effect of this broadening contributes to enhance ORR kinetics at the surface of the particles prepared. To quantify the relationship between strain and catalytic activity, the researchers compared measured experimental values for their clusters to a theoretically derived volcano plot, shown in Figure 8. Computational work suggested that the ORR activity would peak at a certain critical strain value, after which point Pt-O binding would be too weak for the reaction to occur readily. The researchers did not observe this trend, however, and suggest that this may be due to differences in strain experienced by Pt atoms at different positions within the particles. They hypothesise that Pt atoms adjacent to the Cu core will relax under strain to adopt lattice parameters closer to that of the Cu atoms, while surface shell Pt atoms – those directly engaging in catalysis – will relax towards lattice constants more typical for bulk Pt. Such an effect was described previously for Pt films grown on Cu (111) surfaces [62]. These observations contributed significantly towards a more robust understanding of the theoretically predicted trends in core@shell catalyst activities, while also further demonstrating the complexity of these systems.

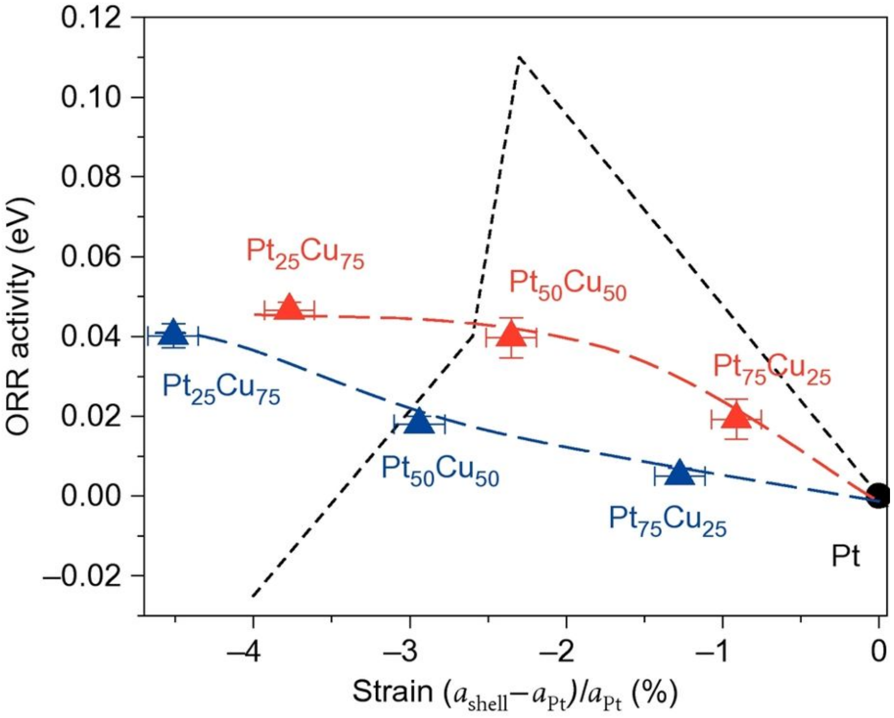

Figure 8. Experimentally verified ORR activities as a function of strain for Cu@Pt nanoparticles with red and blue triangles referring to particles annealed at 800 and 900 °C, respectively. The dashed line relates the theoretically predicted relationship. Reproduced from [61] *with permission from Springer Nature.*

In a further theoretical work, Jennings *et al* [63] computationally analysed rates of oxygen dissociation at M@Pt surfaces relative to shell flexibility. This flexibility, intrinsically linked to lattice mismatch and core-size, permits the distorting of the shell to facilitate fast oxygen dissociation. These flexibility studies recommended alloying with late transition metals (particularly Ni, Cu and Zn) as their interaction with platinum is sufficiently weak as to permit permutation of the outer shell layer. The authors conceded though that alloys and core@shell clusters composed of these elements were impeded by stability issues due to dealloying and dissolution. These findings all contribute to a growing understanding of the need to acknowledge and plan for factors additional to the d-electron band centre downshifting associated with core-metal electronegativity.

The structural and geometrical insights outlined thus far encourage conclusions which are at times rather contradictory. Rationally assessing all of the evidence available, it seems that M@Pt nanoparticles formed with either early or late transition metal cores have opposite advantages and disadvantages to recommend their use in ORR electrocatalysis. Where the early transition metals, particularly Y, Sc and Ti have been lauded for their capacity to weaken Pt-O binding energies through their strong interactions with the Pt shell, so too have late d-metals such as Ni and Cu been idealised for their capacity to weakly interact with a thus highly flexible and attractively dissociative outer shell. Perhaps then the formula for the ideal M@Pt cluster requires a ‘just right’ compromise between characteristics associated with these two diverging poles. Cognisant of this observation or otherwise, a number of researchers have focussed their efforts on elements which adopt central positions within the transition metal block. Elements drawn from the ‘platinum group metals’, Pd, Rh, Ir, Ru and Os have thus piqued the interest of researchers, and have been incorporated in core@shell cluster catalysts in a number of different conformations. Lu *et al* [64] prepared PtPd nanodendrites, while Pd@Pt nanocrystals were preferred by Qi and colleagues [65]. Both groups reported enhanced catalytic activity ascribed to the formation of thin catalytic layers and ordered core-shell alignment, respectively. Ordered trimetallic core@shell catalysts have also been prepared. IrRe@Pt particles demonstrated comparable activity to commercial Pt/C with high durability [66]. However, the major disadvantage associated with forming cores with the platinum group metals described is that they too are of limited abundance and useful in industrial processes. As a result, they are also expensive materials. A comparison of platinum group metal costs is shown in Figure 4.

As shown, ruthenium, with an average price of 76.40 \$/oz in 2015-2018, is an exception to the rule in that it comes in at least 12 times cheaper than platinum, which has averaged 976.19 \$/oz over the same period [33]. Accordingly, researchers have looked to ruthenium as a very eligible candidate for M@Pt studies. In 2013, ordered Ru@Pt nanoparticles were synthesised using a new method which reportedly minimised the formation of crystal lattice deformations. These nanoparticles were subsequently tested in a fuel cell stack to measure their capacity for catalysing the hydrogen evolution reaction (HER) at a PEFC anode. Significantly, the researchers tested their nanoparticles with a carbon monoxide-poisoned hydrogen stream and were able to demonstrate enhanced tolerance to poisoning when compared to commercial Pt/C. This effect was ascribed in part at least due to the chemical ordering engendered in the Ru-core following an annealing step at 450 °C [67]. This group once more highlighted the contribution that defined chemical ordering made to the activity and durability of their catalysts. This phenomenon has been further studied, with Cu@Pt-Ru nanoparticles tested as methanol and carbon monoxide oxidation catalysts in two successive works [68, 69]. The authors noted in both cases that their nanoparticles demonstrated enhanced tolerance to carbon monoxide poisoning. The enhanced durability of each of the catalysts described highlights a unique property of alloyed Pt/Ru surfaces.

A more recent work with Ru@Pt HER catalysts sought to further investigate strain effects, and their impact upon the catalytic activity of Pt shells [70]. To this end, the researchers prepared defined Ru@Pt particles alongside RuPt alloy catalysts. Higher hydrogen oxidation activities were reported for the Ru@Pt particles, with this attributed to weakened hydroxyl binding by the Pt shell as a result of high strain. The strain arises in the particles due to the mismatch between the platinum and ruthenium lattices.

Subsequent work with Ru@Pt clusters has focussed on oxygen reduction. One particular paper highlighted the potential to tune the ORR activity of the particles by varying the thickness of the Pt shell [71]. Using an underpotential deposition technique, platinum mono- bi- and tri-layers were deposited onto a pre-prepared ruthenium core. These structures were confirmed using HAADF-STEM imaging and EELS measurements. In electrochemical testing, highest catalytic activities were observed for the Ru@Pt clusters with Pt bi-layer shells.

The researchers sought to explain this finding using DFT calculations. These calculations show that for the catalysts studied (Ru@Pt$_{1ML}$, Ru@Pt$_{2ML}$, Ru@Pt$_{3ML}$ and Pt/C), Ru@Pt$_{2ML}$ struck the optimal balance in terms of fast O-O bond scission, but also in terms of facile hydrogenation in the removal of bound O.

A further paper described the preparation of core-shell like “Pt-surface-enriched” Pt-Ir and Pt-Ru nanoparticles [72]. In this work the researchers reported that their Pt-Ru nanoparticles achieved comparable catalytic activity to commercial Pt/C standards, but noted that these same nanoparticles performed very poorly in accelerated degradation testing, likely due to dissolution and dealloying.

Jackson and colleagues followed with recent work in which they prepared durable and active Ru@Pt catalysts using a wet chemical method [73]. In their study, the researchers sought to evaluate the impact of varying nanoparticle precursor ratios, finding that the most active catalyst was that prepared with an Ru@Pt ratio of 1:1. Significantly, these optimised particles retained 85% of their activity following accelerated degradative cycling. The researchers reported that the Pt shell protected the otherwise vulnerable Ru core from corrosive degradation.

1.2.2.2 Incorporating Non-Metals

In order to address issues of durability, an additional class of core@shell materials have been investigated. In these systems, non-metal elements are incorporated into the alloy materials. In so doing, researchers have reported a range of novel properties.

Ternary compounds with metal nitride alloy cores were prepared by Kuttiyiel and colleagues [74]. In this work, CoN@Pt, FeN@Pt and NiN@Pt nanoparticles were prepared and characterised electrochemically with respect to standard Pt/C. The increase in specific activity over Pt/C observed was ranked as follows: NiN@Pt > FeN@Pt > CoN@Pt. More significantly, in degradation testing all three catalysts were found to be more durable than Pt/C. Negative shifts in half-wave potential of 5 mV, 5 mV and 11 mV for NiN@Pt, CoN@Pt and FeN@Pt respectively, which was compared to 40 mV for Pt/C. Aside from referring to the formation of nitrogen bonds, the authors do not offer any theories as to why nitriding the core metals gives rise to this effect. It seems reasonable to suggest that the metal nitrides would be less vulnerable to degradative oxidation than their pure metal equivalents due to the formation of stable nitride species, with reduced unbonded valence electronic character.

In a similar vein, researchers focussing on electrocatalysis for the MOR in direct methanol fuel cells have observed that while Ru catalysts are more tolerant to methanol poisoning than Pt, they are vulnerable to oxidation. Several works have demonstrated the possibility to make these Ru catalysts more durable by forming alloys of ruthenium-selenide, RuSe [75],[76]. The mechanism for this improvement in durability has been ascribed to the formation of stable complexes between Ru and Se, which do not oxidise as readily as bare Ru metal.

1.2.3 Conclusions and outlook

Core@shell nanoparticles offer an attractive route towards decreasing platinum loading in electrocatalysts for fuel cells. As has been discussed, they also have the potential to realise enhanced catalytic activities and durabilities as compared to commercial Pt/C catalysts. This review has focussed on Pt-shell nanoparticles with a range of differing core materials, as this still reflects the approach taken by the majority of those publishing in this field. Indeed, as demonstrated, a wide array of candidate core materials have been studied by researchers, with virtually all of the transition metals having been incorporated into TM@Pt assemblies. The resultant literature is at times dizzying given the sheer volume of systems being explored, and reticence within the community to adopt standardised testing procedures can make meaningful, quantitative comparisons between published works difficult. Several trends emerge from the works surveyed here, however as summarised in Table 1. The first is the initial attractiveness of candidate core materials drawn from the upper corners of the d-block. Cores composed of early transition metals such as Sc, Ti and Cr were predicted to confer the most constructive electronic effects upon Pt shells, but these proved challenging to prepare given the electronegativities of the elements, and their propensities to readily oxidise and thus adopt shell positions [47, 48]. Looking to the other end of the d-block, however, researchers have reported impressive relative activity gains for Co@Pt, Ni@Pt, and Cu@Pt particles, but these systems have been plagued with issues of poor durability [77]. Despite their comparative expense, then, the platinum group metals have thus remained reliable candidates due to their nobilities. PGM@Pt particles are arguably more stable than the alternatives described but this stability arises in part due to a smaller electronic divergence from the bulk lattice constant or atomic radii of shell Pt atoms [60, 63] than other elements described, so it is unlikely that these particles will contribute to significant, record-breaking gains in catalytic activity. Given the challenges associated with each group of transition metals described, it is unlikely that ideal core@shell catalysts will be prepared simply by adopting the best possible candidate core material. Instead, it seems likely that researchers will seek to prepare optimised catalysts using a range of the materials described, focussing on addressing the issues highlighted with each candidate system through a range of other approaches. One standout observation from the works surveyed is the importance of – and challenges associated with - optimising shell thickness. While some researchers found that particles with thin (mostly monolayer) Pt shells were most active [50, 55], others observed higher activities for particles with slightly thicker shells [57, 58, 71]. Strasser *et al's* work with Cu@Pt highlighted the importance of balancing strain effects, which do not scale linearly with shell thickness, when designing catalysts [61]. Other key priorities may focus on enhancing surface area and active site availability of catalysts; with one growing area of interest being the preparation of novel and ever more complex nano-morphologies, including nanowires [78] and nanoframes [79]. Meanwhile, we are sure to see a growing emphasis on developing novel strategies to enhance durability of some of the catalyst systems most prone to degradation. Ever more complex alloys with designed-in protection are one potential route, with third and fourth components, including p-block elements as per the nitriding example mentioned above [74].

Clearly it is difficult to choose any one leading candidate in this class of materials, and it is likely to become even more difficult to do so as these systems become ever more complex. Hopefully, though, researchers keeping the end application – and considerations of scale-up and commercialisation – in mind will contribute to preparing better and better catalysts which can facilitate wider roll out of fuel cell technologies.

Table 2. Summarises key findings in terms of whether or not core@shell particles have been prepared for the given elements, and whether enhanced activities or durabilities have been reported for those particles. Notes: a. refers to reference [61]. *b. notes that enhanced durability is reported but that the tests described are less rigorous than typical. c. notes that reported enhanced durabilities vary with annealing temperature.*

Element	**Succesful M@Pt?**	**Activity**	**Durability**	**References**
Ti	×	-	-	[23],[24]
Cr	×	-	-	[25]
Cu	✓	↓/↑[a]	↑	[27], [28], [38]
Fe	✓	↑	↑[b]	[30]
Ni	✓	↑	↓	[31], [32], [33], [34], [35], [36]
Co	✓	↑	↓/↑[c]	[31], [36]
Pd	✓	↑	↑/↓	[41], [42]
Ru	✓	↑	↑/↓	[44], [45], [46], [47], [48], [49], [54]

1.3 *Aims and Objectives of this Work, and Structure of Thesis*

The focus of this thesis is on efforts to develop a novel ternary alloy catalyst nanoparticle, which would be more cost effective, catalytically active and durable than the platinum commercial standard currently used widely. The chapters which follow describe work carried out towards this aim, which has been guided by cognisance of the context as laid out first, and the prior endeavour described in the previous section. The candidate material chosen was core-shell RuSe@Pt. As described in detail in the preceding section, Ru@Pt materials have been reported with enhanced catalytic activities, attributed to the constructive influence of the Ru core on the Pt atoms in the shell [73, 80]. However, durability issues associated with all core@shell nanoparticles, due to dealloying and dissolution, as is also discussed in detail in the previous section, encouraged the design of a would-be core material with improved stability. Given prior research showing the durability of RuSe nanoparticles as catalysts in their own right [81–84], it was anticipated that an RuSe core material could prove to be the ideal surface upon which to layer an active Pt shell, to deliver durable catalysis.

With this in mind, the work which follows work concerned attempts to prepare and characterise RuSe@Pt nanoparticles, and to test their electrocatalytic potential in a benchmarking exercise in which they were compared to standard commercial catalysts. This work is described hereafter in three chapters;

Chapter 2) Preparation of RuSePt Nanoparticles, which concerns synthetic procedures carried out in attempts to reliably produce RuSe@Pt nanoparticle catalysts, and relates physical and chemical characterisation of the prepared particles. Efforts towards optimisation of the synthetic procedures developed are also described;

Chapter 3) Efforts Towards Controlling the Morphology and Surface Composition of RuSePt Nanoparticles, in which acid and heat treatment protocols used to influence the structure of the prepared nanoparticles are described. The success of those protocols is interrogated, and;

Chapter 4) Electrocatalytic Testing of RuSePt Nanoparticles, in which electrochemical testing and benchmarking of the optimised and treated nanoparticles is described, compared to results acquired for commercial standard catalysts.

2 Preparation of RuSePt Nanoparticles

2.1 Background and Context

A wide range of chemical and physical approaches have been developed for the synthesis of nanoparticles, including a number which have already been described in the preceding section. Identifying novel synthetic routes with ever greater degrees of kinetic and/or thermodynamic control over the composition and configuration of the product nanoparticles has been the focus of significant research effort over the last few decades. This work requires an understanding of, and reference to, the fundamental chemical and physical phenomena driving nanoparticle assembly, which are outlined briefly here. A number of promising approaches are also surveyed here, before focussing on the theoretical underpinning and stage of development of the solvothermal synthetic routes which become the focus of the chapter which follows. This section also includes an overview of the capping agents and surfactants available to researchers who wish to control the dynamics of the synthesis of their nanoparticles, as well as the characterisation techniques and equipment available to study the effects of those interventions.

Physical nanoparticle synthesis methods have been developed, including atomic layer deposition [85] and condensation in the gas phase using magnetron sputtering from a cluster beam source [47]. These methods afford significant control over the properties and parameters of the nanoparticles, though they require specialised equipment and expertise.

Colloidal routes dominate, however, due to the comparative ease of handling the product nanoparticles. A colloid consists of a suspension of one phase, likely a solid material, in another phase, typically a liquid medium [86]. Colloidal nanoparticle suspensions have been studied for many, many years. Indeed, famously, the first report of the preparation of a colloidal suspension was by Michael Faraday in 1857, in a lecture in which he described the curious interaction of light with a gold nanoparticle colloid [87]. In the intervening years, significant research effort has focussed on elaborating these methods to engender further control over the nanoparticles prepared.

Most metal nanoparticle colloid syntheses proceed via the initial reduction of metal complexes or salt precursors dissolved in solution, which supply a source of ions of the target metal. The reduction may take place through a chemical method involving a reducing agent [65, 88–90], or may be decompositional in nature; whereby the precursors are reduced, using a physical method such as ultrasonication [91], or more regularly, thermally. In solvothermal reactions, nanoparticle precursors dissolved in solvents are decomposed by heating them at high temperatures. Some researchers have pursued microwave-assisted solvothermal syntheses, whereby microwave appliances are used to rapidly provide the heat required for precursor decomposition [92, 93], however the majority of researchers employ more conventional lab based heating appliances such as hot plates and oil baths or heating mantles.

Irrespective of the approach taken, the purpose of the reduction step in nanoparticle synthesis is to elicit the formation of zero valent metal atoms, dispersed in the reaction media [86]. Thereafter, nanoparticles emerge over the course of a three step process [94]. The first step is nucleation of these metal atoms, and the formation of growing nuclei. Different nucleation mechanisms are anticipated depending on the method used to reduce the metal precursors. LaMer and colleagues studied the mechanisms associated with the emergence by nucleation of sulphur atoms in the preparation of colloidal hydrosols in the 1950s [95]. Their work has had significant influence over modern understanding of the mechanisms underpinning decompositional nucleation in nanoparticle synthesis, as described in the detailed overview provided in a 2009 review drawn upon here [94]. Those latter authors graphically depicted the stages involved in nucleation, as reproduced in Figure 9 [94]. In such a decompositional process, the concentration of metal atoms in solution steadily grows as the decomposition proceeds. Once the metal atom concentration reaches a minimum threshold, as depicted by C^{nu} min., homogeneous nucleation occurs, in which nuclei emerge as the atoms begin to react together to form small clusters. A growth phase follows as homogeneous reactions continue, growing the nuclei, causing a concomitant reduction in metal atom concentration [94].

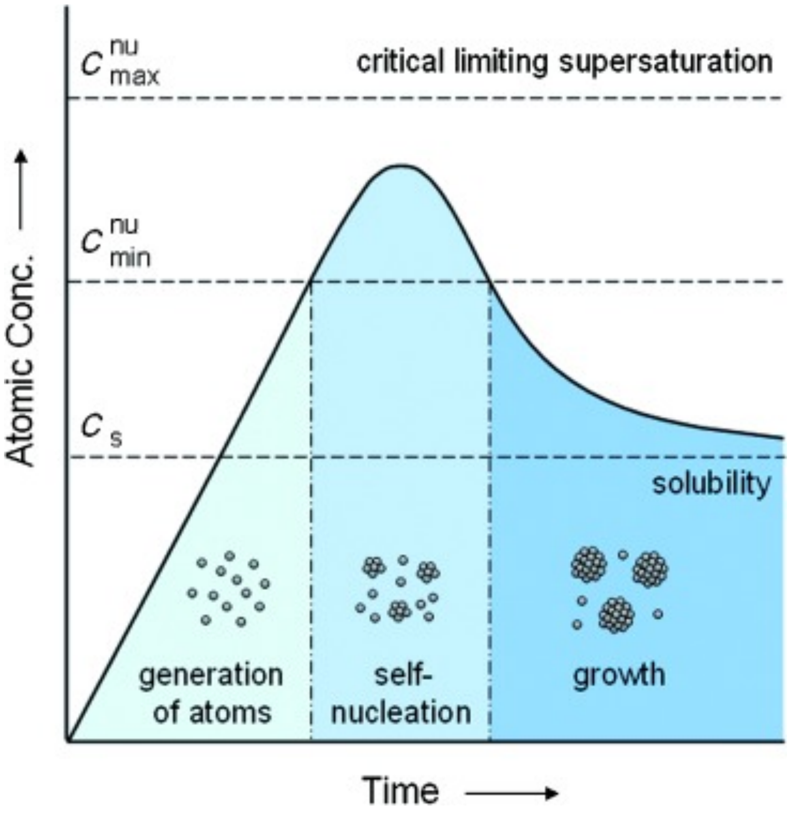

Figure 9. Graph depicting naoparticle nucleation as a function of concentration and time, where C_s refers to a solubility threshold in concentration terms, and C^{nu} min. and max. refer to minimum and maximum concentrations for the nucleation domain, respectively. Reproduced from [94] *with permission from Wiley, though figure adapted from originally published plot in* [95]*. Therefore, adapted here with permission from* [95]*. Copyright 1950 American Chemical Society.*

The second phase of nanoparticle synthesis is characterised by further growth, and the emergence of a stable, crystalline core or 'seed.' Seeds refer to clustered nuclei which have reached a critical size, beyond which their growth pattern is determined by the adoption of favoured structures, driven by a range of thermodynamic and kinetic parameters associated with crystallite electronics, reaction conditions, and solvent, surfactant or capping agent choice. In general terms, atoms in solution will continue to adsorb onto the growing crystallites where they undergo diffusion until they are included in the structure at a vacant step site. The emergence of fully fledged nanoparticles is determined at this stage by the dynamic balance between growth and dissolution of adsorbing atoms, with the rate of each process influenced by conditions which determine the bulk and surface energies of the crystallites [94]. The realisation of stable nanoparticles depends upon a final passivation step, in which nanocrystallite growth is terminated either through quenching the synthesis reaction or through the mediation of a surfactant or capping agent. This step is important in stabilising the nanoparticles in suspension, and in controlling their growth in order to prevent them agglomerating together [96].

Surfactants and other capping agents have therefore long been known to play a crucial role in determining the outcome of nanoparticle synthesis reactions. Their role in stabilising prepared nanoparticles typically involves coordinating to the surface of those particles as they grow. This can function either to direct the growth of those particles, for example if the capping agent coordinates preferentially to a specific facet of an emerging crystallite [94], or can prevent further particle growth altogether in the case of the coordination of molecules which exert strong steric or electrostatic repulsive forces [97].

Characterising nanoparticles is made inherently challenging by their small sizes. This is particularly true of efforts to study the early stages of nanoparticle synthesis reactions. There are limited opportunities available to researchers to follow the atomic-scale processes described in the preceding paragraphs, although some synchrotron X-ray studies have been undertaken to interrogate common theoretical understanding of these processes [98–100]. Bulk crystalline materials are also often studied using X-ray and neutron diffraction techniques, however given these techniques sample diffraction patterns from the whole specimen, rather than any nano-scale areas therein, their utility in characterising nanoparticulate materials can be limited, particularly in samples which might contain particles with multiple, different crystalline phases. In analysing the chemical and physical parameters of prepared nanoparticles [101], however, researchers regularly employ microscopy and spectroscopy techniques. Those of particular relevance to the current study are described hereafter.

Transmission electron microscopy (TEM) is a particularly useful technique for the study of nanoscale objects. Unlike macroscale objects, which interact with beams of light, and thus can be characterised using conventional optical microscopy, features in the nanoscale interact with smaller wavelengths of radiation. As such, electron beams are ideal for use in microscopy at the nanoscale [101]. In simple terms, a TEM consists of an electron generating gun, a column through which the electron beam passes, a sample stage which is inserted into the beam column, through which the electron beam is transmitted, then magnification, projection and observation systems which allow the user to visualise the image produced [102]. Electrons from the beam interact with the sample during irradiation, scattering off electrons within the nuclei in the sample atoms. Due to increased density of electrons, scattering increases with increasing atomic number. The transmitted beam passes through the objective and magnifying lenses of the microscope, forming the final image. That image reflects the degree of transmittance of the sample, and in bright field imaging, higher contrast can indicate lower transmittance, which is anticipated for higher atomic number components. Regions of a specimen with little or no sample appear bright [103]. TEM is particularly useful for studying the size, shape and morphology of nanoparticles, as well as analysing the dispersity of those properties within a suspension, and in interrogating adsorbates onto their surfaces [103]. That is the basis for using TEM in the current work.

In terms of spectroscopy, a particularly useful technique for studying the elemental composition of a material is X-ray photoelectron spectroscopy (XPS). XPS is a surface sensitive technique, and indeed appears to be the most widely used spectroscopic tool in surface science [104]. The function of XPS is based on the photoelectric effect, whereby core electrons are excited and subsequently emitted from a sample irradiated by a soft X-ray of energy hv. The ejected photoelectrons are measured by an electronic spectrometer, which records their kinetic energies (K_e). These kinetic energies are related to the binding energies (K_b) of the emitted electrons by:

$$K_b = hv - K_e - \emptyset$$

Equation 1. Equation relating the kinetic energies measured in an XPS spectrometer to the binding energies of the electrons emitted from the sample under study.

where $\emptyset$ is the workfunction of the spectrometer. As the binding energies are characteristic for the specific orbital from which the electron was emitted, these measured energies can be used to discern substantial insight regarding the electronic structure of the sample [105]. XPS can therefore be used to elucidate the elemental composition and the oxidation state of those elements present in the sample [106]. Spectroscopic scans can be carried out across broad ranges of kinetic energies in so called ‘survey scans,’ to evaluate and quantify at relatively low resolution the elemental composition of the whole sample. Higher resolution scans, however, can be focussed on the energy ranges associated with the binding energies of elements of interest, to acquire higher quality, quantitative insight into the composition, configuration and oxidative environment of the orbitals in question. The incident photoelectrons have limited penetration within the sample, to approximately 10 nm depth, and thus the technique is highly surface sensitive in its characterisation [107]. In this study, it is primarily used to interrogate the ratio of the metal elements within the alloy nanoparticles synthesised.

2.2 <u>Aims and Objectives</u>

This chapter concerns efforts towards preparing previously unreported RuSe@Pt nanoparticles, and accompanying work carried out to explore the chemical and physical properties, parameters and morphology of nanoparticle samples prepared in the pursuit of that aim. Key objectives for this work therefore include:

- The development of synthetic protocols which would deliver a controllable and reproducible route towards preparing nanoparticles with;
    - cores composed of RuSe coated with ultra-low loading, thin layers of Pt, likely 1-2 molecular layers thick;

    - known and controlled ratios of the three component elements;
    - good dispersion, with low levels of agglomeration, in stable suspensions;
    - tight size distributions, in the sub 10 nm range, in order to maximise active catalyst surface area;
- Insight into optimal means of controlling the morphology and dispersion of those nanoparticles, through the use of capping and stabilisation agents.

2.3 <u>Methods</u>

2.3.1 Synthesis of Nanoparticle Suspensions

A number of differing approaches towards nanoparticle synthesis were explored in the course of this work. Sequential and incremental synthetic optimisations were also pursued in improving the protocols described. These are summarised here, with discussion on the efficacy of these approaches following in the next section. The following section explains the rationale for developing each procedure.

2.3.1.1 CdSe Particles Synthesis

CdSe particles were synthesised following a published method [108]. All reagents were obtained from Sigma Aldrich. HPLC grade (99.99%) solvents were used. Se and Cd precursor solutions were prepared by dissolving 0.099 g selenium powder (100 mesh, > 99.9%) in 5.5 mL trioctylphosphine (technical grade, 90%)

(to prepare a 0.22 M Se solution) and 0.053 g cadmium acetate dehydrate (98%), with 0.6 mL oleic acid (> 99%), in 5.5 mL octadecene (technical grade, 90%) (to prepare a 0.04 M $Cd(CH_3CO_2)_2$ solution), respectively, in 25 mL round bottom flasks, with stirring. Using an oil bath on a hot plate, the Cd-containing flask was heated to 130 °C. A growth solution was prepared by adding 10 mL of octadecene and 0.67 mL of oleylamine (technical grade, 70%) to a 25 mL round bottom flask. The flask was then heated, also using the oil bath on the hot plate and with stirring, to 165 °C. Once the temperature of the growth solution had equilibrated, 1 mL of the Cd solution and 1 mL of the Se solution were added simultaneously and quickly, using a syringe. After eight minutes the hot plate was switched off and the CdSe solution was allowed to cool. The particles obtained were washed three times using a 50:50 de-ionised water:acetone solution, and collected by centrifugation. A Sigma 3k30 centrifuge was used, set to centrifuge the suspensions at 16000 revolutions per minute (RPM) at a temperature of 20 °C, for 30 minutes. The product particles were resuspended in 10 mL de-ionised water and stored in a labelled sample tube.

2.3.1.2 RuSe Particle Synthesis as per CdSe Protocol

A published method [108] was adapted to prepare RuSe particles. All reagents were obtained from Sigma Aldrich. HPLC grade (99.99%) solvents were used. Se and Ru precursor solutions were prepared by dissolving 0.099 g selenium powder (100 mesh, > 99.9%) in 5.5 mL trioctylphosphine (technical grade, 90%) (to prepare a 0.22 M Se solution) and 0.041 g ruthenium trichloride (99.98%), with 0.6 mL oleic acid (> 99%), in 5.5 mL octadecene (technical grade, 90%) (to prepare a 0.0359 M $RuCl_3$ solution), respectively, in 25 mL round bottom flasks, with stirring. Using an oil bath on a hot plate, the Ru-containing flask was heated to 130 °C. A growth solution was prepared by adding 10 mL of octadecene and 0.67 mL of oleylamine (technical grade, 70%) to a 25 mL round bottom flask. The flask was then heated, also using the oil bath on the hot plate and with stirring, to 165 °C. Once the temperature of the growth solution had equilibrated, 1 mL of the Ru solution and 1 mL of the Se solution were added simultaneously and quickly, using a syringe. After eight minutes the hot plate was switched off and the RuSe solution was allowed to cool. The particles obtained were washed three times using a 50:50 v/v de-ionised water:acetone solution, and collected by centrifugation. A Sigma 3k30 centrifuge was used, set to centrifuge the suspensions at 16000 RPM at a temperature of 20 °C, for 30 minutes. The product particles were resuspended in 10 mL water and stored in a labelled sample tube.

2.3.1.3 Pt Layer Deposition on RuSe Particles

A published method [109] was adapted to coat previously prepared RuSe particles with Pt. 2 mL of the previously prepared RuSe hydrosol were diluted using 50 mL of de-ionised water in a 100 mL roundbottom flask. The diluted hydrosol was refluxed, using a condenser, with stirring, at 110 °C for 30 minutes. A 0.1 M sodium citrate solution was prepared by dissolving 1.4705 g (>99%) in 50 mL deionised water. Of this, 8 mL were added to the refluxing solution, under continued heating for a further three minutes. A 0.05 M K_2PtCl_4 solution was prepared by dissolving 0.1038 g (98%) in 5 mL deionised water. Of this solution, 2 mL were added to the refluxing RuSe-hydrosol, under continued heating for a further 60 minutes. The refluxed RuSe@Pt solution was allowed to cool. The particles obtained were washed three times using a 50:50 v/v de-ionised water:acetone solution, and collected by centrifugation. A Sigma 3k30 centrifuge was used, set to centrifuge the suspensions at 16000 RPM at a temperature of 20 °C, for 30 minutes. The product particles were resuspended in 10 mL water and stored in a labelled sample tube.

2.3.1.4 RuSePt Particle Synthesis – Migration and Segregation Method

RuSePt nanoparticles were synthesised using a method adapted from a published protocol [79]. All reagents were obtained from Sigma Aldrich. HPLC grade (99.99%) solvents were used. 0.0207 g $RuCl_3$ (99.98%), 0.0485 g K_2PtCl_6 (99%) and 0.0078 Se powder (100 mesh, 99.9%) were dissolved in 1 mL of oleylamine (technical grade, 70%) in a sample tube to prepare a 0.1 M equivalent solution of the precursors. Using an oil bath on a hot plate, the mixture was heated at 120 °C for one hour, with stirring. 10 mL of oleylamine was also preheated in a roundbottom flask at 160 °C for one hour using another oil bath and hot plate. The temperature of the oil bath containing the oleylamine growth solution was increased to 230 °C. Once the temperature of the growth solution had reached 230 °C, the precursor solution was injected rapidly into the growth solution and then the resultant mixture was stirred for one hour with continued heating at 230 °C. The product particle suspension was washed three times in a 50% v/v ethanol:hexane solution and collected via centrifugation. A Sigma 3k30 centrifuge was used, set to centrifuge the suspensions at 16000 RPM at a temperature of 20 °C, for 30 minutes. The collected particles were suspended in 10 mL 50% v/v ethanol:hexane solution and stored in a labelled sample tube.

2.3.1.5 Surfactant Optimisation – Cetyltrimethylammonium bromide

Pt nanoparticles were synthesised using a method adapted from a published protocol [79]. All reagents were obtained from Sigma Aldrich. HPLC grade (99.99%) solvents were used. A 0.1 M Pt precursor solution was prepared by dissolving 0.0485 g K_2PtCl_6 (99%) in 1 mL of oleylamine (technical grade, 70%) in a sample tube. An excess (0.6930 g) of cetyltrimethylammonium bromide (CTAB) (> 98%) was added. Using an oil bath on a hot plate, the mixture was heated at 120 °C for one hour, with stirring. 10 mL of oleylamine was also preheated in a roundbottom flask at 160 °C for one hour using another oil bath and hot plate. The temperature of the oil bath containing the oleylamine growth solution was increased to 230 °C. Once the temperature of the growth solution had reached 230 °C, the precursor solution was injected rapidly into the growth solution and then the resultant mixture was heated for one hour with continued heating at 230 °C. The product particles were washed three times in a 50% v/v ethanol:hexane solution and collected via centrifugation. A Sigma 3k30 centrifuge was used, set to centrifuge the suspensions at 16000 RPM at a temperature of 20 °C, for 30 minutes. The collected particles were suspended in 10 mL 50% v/v ethanol:hexane solution and stored in a labelled sample tube.

2.3.1.6 Surfactant Optimisation – Oleic Acid

Pt nanoparticles were synthesised using a method adapted from a published protocol [79]. All reagents were obtained from Sigma Aldrich. HPLC grade (99.99%) solvents were used. A 0.1 M Pt precursor solution was prepared by dissolving 0.0485 g K_2PtCl_6 (98%) in 1 mL of oleylamine (technical grade, 70%) in a sample tube. 0.6 mL of oleic acid (> 99%) was added. Using an oil bath on a hot plate, the mixture was heated at 120 °C for one hour, with stirring. 10 mL of oleylamine was also preheated in a roundbottom flask at 160 °C for one hour using another oil bath and hot plate. The temperature of the oil bath containing the oleylamine growth solution was increased to 230 °C. Once the temperature of the growth solution had reached 230 °C, the precursor solution was injected rapidly into the growth solution and then the resultant mixture was heated for one hour with continued heating at 230 °C. The product particles were washed three times in a 50% v/v ethanol:hexane solution and collected via centrifugation. A Sigma 3k30 centrifuge was used, set to centrifuge the suspensions at 16000 RPM at a temperature of 20 °C, for 30 minutes. The collected particles were suspended in 10 mL 50% v/v ethanol:hexane solution and stored in a labelled sample tube.

2.3.1.7 Surfactant Optimisation – Excess Oleylamine

Pt nanoparticles were synthesised using a method adapted from a published protocol [79]. All reagents were obtained from Sigma Aldrich. HPLC grade (99.99%) solvents were used. A 0.02 M Pt precursor solution was prepared by dissolving 0.0485 g K_2PtCl_6 (98%) in 5 mL of oleylamine (technical grade, 70%) in a sample tube. Using an oil bath on a hot plate, the mixture was heated at 120

°C for one hour, with stirring. 10 mL of oleylamine was also preheated in a roundbottom flask at 160 °C for one hour using another oil bath and hot plate. The temperature of the oil bath containing the oleylamine growth solution was increased to 230 °C. Once the temperature of the growth solution had reached 230 °C, the precursor solution was injected rapidly into the growth solution and then the resultant mixture was heated for one hour with continued heating at 230 °C. The product particles were washed three times in a 50% v/v ethanol:hexane solution and collected via centrifugation. A Sigma 3k30 centrifuge was used, set to centrifuge the suspensions at 16000 RPM at a temperature of 20 °C, for 30 minutes. The collected particles were suspended in 10 mL 50% v/v ethanol:hexane solution and stored in a labelled sample tube.

2.3.1.8 RuSePt Particle Synthesis – Precursor and Molarity Optimisation

RuSePt nanoparticles were synthesised using a method adapted from a published protocol [79]. All reagents were obtained from Sigma Aldrich. HPLC grade (99.99%) solvents were used. 0.0796 g $Ru(C_5H_7O_2)_3$ ($Ru[acac]_3$) (99.5%), 0.0786 g $Pt(C_5H_7O_2)_2$ ($Pt[acac]_2$) (99.5%), and 0.0078 g Se powder (100 mesh, 99.9%) were dissolved in 5 mL of oleylamine (technical grade, 70%) in a sample tube to prepare a precursor solution with equivalent concentrations of 0.04 M Pt and Ru species, and 0.02 M Se. Using an oil bath on a hot plate, the mixture was heated at 120 °C for one hour, with stirring. 25 mL of oleylamine was also preheated in a roundbottom flask at 160 °C for one hour using another oil bath and hot plate. The temperature of the oil bath containing the oleylamine growth solution was increased to 230 °C. Once the temperature of the growth solution had reached 230 °C, the precursor solution was injected rapidly into the growth solution and then the resultant mixture was heated for one hour with continued heating at 230 °C. The product particles were washed three times in a 50% v/v ethanol:hexane solution and collected via centrifugation. A Sigma 3k30 centrifuge was used, set to centrifuge the suspensions at 16000 RPM at a temperature of 20 °C, for 30 minutes. The collected particles were suspended in 10 mL 50% v/v ethanol:hexane solution and stored in a labelled sample tube.

2.3.1.9 Pt and PtRu Nanoparticle Synthesis – Preparing Controls

In two separate procedures, Pt and PtRu nanoparticles were synthesised using a method adapted from a published protocol [79]. These particles were prepared as controls for further characterisation experiments. All reagents were obtained from Sigma Aldrich. HPLC grade (99.99%) solvents were used. 0.04 M equivalent precursor solutions were prepared, with 0.0786 g $Pt(C_5H_7O_2)_2$ ($Pt[acac]_2$) (99.5%), and 0.0796 g $Ru(C_5H_7O_2)_3$ ($Ru[acac]_3$) (99.5%) and 0.0786 g $Pt(C_5H_7O_2)_2$ ($Pt[acac]_2$) (99.5%) dissolved in 5 mL of oleylamine (technical grade, 70%) in sample tubes, respectively. The following steps were carried out in parallel for the two respective Pt and PtRu precursor mixtures. Using an oil bath on a hot plate, the resulting mixtures was heated at 120 °C for one hour, with stirring. 25 mL of oleylamine was also preheated in a roundbottom flask at 160 °C for one hour using another oil bath and hot plate. The temperature of the oil bath containing the oleylamine growth solution was increased to 230 °C. Once the temperature of the growth solution had reached 230 °C, the precursor solution was injected rapidly into the growth solution and then the resultant mixture was heated for one hour with continued heating at 230 °C. The product particles were washed three times in a 50% v/v ethanol:hexane solution and collected via centrifugation. A Sigma 3k30 centrifuge was used, set to centrifuge the suspensions at 16000 RPM at a temperature of 20 °C, for 30 minutes. The two sets of collected particles were suspended in separate 10 mL 50% v/v ethanol:hexane solution and stored in a labelled sample tube.

2.3.2 Chemical and Physical Characterisation of Nanoparticles

Characterisation techniques were employed to better understand the impact of the optimisation steps thus far described on the prepared nanoparticles.

2.3.2.1 Transmission Electron Microscopy (TEM)

Transmission electron microscopy imaging was also carried out across two distinct instruments due to availability and access restrictions. In both instances, in the days prior to arranged instrument time, as collected nanoparticle suspensions were diluted ten times in deionised water or ethanol, depending on the matrix in which they were suspended, and were sonicated for at least 20 minutes. Once well mixed, the suspensions were drop dried onto TEM grids acquired from EM Resolutions. In each case, one 10 µL drop was deposited per grid, with filter paper used to wick away excess solvent. To improve film deposition, the grids were dried under a lamp.

Preliminary TEM imaging was carried out using a Jeol 1200EX TEM at the Centre for Electron Microscopy at the University of Birmingham. The grids used for these imaging sessions were formvar/carbon film on copper, 300 mesh. The operating voltage used was 80 keV.

Subsequent, higher resolution imaging was carried out at the University of Nottingham Nanoscale and Microscale Research Centre. The grids used for these imaging sessions were graphene oxide on holey carbon films on 300 mesh copper. The microscope used was a Jeol 2100 FEG-TEM (field emission gun TEM), operated by Dr Michael Fay. Operating voltages ranged between 100 and 200 keV.

The images collected were used to size the nanoparticles prepared according to a protocol described previously [110], using ImageJ software. On average, the sizes of 100 nanoparticles were measured for each sample in order to provide a representative insight on particle size distribution. On average, these particles were counted from four distinct TEM images. This particle count threshold is below the range typically considered to provide statistically significant insight, which Pons *et al* suggest should be at least 500 particles, and ideally 100-1500 particles [111]. However, given the number of samples prepared and characterised, this number of particles analysed was considered to be sufficient to provide an indicative insight into particle size ranges.

2.3.2.2 X-Ray Photoelectron Spectroscopy (XPS)

X-ray photoelectron spectroscopy (XPS) measurements were carried out on two distinct instruments due to availability. CasaXPS software was used to fit the spectra generated and to carry out elemental analyses.

In both cases, thin films of nanoparticle suspensions were drop-dried onto silicon wafer chips in the days prior to arranged instrument time. Wafer chips approximately 1 cm^2 in size were cut using a diamond pencil. Aliquots of nanoparticle suspensions were withdrawn from previously prepared sample tubes, and sonicated for at least 20 minutes before drop drying. Whilst drop casting, the suspensions were added dropwise onto polished silicon chips and dried under a lamp, with duplicate wafers prepared for each sample.

The first batch of samples were measured using a Thermo Scientific K-Alpha instrument at Newcastle University in the Engineering and Physical Sciences Research Council funded NEXUS national XPS facility. The spectrometer was operated by Dr Naoko Sano. Spectra were recorded using a monochromatic Al Kα X-ray source, in three distinct spots on each wafer. In addition to survey scans, high resolution scans in the C 1s, O 1s, N 1s, Pt 4f, Se 3d, Ru 3p, and S 2p regions were recorded, with a step size of 0.1 eV.

Further measurements were carried out at the University of Nottingham Nanoscale and Microscale Research Centre on a Kratos AXIS ULTRA DLD instrument optimised for liquid phase measurements. The instrument was operated by Dr Emily Smith. Spectra were recorded using a high energy monochromated Ag source, in three distinct spots on each wafer. In addition to survey scans, high resolution scans in the C 1s, O 1s, N 1s, Pt 4f, Se 3d, Ru 3p, and S 2p regions were recorded, with a step size of 0.1 eV.

2.4 Results and Discussion

2.4.1 Two Step Synthesis Protocol

CdSe was identified early on in this study as a potential analogue for RuSe. CdSe quantum dots are well developed materials, having been prepared by researchers for a diverse range of applications including in light harvesting in sensitised solar cells [112], in biomedical diagnostics and sensing [113], and even in energy-generating coatings for glazing [114]. Given the relative maturity of CdSe quantum dot materials, a wealth of knowledge has also been generated regarding their preparation and handling. As such, a facile method for the fabrication of CdSe quantum dots [108] was reproduced and validated in the first stages of this work, as described in the previous section (synthesis 2.3.1.1). TEM images of the prepared nanoparticles are shown in Figure 10. The particles were relatively well dispersed, with limited evidence of aggregation, and adopted spherical morphologies. The average particle size in the sample was 6.2 ± 0.6 nm.

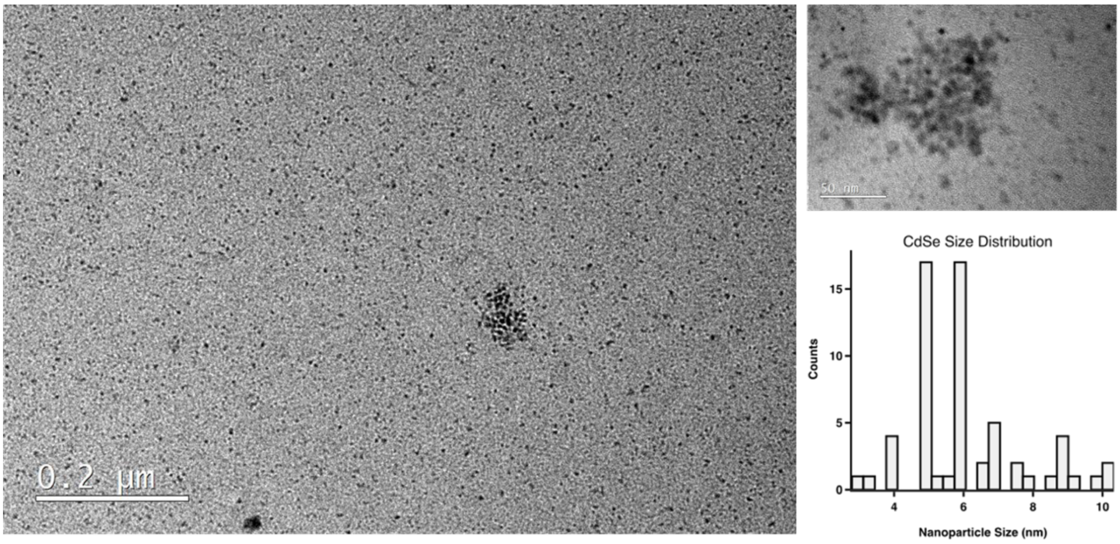

Figure 10. TEM images of prepared CdSe nanoparticles with histogram showing measured size distribution.

Having verified the method, it was adopted to produce RuSe nanoparticles. RuSe nanomaterials have been relatively well researched in their own right, having shown promise as durable and active catalysts for oxygen reduction at the cathode of methanol fuel cells [81–84, 115, 116], in which tolerance to methanol crossover from the anode is a key attribute of any candidate catalyst. As such, it was anticipated that once prepared, RuSe nanoparticles would be ideal, durable core materials for the intended RuSe@Pt catalysts. The validated CdSe method was therefore adapted as described (synthesis 2.3.1.2) for the preparation of RuSe nanoparticles. Further TEM images, Figure 11, show that these particles were also realised with relatively well controlled dispersion, though the size distribution is wider in this case. The average particle size was 19.1 ± 1.1 nm.

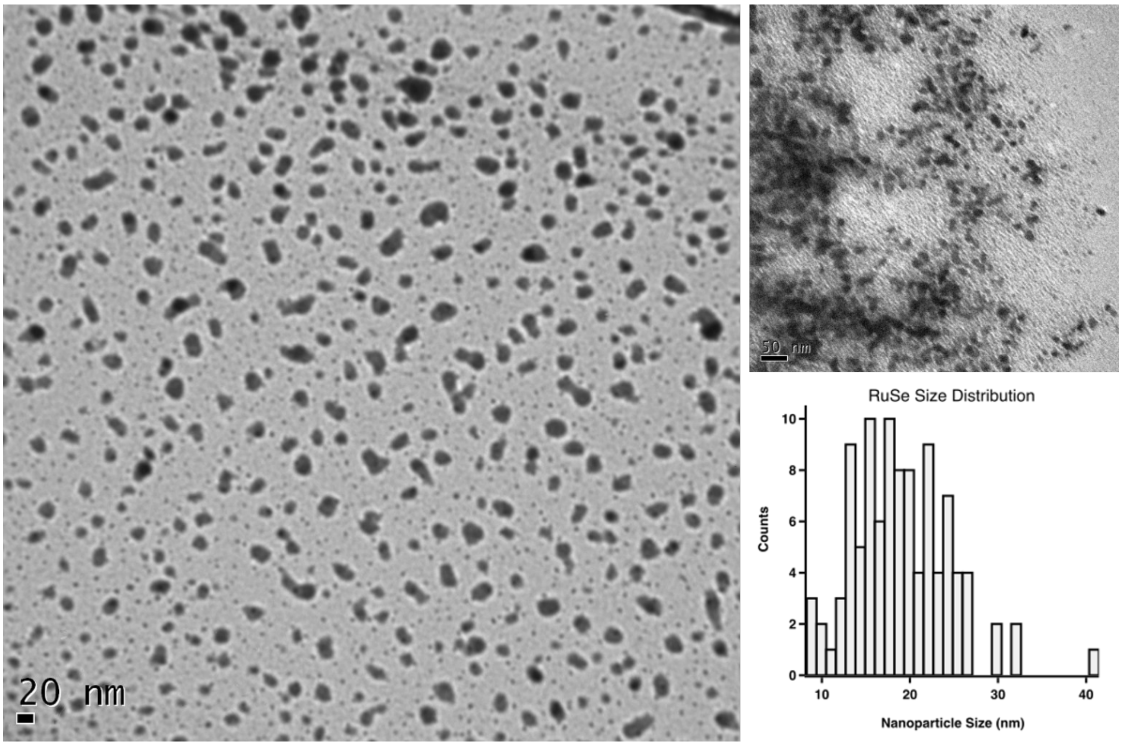

Figure 11. TEM images of the RuSe nanoparticles prepared, with histogram showing the particle sizes measured.

These RuSe nanoparticles were taken forward for further experimentation. A protocol was elaborated for a further synthetic step intended to coat those particles with a thin layer of Pt (synthesis 2.3.1.3). In this case, the protocol was adapted from a further published method [109], in which previously prepared CdSe nanoparticles had been coated with Pt. TEM images of the material produced, Figure 12, show clearly that the synthesis was unsuccessful. Instead of coating the RuSe particles with Pt, this protocol delivered an agglomerated mass of material. It is likely that heating the RuSe suspension resulted in further homogeneous reaction between those particles, causing them to grow further, alongside distinct and independent reduction of the Pt precursor, stabilised by the sodium citrate capping agent added to the refluxing solution. Such challenges likely explain the observation that of the other systems and synthetic procedures reported so far, the majority proceed via single step protocols. As such, a renewed approach was explored for preparing the target RuSe@Pt particles.

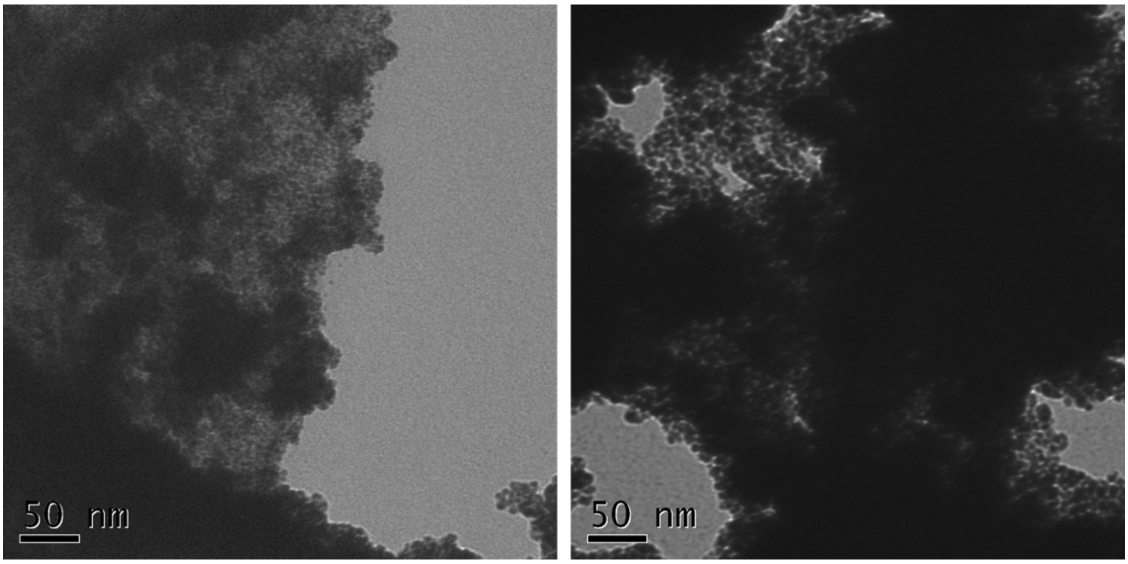

Figure 12. TEM images of would-be RuSe@Pt nanoparticles, demonstrating the failure of this two step synthesis procedure.

2.4.2 Migration and Segregation Method

An alternative, one-step synthetic protocol was investigated (synthesis 2.3.1.4), adapting a published method [79] which had been reported for the preparation of PtNi nanoframe catalysts. This approach concerned the use of oleylamine as both solvent and surfactant, to mediate nanoparticle growth, in a so called “hot injection” method. In hot injection synthesis, a mixture of solvated precursors are rapidly injected into a heated growth solution to facilitate fast nucleation of mixed alloy nanoclusters. The reported method generated nanoframe catalysts with Pt atoms segregated to the outer shell layers of the cluster, in a pseudo core@shell arrangement. This phenomenon and its potential application to the system of interest here is further discussed and characterised in the next chapter; the focus in this section is on the merits of the oleylamine-mediated synthetic protocol for the preparation of alloy nanoparticles which are hereafter referred to as ‘RuSePt,’ (rather than RuSe@Pt) given the lack of clarity at this stage as to whether a core@shell morphology has been adopted. TEM images were used to verify the success of the synthesis in terms of preparing particles with the anticipated dispersion and size distribution. These are shown in Figure 13. Average particle size was 3.3 ± 0.4 nm. The particles were spherical in nature.

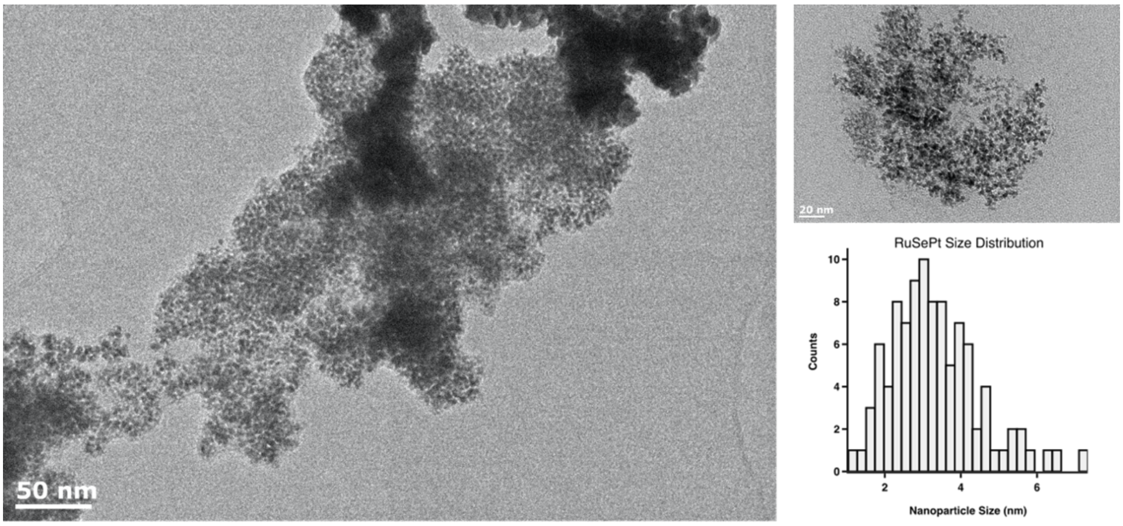

Figure 13. RuSePt alloy nanoparticles imaged using TEM, with a histogram showing measured size distribution.

Additionally, XPS was used to characterise the elemental composition and oxidation states of the elements present in the particles prepared. Spectra are shown in Figure 14. Analysis of these indicated that all three precursors had been reduced with varying degrees of success, Table 3, but that the three target elements had indeed been incorporated into the nanoparticles prepared. Nonetheless, the observed compositional ratio of those elements is very different to that expected. The low ratio of Ru is likely explained relatively simply by issues of poor solubility in the oleylamine solvent resulting in the delivery of a lower concentration of Ru precursor than anticipated. The surface-sensitivity of XPS may also mean that Ru is segregated to the inner layers of the material. The large concentration of silicon observed suggests that a relatively poor quality film of the sample was analysed, as this Si content is measured from the Si wafer support upon which the sample was deposited. The most significant finding from these experiments, however, is the excess of Se observed in the samples.

As XPS is a surface sensitive technique [104, 107], it was considered likely that these results indicated the presence of a surface layer or coating of Se. The 'Se Ox' band in the Se 3d spectrum, Figure 14, c, at a binding energy of ~58 eV, indicates the detection of oxidised Se, likely in the form of an SeO_2 film, which might negatively influence future catalysis using these particles. The small size of the particles made this a challenging assertion to test, however. In any case, the Se excess needed to be addressed in reviewing the precursor concentrations. Further challenges arose due to the difficulties in characterising Ru using XPS. The primary Ru orbital of interest is the Ru 3d orbital, however this overlaps very strongly in the XPS spectrum with the carbon C 1s orbital. With this in mind, spectra in the Ru 3p region were used in this and in all further XPS characterisation on these nanoparticle systems, with fitting parameters adapted from those proposed in a comprehensive study on Ru XPS [117]. Given the challenges described in solvating the $RuCl_3$ precursor in oleylamine, and the poorly resolved Ru 3p spectrum observed (Figure 14), further synthetic optimisation steps were indicated.

Table 3. Summary of atomic percentage values calculated from XPS survey spectrum on RuSePt nanoparticles.

	Atomic % of each Element						
Sample	**C 1s**	**O 1s**	**N 1s**	**Si 2p**	**Pt 4f**	**Ru 3p**	**Se 3d**
RuSePt	50.81 ± 2.31	17.59 ± 1.31	2.20 ± 0.31	22.55 ± 2.41	1.26 ± 0.21	0.68 ± 0.13	4.90 ± 0.80

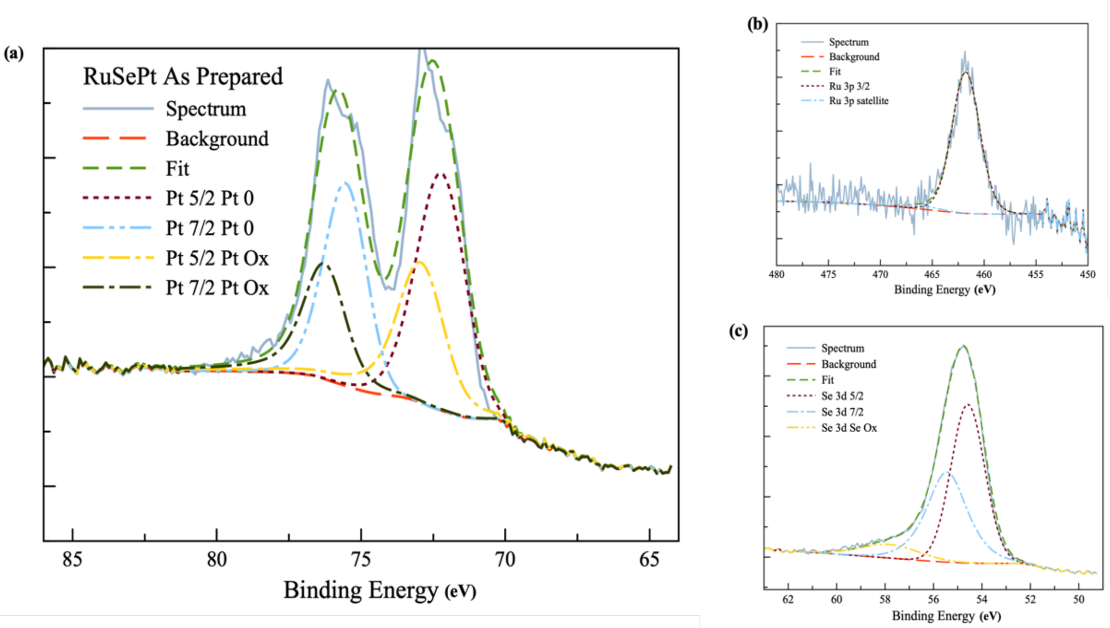

Figure 14. High resolution XPS spectra from the a) Pt 4f, b) Ru 3p, and c) Se 3d regions, from measurements on RuSePt nanoparticle samples. Where 'Pt 0,' refers to the components corresponding to metallic Pt, and 'Pt Ox,' refers to components corresponding to oxidised platinic species. 'Spectrum,' refers to the as-measured spectrum, and 'Fit,' refers to the line resulting from the fitting of the Pt spectrum components.

2.4.3 Incremental Optimisations and Preparing Standards

In pursuit of a method for reproducibly synthesising ideal RuSePt alloy nanoparticles, and relevant standard materials (Pt and PtRu nanoparticles) for experimental comparisons and benchmarking, further optimisation steps were undertaken. This incremental approach enabled multiple challenges to be addressed before settling on a final method which would be taken forward for further experimentation, including electrochemical characterisation of the catalyst nanoparticles. Although significant progress had been made in adopting the migration and segregation protocol described in the previous section, better dispersion of the nanoparticles was required for optimal catalysis in future experiments. With this in mind, work was undertaken to identify means of improving the stabilisation of the growing nanoparticles through testing alternative surfactant molecules. For simplicity, Pt nanoparticles were therefore synthesised in three batches (syntheses 2.3.1.5, 2.3.1.6, and 2.3.1.7), with oleic acid, cetyltrimethylammonium bromide (CTAB), and an excess of oleylamine used, respectively, as surfactant and/or capping agent. TEM images of the product particles are summarised in Figure 15. CTAB is sometimes referred to as a nanostructure ‘shape directing agent’ due to the strong influence it exerts over the morphology of product particles (and other structures) prepared when it is used. Notably, CTAB has been used to control the formation of gold nanorods [118], silver nanoparticles [119], and platinum nanoparticles [97]. It is curious that in this case, Pt nanorods were formed, Figure 15, b, with a high degree of agglomeration. Previous reports on the use of CTAB in oleylamine matrices have concerned the formation of a strongly sterically repulsive CTAB bilayer on the surface of growing nanostructures [120], and that these micelle-like formations have driven the growth of nanorods in other systems by directing growth in a single dimension [121]. Meanwhile, in mixed oleylamine-oleic acid systems, molecular dynamics simulations [122] have suggested an inverse relationship, in which an olelyamine bilayer may form around the nanostructure within an oleic acid matrix. As shown, however, Figure 15, a, the formation of truncated nanorods occurred in this case, with a high degree of agglomeration. The nanoparticles prepared using the excess oleylamine method, Figure 15, c, and histogram, d, had an average size of 12.3 ± 0.6 nm, with low polydispersity, good dispersion, and the adoption of spherical morphologies. Given the aim of enhancing control over the dispersion of the nanoparticles prepared, higher volumes of oleylamine were used in all of the syntheses which followed.

The enhanced dispersion associated with simply increasing the volume of oleylamine used in the synthesis encouraged a review of the precursor molarities used hereafter. It is worth highlighting at this stage the observation that the synthetic method could be tailored to deliver enhanced control over the morphology and dispersion of the nanoparticles by modifying the precursor molarity, rather than by increasing the complexity of the reaction by adding a further surfactant.

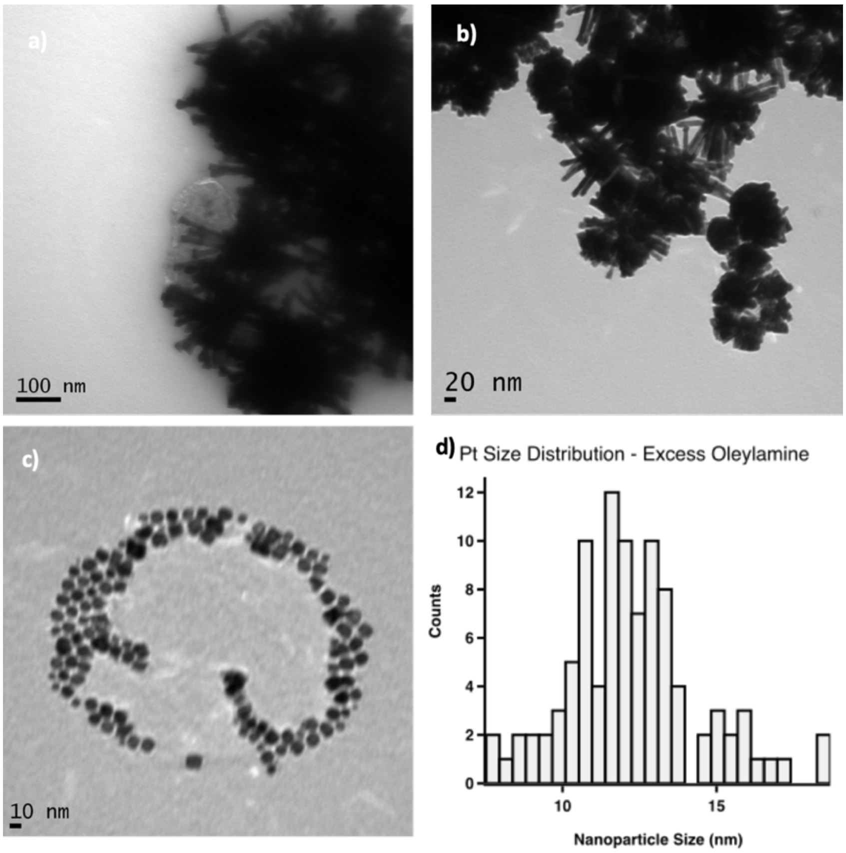

Figure 15. TEM images of Pt nanostructures prepared using varying surfactants, with a) oleic acid, b) CTAB, and c) excess oleylamine. d) shows a histogram of the size distribution of the excess oleylamine case.

Further iterations of the protocol concerned addressing the solubility challenges observed with $RuCl_3$ in the oleylamine matrix, and reducing the concentration of Se precursor used in order to rebalance the ratios of the elements seen in the product particles prepared. Finally, a fully optimised synthetic procedure (synthesis 2.3.1.8) was arrived at and used for all further syntheses. Acetylacetonate Pt and Ru precursors, $Pt[acac]_2$ and $Ru[acac]_3$, were used, with enhanced solubility observed for both in the oleylamine solvent. RuSePt particles prepared using this method are shown in Figure 16, a and b, with histogram, c. They measured 4.4 ± 0.5 nm on average with a mixed morphology, where some nanoparticles in the sample adopted a cubic shape, while others were spherical in configuration. Although these particles are more agglomerated than the Pt standards prepared prior (Figure 15), they were within the desired size range (< 10 nm) and as the histogram (Figure 16, c) suggests, the distribution of their sizes was relatively tight and well controlled. This protocol was adapted (synthesis 2.3.1.9) to produce batches of standard or benchmark Pt and PtRu nanoparticles, for further characterisation. TEM images demonstrating the dispersion and size distributions of these particles are also included in Figure 16 with the Pt particles shown in d, and histogram showing their size distribution, f, and the PtRu particles shown in image e, and histogram g. Both sets of particles are more homogeneous in morphology than in the RuSePt case, with spherical morphologies adopted by the particles, which are also small and in tight size distribution. The PtRu particles are the less agglomerated of the two. These three nanoparticle systems were taken forward for further characterisation and testing.

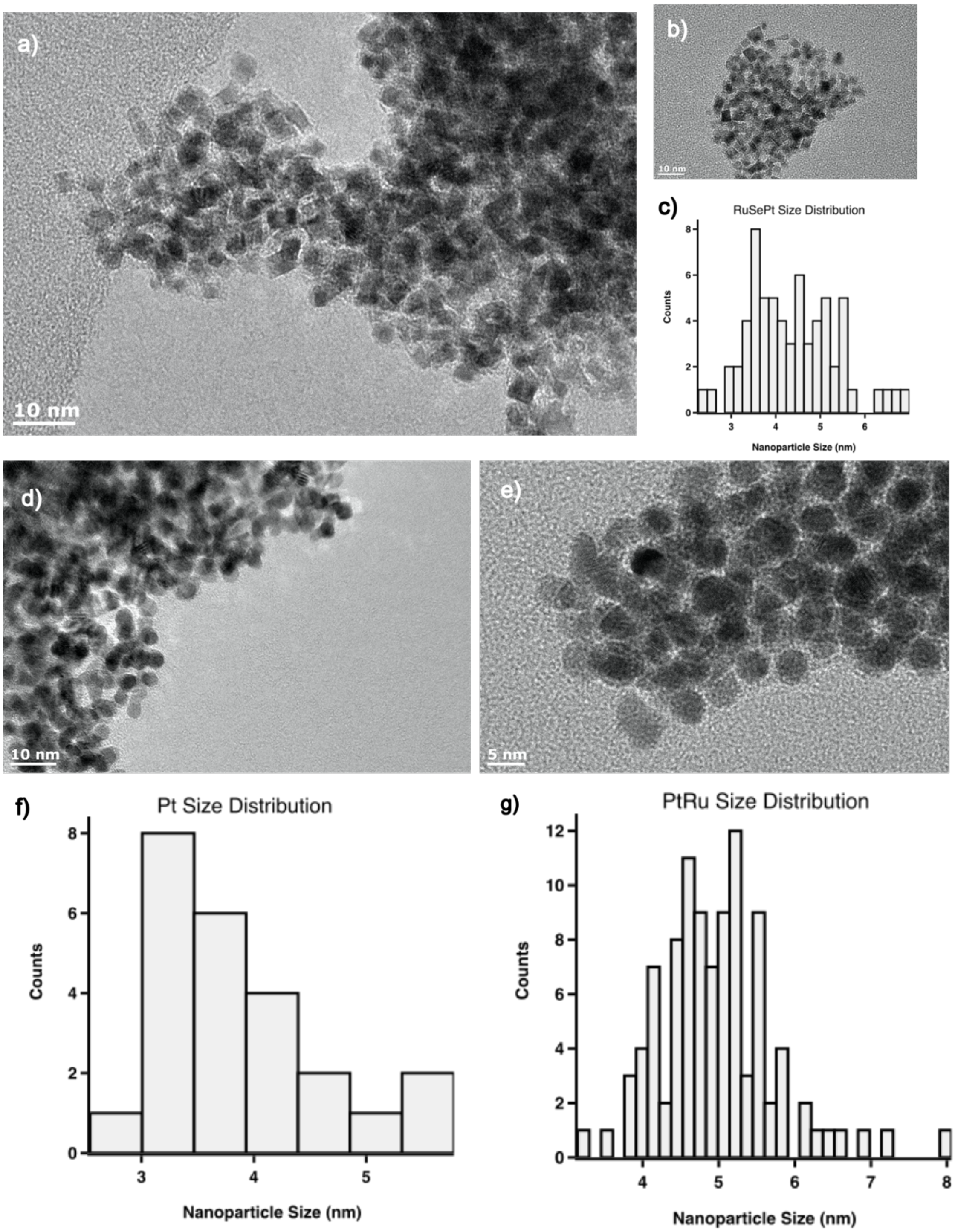

Figure 16. TEM images and histograms of optimised nanoparticles, with a) and b) RuSePt with [acac] precursors, and c) showing the measured size distribution for these. d) shows Pt and e) shows PtRu nanoparticles prepared with the optimised method. Histograms f) and g) show their measured size distributions, respectively.

2.5 Conclusions

The work described thus far concerned a sequence of incremental improvements intended to deliver a reliable and controlled protocol for the preparation of a novel nanoparticle composition, namely RuSePt nanoparticles, and appropriate Pt and PtRu standards. An optimised synthetic protocol was developed, in which acetylacetonate precursors Pt[acac]$_2$ and Ru[acac]$_3$, with Se powder, were dissolved in oleylamine, which served multiple roles as solvent, reducing agent and surfactant. Optimisation steps have been discussed in the development of this protocol, with precursor and surfactant choice having been identified as key considerations.

Observations made in the course of these optimisation steps may prove insightful for researchers seeking to develop synthetic procedures aimed at preparing well controlled nanoparticles. It is worth highlighting that the successful interventions described concerned simplifying the reactions concerned; moving from a two-step synthetic procedure involving phase transfer of prior prepared nanoparticle suspensions, to a one pot, one step method improved handling of the nanoparticles. Although complex surfactant mixtures were considered, based on published reports of their successful use, the biggest improvement in control of nanoparticle dispersion and morphology was subsequently realised by simply using a larger volume of surfactant in each synthesis. This finding makes clear the value of carefully considering and indeed optimising surfactant volumes and thus precursor molarities in developing nanoparticle synthetic protocols. The findings reported here could contribute to improved understanding of the role of those molarities in controlling product nanoparticle size and shape, as other researchers have reported [123].

The first expressed aim for this chapter focussed on preparing RuSe@Pt nanoparticles with thin Pt shells overlayed on previously prepared, stable and durable RuSe nanoparticles. As discussed, the two-step procedure intended to synthesise nanoparticles in this configuration proved unsuccessful. It was deemed worthwhile to pursue alternatives. At this stage in the process of conducting this research it was unclear which configuration the three elements in the prepared nanoparticles had adopted, and hence they were referred to as RuSePt nanoparticles so as not to be misleading in convention. Efforts to further characterise the prepared nanoparticles, and to understand the segregation behaviour of the atoms contained therein are discussed in the next chapter.

3 Efforts Towards Controlling the Morphology and Surface Composition of RuSePt Nanoparticles

3.1 Background and Context

This chapter concerns means of exerting control over the surface chemistry of the nanoparticles prepared. The surface composition is very influential in determining the availability of active sites for catalysis, and thus in shaping the utility of the materials as catalysts. Naturally these optimisation efforts begin with the synthesis protocol used to prepare the nanoparticles, as has been discussed in detail in the previous chapter. Further synthetic considerations are detailed briefly here before turning to post-synthetic treatments and handling protocols which have been developed by researchers seeking to optimise their catalysts.

In order to contextualise some of the work which follows it is worth briefly here revisiting the notion that the choice of precursors and surfactant used in a given nanoparticle synthesis can strongly influence the shape and configuration of the product particles. This is discussed in detail in the prior chapter.

Once researchers have celebrated the successful preparation of their desired nanoparticle catalysts, a myriad series of considerations emerge regarding post-synthetic handling and treatment protocols. A number of approaches towards optimising catalytic surfaces are reviewed here, prior to reporting on attempts to apply these techniques to the nanoparticle system thus far described.

Porous nanostructures are a subclass of materials considered in modern nanocatalyst development. In heterogenous applications in which solid phase catalysts are involved in mediating gas phase reactions, porosity can enhance the activity of the catalyst by improving gas flow and thus reactant supply and cycling [124]. Acid treatment or leaching protocols aiming to selectively degrade non-noble catalyst components have been developed, in order to enhance both porosity but also mass of active, noble metal per mass area of catalyst surface [76, 79, 125, 126].

The important role that surfactants and capping agents play in nanoparticle synthesis has already been discussed in detail. Another important aspect is the influence that those surface ligands have over the electrochemistry and catalytic activity of the nanostructures stabilised. Some limited research has shown that careful surfactant selection can lead to enhanced catalytic activity [127, 128], however the majority of references to this topic in the scientific literature relate to the potential that surfactants have to ‘poison’ catalysts, by blocking all-important active sites, where catalytic reactions occur [129, 130]. Indeed, dedicated methods have been developed to aid researchers in efficiently removing surfactants from catalyst nanoparticle surfaces [131]. More broadly, however, published reports of novel, improved catalysts often now include an annealing or heat treatment step, in which the catalyst powders are heated at high temperatures (often up to 700 °C) to engender enhanced chemical ordering in alloys, and to remove surfactants and other surface ligands to reveal pristine catalyst surfaces [73, 132]. Given the supply of energy associated with heating, annealed nanoparticles are prone to sintering and agglomeration in the course of heat treatment [133], and managing and preventing this is another sub-theme of research in this area. Most protocols include flowing reductive gas over the powder surfaces during heating, in order to minimise oxidative degradation [84].

Given the scope and complexity of the controls and treatment protocols envisaged, a broader range of characterisation techniques than described in the prior section have been employed by other researchers, and were drawn upon in the work which follows, in seeking to understand the impact of the interventions described.

So called ‘inherent electrochemistry’ experiments have been used to study a range of chemical surfaces [134–136], with a view to understanding what is essentially the passive electroactivity of the material; the oxidation or reduction of the surface itself in response to the application of oxidative or reductive potentials. Of particular relevance to the current study was a thorough study of the inherent electrochemistry of platinum dichalcogenides, PtS_2, $PtSe_2$ and $PtTe_2$ [137]. The researchers observed a characteristic oxidative signal at 0.8 V (vs. Ag/AgCl) for $PtSe_2$ films, associated with the formation of high oxidation states of Se, likely including $HSeO_3^-$, SeO_3^{2-}, SeO_4^{2-} species. Reference to this study is drawn in the work which follows, in providing an insight into the electronic character of the nanocatalyst powders prepared.

The theoretical underpinning and background for the use of X-ray photoelectron spectroscopy (XPS) and transmission electron microscopy (TEM) was described in detail in the previous chapter. Briefly, in XPS, a soft X-ray is used to irradiate a sample surface, where it facilitates the ejection and emission of core level electrons from the material under study. The energy of those emitted electrons is recorded by a spectrometer, and is characteristic of the element and orbital from which the electron has been ejected. XPS is therefore particularly useful for studying the elemental composition of the material under study, and provides insight into its electronic characteristics and oxidation state. TEM involves inserting prepared samples into an electron beam and measuring the electrons transmitted through, using magnetic lenses and visualisers to generate a microscopy image of the sample under investigation. In bright field mode, regions within the specimen which are blank of sample appear bright, while regions with deposited sample appear dark. The relative darkness relates to the contrast, associated with the atomic number of the deposited material, as well as the density of the film deposited. TEM is used to visualise the morphology and configuration of the sample, and in the current work is employed in particular to scrutinise the dispersion and size distribution of the prepared nanoparticles.

Bright field is the standard mode of operation for traditional TEM imaging. This technique is particularly valuable for obtaining information regarding the context of the material under study and the matrix within which it is dispersed or deposited. In the nanoparticle case TEM is also very useful in providing an easy to achieve overview of a large number of particles, representative of a wider sample. However, detail regarding the composition of those particles can be lost due both to the typical lack of resolution between broadly similar chemical components within the sample (for example, different transition metal components of alloy nanoparticles are indistinguishable), and also due to noise in the instrumentation [138]. Another electron microscope variant, the scanning transmission electron microscope (STEM) has been optimised to mitigate these concerns. Figure 17 illustrates the operational mode of STEM, and the interrelation of its associated components. Briefly, the probe of the microscope is rastered over the specimen surface, where it conveys the convergent beam through the sample. The beam interacts with the sample, facilitating the generation of a number of signals. The scanning of the probe across the surface enables the collection of each signal evolved with high spatial resolution. As such, maps can be generated denoting the composition and morphology of the sample under study, in what Meurig Thomas and colleagues have described as “nanoscale cartography,” [139]. A key feature of STEM that is denoted in Figure 17 is the capacity to selectively collect highly scattered electrons through the annular dark field (ADF) detectors in High Angle Annular Dark Field STEM (HAADF-STEM). In this operating mode the image noise is reduced and high fidelity images can be captured, particularly of metallic nanoparticles and other nanostructures, which appear bright [138]. These characteristics make HAADF-STEM an ideal technique for studying nanoparticle structure and morphology, as well as in gathering insight into the nanoparticle environment as in bright field TEM [101].

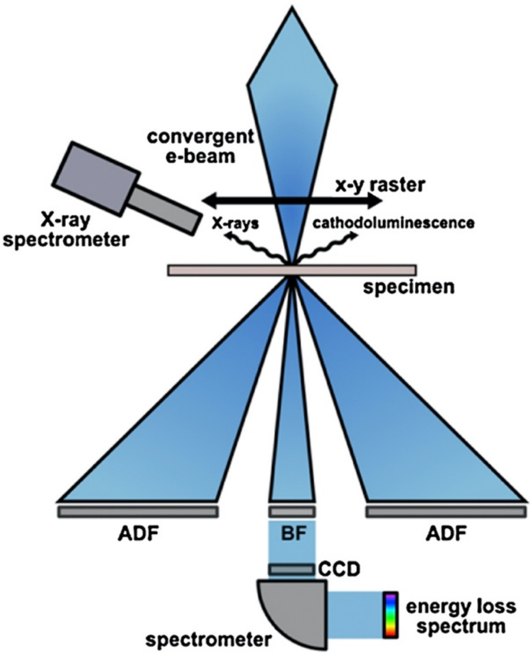

Figure 17. Diagrammatic representation of a scanning transmission electron microscope, where ADF refers to annular dark field, BF refers to bright field, and CCD refers to a charge-coupled device camera. Reproduced from [139], *https://doi.org/10.1016/j.cplett.2015.04.048, under Creative Commons License (CC BY-NC-ND 4.0).*

A sub-category of STEM instrumentation of great importance to this work is the aberration corrected microscope. Defects in the microscope lenses cause artefacts known as aberrations. Most electron microscopes are subject to spherical aberrations in their objective lenses, which is the lens located after the sample in the microscope column [101]. These aberrations are inherent to the round shape of the lens. Corrective intervention can be made to improve the aberration by including additional optical components, including non-round lenses, as well as by introducing autocalibrative systems to the microscope to right aberrations arising due to poor microscope alignment [140]. Aberration corrected STEM instruments can achieve sub-atomic resolution imaging, which is relatively self-evidently of great utility to researchers working with nanomaterials. With even further improved noise, resolution and image fidelity arising from aberration correction, these instruments can for example be used to differentiate metals in segregated nanoalloys as a result of being able to visualise atomic scale variances in lattice structure and the brightness associated with differing atomic number [88].

Figure 17 also shows the non-microscopy components of a typical STEM instrument, the spectroscopes. Many STEM instruments are equipped with spectrometers optimised for energy dispersive X-ray spectroscopy (EDXS) and electron energy-loss spectroscopy (EELS) measurements. EDXS and EELS can completement the structural and morphological insight provided by STEM imaging with mapped-on spectral information on the chemical composition and characteristics of the sample under study. Instruments capable of tomographical EDX have been developed recently, in which multiple detectors are used to collect maps from all angles which can be computed together to form a three dimensional model of the composition of a sample [141]. STEM-EDX measurements on nanoparticles, and in particular nanoparticles stabilised with organic surfactants, can be challenging, however. The probe dwell time required to conduct the required spectroscopic measurements can supply excessive amounts of energy to the specimen surface, encouraging nanoparticle agglomeration and degrading surfactant layers. EELS instruments can acquire atomic resolution chemical maps more quickly and more efficiently than EDXS instruments, resulting in lower electron doses and indeed higher resolution outputs due to reduced noise. State of the art aberration corrected STEMs with EELS detectors can even be used to acquire maps with atomic scale resolution without displacing the atoms under study [140]. STEM-EELS was used to investigate the configuration and segregation behaviour of the atoms in the nanoparticles prepared in this study. Those experiments are discussed further in this chapter.

3.2 Aims and Objectives

The focus of this chapter is on means of exerting additional levels of control over the composition, configuration, structure and, in particular, surface morphology of the nanoparticles prepared. The work described here sought to understand how synthetic conditions and post-synthesis treatments could be used to prepare nanoparticles with characteristics anticipated to confer enhanced catalytic activity. Key aims for this portion of the study concern;

- understanding the effect and efficacy of attempts to tweak the composition of the prepared nanoparticles by varying the molar ratios of the chemical precursors used;
- identifying alternative post-synthesis routes towards engendering control over the surface configuration of the nanoparticles, and the segregation or otherwise of the ions of each constituent element therein;
- verifying the efficacy of these approaches, and the broader impacts that they have on the nanoparticle systems concerned, in order to provide insight into optimal strategies for handling catalyst nanoparticles;
    - through employing a broad range of characterisation techniques, to better understand the chemical and physical phenomena shaping the impacts observed.

3.3 Methods

3.3.1 Synthesis and Post-Synthesis Treatment of Nanoparticle Suspensions

Building on the synthetic work described in the previous chapter, this section relates to the methodology underpinning a range of interventions and treatments aimed at exerting further control over the parameters of the nanoparticles prepared. A synthesis procedure with decreased Se molarity was developed in order to prepare RuSePt particles with low Se content. Thereafter, acid and heat treatment protocols were adopted to modify the surface configuration of the prepared particles.

3.3.1.1 RuSePt Nanoparticle Synthesis – Low Se Content

RuSePt nanoparticles were synthesised using a method adapted from a published protocol [79]. All reagents were obtained from Sigma Aldrich. HPLC grade (99.99%) solvents were used. 0.0796 g $Ru(C_5H_7O_2)_3$ ($Ru[acac]_3$) (99.5%), 0.0786 g $Pt(C_5H_7O_2)_2$ ($Pt[acac]_2$) (99.5%), and 0.0008 g Se powder (100 mesh, 99.9%) were dissolved in 5 mL of oleylamine in a sample tube to prepare a precursor solution with equivalent concentrations of 0.04 M Pt and Ru species, and 0.002 M Se. Using an oil bath on a hot plate, the mixture was heated at 120 °C for one hour, with stirring. 25 mL of oleylamine was also preheated in a roundbottom flask at 160 °C for one hour using another oil bath and hot plate. The temperature of the oil bath containing the oleylamine growth solution was increased to 230 °C. Once the temperature of the growth solution had reached 230 °C, the precursor solution was injected rapidly into the growth solution and then the resultant mixture was heated for one hour with continued heating at 230 °C. The product particles were washed three times in a 50% v/v ethanol:hexane solution and collected via centrifugation. A Sigma 3k30 centrifuge was used, set to centrifuge the suspensions at 16000 RPM at a temperature of 20 °C, for 30 minutes. The collected particles were suspended in 10 mL 50% v/v ethanol:hexane solution and stored in a labelled sample tube.

3.3.1.2 Acid Treatment

Previously prepared nanoparticle suspensions were treated with acetic acid according to a protocol developed by adapting a published method [79]. 2 mL of the previously prepared RuSePt nanoparticle suspensions were mixed with 0.1 mL of oleylamine in a roundbottom flask. 2 mL of acetic acid (> 99.7%) was added to the flask and the resulting solution was heated at 90 °C for two hours using an oil bath on a hot plate, with stirring. After heating, the treated nanoparticle suspensions were washed three times in a 50% v/v ethanol:hexane solution and collected via centrifugation. A Sigma 3k30 centrifuge was used, set to centrifuge the suspensions at 16000 RPM at a temperature of 20 °C, for 30 minutes. The collected particles were suspended in 10 mL 50% v/v ethanol:hexane solution and stored in a labelled sample tube.

3.3.1.3 Deposition of Nanoparticles on Carbon Black

For subsequent heat treatment and electrochemistry experiments, it was necessary to deposit the nanoparticles prepared previously onto carbon black support materials. Vulcan XC 72 carbon black powder manufactured by Tanaka Kikinzoku International (TKK) was acquired from Fuel Cells Store and was used as received. The carbon black powder is hereafter referred to as ‘TKK carbon black.’ 1 mg of TKK carbon black powder was used to disperse 1 mL of nanoparticle suspension in each case. In a typical preparation, the desired volume of nanoparticle suspension was measured out into a sample tube, into which the corresponding mass of TKK carbon black was added. The mixture was sonicated for 30 minutes, before being washed once in a 50% v/v ethanol:hexane solution and collected via centrifugation. A Sigma 3k30 centrifuge was used, set to centrifuge the suspension at 16000 RPM at a temperature of 20 °C, for 30 minutes. The collected suspension was then decanted into a petri dish, partially covered and then dried in a vacuum oven at 80 °C overnight. The dried powder was collected into a labelled sample tube.

3.3.1.4 Heat Treatment

A published method [132] was adapted to develop a heat treatment protocol. The nanoparticles-on-carbon powders prepared previously were each heat treated at two temperatures, 250 °C and 500 °C. In each case, the powder was weighed into an alumina crucible and loaded into a tube furnace, which was sealed. 4% hydrogen in argon gas was then flushed through the tube while the furnace was heated at a rate of 10 °C per minute up to the desired temperature. Once the target temperature had been reached, this was held for six hours with continuous flow of gas. The furnace was programmed to cool to room temperature under gas flow. Once cool, the annealed powders were removed.

3.3.2 Chemical and Physical Characterisation

Given the range of treatments described, elucidative analysis of the chemical and physical impacts of those treatments was required. A range of techniques were drawn upon to better understand the efficacy of the interventions made, and the phenomena underpinning their relative success. This section concerns the methodologies associated with employing those characterisation techniques.

3.3.2.1 Inherent Electrochemistry

A published method [137] was modified. Samples taken from the previously prepared nanoparticle suspensions were readied for measurement by sonication, for 15 minutes. The working electrode was prepared by drop casting 10 µL of sonicated nanoparticle suspension onto a 5 mm glassy carbon (GC) rotating disk electrode tip, which was subsequently dried under a lamp. Meanwhile, the platinum mesh counter electrode and double junction Ag/AgCl reference electrode were cleaned using distilled water, before being assembled in a previously acid washed 150 mL three electrode glass cell. The background electrolyte used for these measurements was phosphate buffered saline (PBS) solution, pH 7, used as received from Sigma Aldrich. 150 mL of PBS was added to the cell before the three electrodes were assembled, using a Pine Instruments rotating disk electrode rotator arm to connect to the Autolab PGSTAT302N potentiostat, which had been acquired from Metrohm. Measurements were carried out at room temperature (25 °C). Nova 2.0 software was used to control the potentiostat and record the currents generated in response to the potentials applied. All potentials referred to here and reported hereafter are relative to Ag/AgCl. The electrolyte was purged with flowing nitrogen for 30 minutes before measurements were recorded. Nitrogen bubbles were dislodged from the electrode surface by rotating the arm at 800 RPM. A scan rate of 100 mV per second was used for all measurements. Measurements were run from −1.8 V towards 1.8 V, followed by a reverse sweep back to −1.8 V.

3.3.2.2 Transmission Electron Microscopy (TEM)

Transmission electron microscopy imaging was also carried out across two distinct instruments due to availability and access restrictions. In both instances, in the days prior to arranged instrument time, as collected nanoparticle suspensions were diluted ten times in deionised water or ethanol, depending on the matrix in which they were suspended, and were sonicated for at least 20 minutes. Once well mixed, the suspensions were drop-dried onto TEM grids acquired from EM Resolutions. In each case, one 10 μL drop was deposited per grid, with filter paper used to wick away excess solvent. To improve film deposition, the grids were dried under a lamp.

Preliminary TEM imaging was carried out using a Jeol 1200EX TEM at the Centre for Electron Microscopy at the University of Birmingham. The grids used for these imaging sessions were formvar/carbon film on copper, 300 mesh. The operating voltage used was 80 keV.

Subsequent, higher resolution imaging was carried out at the University of Nottingham Nanoscale and Microscale Research Centre. The grids used for these imaging sessions were graphene oxide on holey carbon films on 300 mesh copper. The microscope used was a Jeol 2100 Field Emission Gun-TEM (FEG-TEM), operated by Dr Michael Fay. Operating voltages ranged between 100 and 200 keV.

The images collected were used to size the nanoparticles prepared according to a protocol described previously [110], using ImageJ software. On average, the sizes of ~100 nanoparticles were measured for each sample in order to provide a representative insight into particle size distribution. On average, these particles were counted from four distinct TEM images. This particle count threshold is below the range typically considered to provide statistically significant insight, which Pons *et al* suggest should be at least 500 particles, and ideally 100-1500 particles [111]. However, given the number of samples prepared and characterised, this number of particles analysed was considered to be sufficient to provide an indicative insight into particle size ranges.

3.3.2.3 X-ray Photoelectron Spectroscopy (XPS)

X-ray photoelectron spectroscopy (XPS) measurements were carried out at the University of Nottingham Nanoscale and Microscale Research Centre. CasaXPS software was used to fit the spectra generated and to carry out elemental analyses.

Thin films of nanoparticle suspensions were drop-dried onto silicon wafer chips in the days prior to arranged instrument time. Wafer chips approximately 1 cm^2 in size were cut using a diamond pencil. Aliquots of nanoparticle suspensions were withdrawn from previously prepared sample tubes, and sonicated for at least 20 minutes before drop drying. Whilst drop casting, the suspensions were added dropwise onto polished silicon chips and dried under a lamp, with duplicate wafers prepared for each sample.

A Kratos AXIS ULTRA DLD instrument optimised for liquid phase measurements was used. The instrument was operated by Dr Emily Smith. Spectra were recorded using a high energy monochromated Ag source, in three distinct spots on each wafer. In addition to survey scans, high resolution scans in the C 1s, O 1s, N 1s, Pt 4f, Se 3d, Ru 3d, Ru 3p, and S 2p regions were recorded, with a step size of 0.1 eV.

3.3.2.4 Scanning Transmission Electron Microscopy and Electron Energy Loss Spectroscopy (STEM-EELS)

Scanning Transmission Electron Microscopy (STEM) imaging and Electron Energy Loss Spectroscopy (EELS) spectroscopic measurements were carried out at the SuperSTEM facility operated by the Science and Technology Facilities Council on the Sci-Tech Daresbury campus in Cheshire.

In the days prior to arranged instrument time, as collected nanoparticle suspensions were diluted ten times in ethanol, and were sonicated for at least 20 minutes. Once well mixed, the suspensions were drop-dried onto TEM grids acquired from EM Resolutions. Imaging and EELS measurements focussed on the as prepared RuSePt samples. These were deposited on ultra-low background silicon grids, with one 2 µL drop sufficient volume per grid. The excess solvent was carefully wicked away using filter paper and the grids were dried under a lamp. To improve film deposition, the grids were dried under a lamp.

The SuperSTEM 3 microscope was used. SuperSTEM3 is a Nion UltraSTEM^{TM} 100 MC 'Hermes' microscope, equipped with an ultra-high vacuum

Gatan Enfinium spectrometer for EELS measurements, an ultra-stable sample stage and an in-vacuum sample holder magazine. Dr Eric Prestat operated the microscope. The operating voltage used was 100 kV.

3.4 Results and Discussion

A naming convention has been adopted to differentiate the nanoparticle systems described hereafter, in this chapter and the next. This is summarised for reference in Table 4. The table is laid out chronologically in the order in which the particles were prepared and characterised, with the exception that an initial batch of 'RuSePt High' nanoparticles were acid treated in a preliminary experiment which inspired the rest of the work described here. This is discussed in detail in the acid treatment section.

Table 4. Summary of the samples under study in this chapter and the next, and the naming convention adopted to differentiate them from one another. 'High' and 'Low' refer to concentrations of selenium precursor. '/C' refers to nanoparticles loaded onto carbon supports. 'Acid' refers to the samples having been acid treated, and '250 °C' or '500 °C' refers to the samples having undergone heat treatment at the corresponding temperature.

	Molarity of Precursors of each Element						
Name	**Ru**	**Se**	**Pt**	**Synthesis Method**	**Supported on Carbon?**	**Acid Treatment?**	**Heat Treatment?**
RuSePt High	0.04	0.02	0.04	2.3.1.8	-	-	-
RuSePt Low	0.04	0.002	0.04	3.3.1.1	-	-	-
PtRu	0.04	-	0.04	2.3.1.9	-	-	-
Pt	-	-	0.04	2.3.1.9	-	-	-
RuSePt High/C	0.04	0.02	0.04	2.3.1.8	Yes	-	-
RuSePt Low/C	0.04	0.002	0.04	3.3.1.1	Yes	-	-
PtRu/C	0.04	-	0.04	2.3.1.9	Yes	-	-
Pt/C	-	-	0.04	2.3.1.9	Yes	-	-
RuSePt High/C Acid	0.04	0.02	0.04	2.3.1.8	Yes	Yes	-
RuSePt Low/C Acid	0.04	0.002	0.04	3.3.1.1	Yes	Yes	-
RuSePt High/C 250 ° C	0.04	0.02	0.04	2.3.1.8	Yes	-	250 ° C
RuSePt High/C 500 ° C	0.04	0.02	0.04	2.3.1.8	Yes	-	500 ° C
RuSePt Low/C 250 ° C	0.04	0.002	0.04	3.3.1.1	Yes	-	250 ° C
RuSePt Low/C 500 ° C	0.04	0.002	0.04	3.3.1.1	Yes	-	500 ° C
PtRu/C 250 ° C	0.04	-	0.04	2.3.1.9	Yes	-	250 ° C
PtRu/C 500 ° C	0.04	-	0.04	2.3.1.9	Yes	-	500 ° C
Pt/C 250 ° C	-	-	0.04	2.3.1.9	Yes	-	250 ° C
Pt/C 500 ° C	-	-	0.04	2.3.1.9	Yes	-	500 ° C

3.4.1 RuSePt Particle Synthesis – Varying Se Concentration

As noted in the previous chapter, initial RuSePt preparations formed nanoparticles with greater concentrations of Se than had been anticipated. These observations were made using XPS, which, as highlighted previously, is a surface sensitive technique. With high concentrations of Se detected via XPS (Table 3), and the observation that oxidised Se species were detected (Figure 14), it was considered likely that a surface layer of Se had formed on the nanoparticles. Given the stated aim for this work of developing Pt-shell nanocatalysts, experiments were devised to seek to mediate the nanoparticle surfaces to prevent the formation of an outer Se coating.

An initial approach in this regard concerned modifying the Se precursor concentration used in the nanoparticle synthesis procedure developed. 'RuSePt Low' nanoparticles were thus prepared according to synthesis protocol 3.3.1.1, with 0.002 Se precursor molarity (a ten fold reduction with respect to the initially prepared 'RuSePt High' particles, with 0.02 M Se in the precursor solution). TEM images of the prepared particles are shown in Figure 18. Their average size was 3.1 ± 0.4 nm and they were spherical in morphology, with very clear dispersion of the particles and almost no agglomeration observed. Relative to the previously prepared nanoparticle systems, and in particular the RuSePt High sample, this represented a significant improvement. Comparing these particles with those pictured in Figure 16, the improvement in dispersion is evident by the clear spaces between the particles, which are smaller (and with lower error) than the RuSePt High particles (3.1 ± 0.4 nm vs 4.4 ± 0.5 nm for the RuSePt Low (Figure

18) and RuSePt High (Figure 16 a,b) samples, respectively). As mentioned previously, nanoparticle size and dispersion are important parameters in catalysis, given their influence on catalyst surface area (and therefore active site availability). Smaller, well dispersed particles have higher available surface areas than those which are agglomerated.

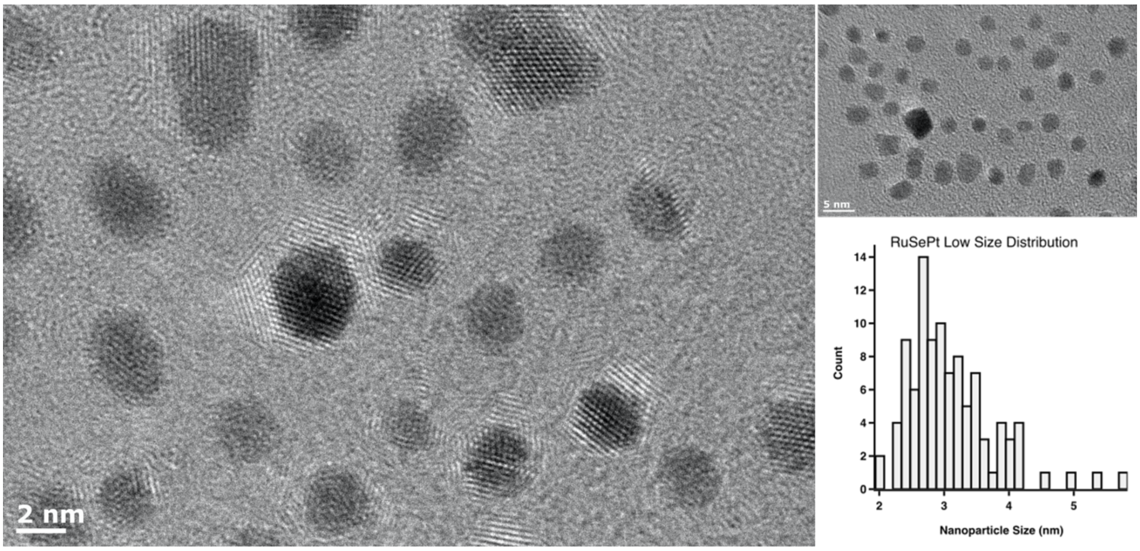

Figure 18. TEM images of as prepared RuSePt Low nanoparticles, with size histogram.

Chemical information regarding the composition of the nanoparticles was sought, to verify the wider impact and efficacy of the novel synthesis procedure. Insights from survey spectra on these and the previously prepared particles are summarised in Table 5. The most surprising feature is the high measured concentrations of Se in the PtRu and Pt samples, which may have arisen through contamination either during sample preparation in the laboratory, during sample transport, or in the course of testing within the XPS instrument vacuum. The low ratio of Ru detected across the samples partly reflects the difficulties associated with using XPS to characterise Ru materials, as described in the preceding chapter, and as highlighted in previously published work in this area [117].

Focussing specifically on the RuSePt Low sample, there was an obvious reduction in the Se content observed following the adoption of a synthetic protocol in which a molarity ten times lower in Se was used, relative to the RuSePt High sample. The concentrations measured for the two constituent metals was lower than anticipated, however. This is likely explained by the surfactant load on these particles. The dispersion pattern shown in Figure 18 suggests a high degree of coordination of oleylamine to the surface of these particles, preventing their agglomeration. While this high surfactant load is useful in stabilising the particles, it also makes their characterisation more challenging. Prior research has elaborated on the impact of surfactant layer thickness on the utility of XPS in characterising nanoparticles [142], highlighting the challenges associated with measuring spectra for nanoparticles with high surfactant loads (and associated thick surfactant layers). Those thick layers are known to obscure signals arising from the nanoparticles, given the interaction of the impinging X-rays on the surfactant molecules themselves.

Table 5. Summary of atomic percentage values calculated from XPS survey spectrum on as prepared RuSePt High, RuSePt Low, PtRu and Pt nanoparticle samples. Each value is an average, calculated from data collected in three measurements per specimen, with two specimens prepared per sample.

	Atomic % of each Element						
Sample	**C 1s**	**O 1s**	**N 1s**	**Si 2p**	**Pt 4f**	**Ru 3p**	**Se 3d**
RuSePt High	62.21 ± 1.78	11.50 ± 0.98	1.05 ± 0.09	22.10 ± 0.99	1.10 ± 0.10	1.46 ± 0.05	0.61 ± 0.06
RuSePt Low	72.42 ± 0.74	12.59 ± 0.27	0.92 ± 0.04	13.89 ± 0.55	0.18 ± 0.01	0.00 ± 0.00	0.02 ± 0.02
PtRu	70.72 ± 2.55	8.35 ± 0.51	1.91 ± 0.12	12.74 ± 1.93	4.84 ± 0.01	0.63 ± 0.17	0.84 ± 0.05
Pt	34.24 ± 0.14	16.18 ± 0.36	1.66 ± 0.12	37.70 ± 0.45	8.53 ± 0.66	0.04 ± 0.04	1.67 ± 0.13

Comparing the high resolution Pt 4f scans collated in Figure 19 highlights differences between the samples, and the unique characteristics of the RuSePt Low material. Broad components in XPS spectra suggest the presence of higher oxidation state species, as a result of the broader range of energy states of the electrons in the band. The wide, low intensity ‘Pt Ox,’ peaks in the RuSePt High spectrum, a, around 72.5 and 76 eV, suggest that the oxidised Pt species in this sample were in higher oxidation states, potentially indicating a high concentration of $PtSe_2$. In the ‘Low’ case, however, the sharper ‘Pt Ox’ peaks in spectrum b, at ~72 and ~75 eV, likely reflect lower oxidation state Pt-O bond formation in the absence of high Se content. The slightly lower binding energy of these components corroborates this supposition, as lower binding energy peaks are associated with lower oxidation states. This hypothesis was also reflected in the relatively sharp peaks in the PtRu and Pt spectra, c) and d) respectively. Further analysis indicates that relative to the other two samples, the Pt Ox peaks (~72 and 75 eV) take a greater share of the peak intensity in the spectra collected for these two samples than is seen in a and b. The Pt 0 peaks (~71 and 74 eV) for both are shallower. This indicates that a higher proportion of the Pt content in those samples was also in oxidised forms, albeit in low oxidation state species such as Pt-O.

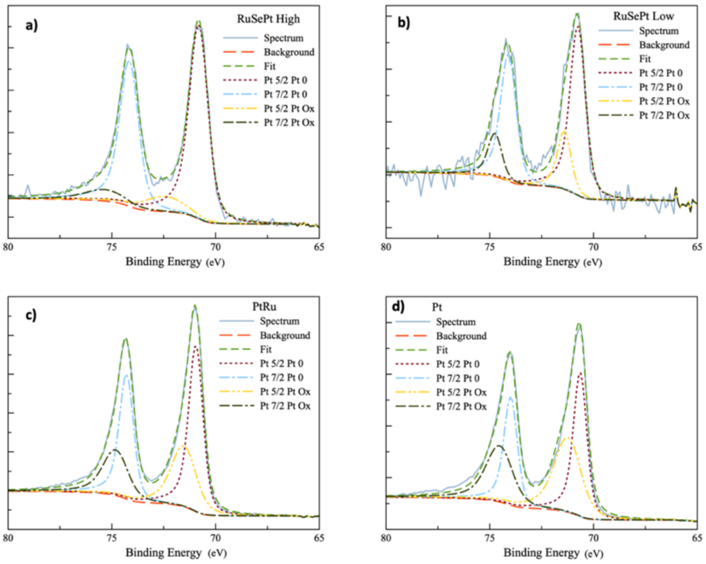

Figure 19. High resolution XPS scans recorded in the Pt 4f region for a) RuSePt High, b) RuSePt Low, c) PtRu and d) Pt nanoparticles. Where ‘Pt 0,’ refers to the components corresponding to metallic Pt, and ‘Pt Ox,’ refers to components corresponding to oxidised platinic species. ‘Spectrum,’ refers to the as-measured spectrum, and ‘Fit,’ refers to the line resulting from the fitting of the Pt spectrum components.

This observation is best elaborated with reference to the TEM images which follow, in Figure 20. The Pt particles, and to a lesser degree the PtRu particles, images d and c, respectively, were more agglomerated than the RuSePt Low particles; this suggests a lower degree of oleylamine adsorption onto the nanoparticle surfaces (as high surfactant adsorption would have lead to good dispersion of the particles, as was the case for the RuSePt Low particles, image b). In the absence of high surfactant adsorption, and indeed without the formation of an Se layer as is likely the case of the RuSePt High particles, then there is ample opportunity for a Pt-O layer to form on the PtRu and Pt nanoparticles when they are exposed to air.

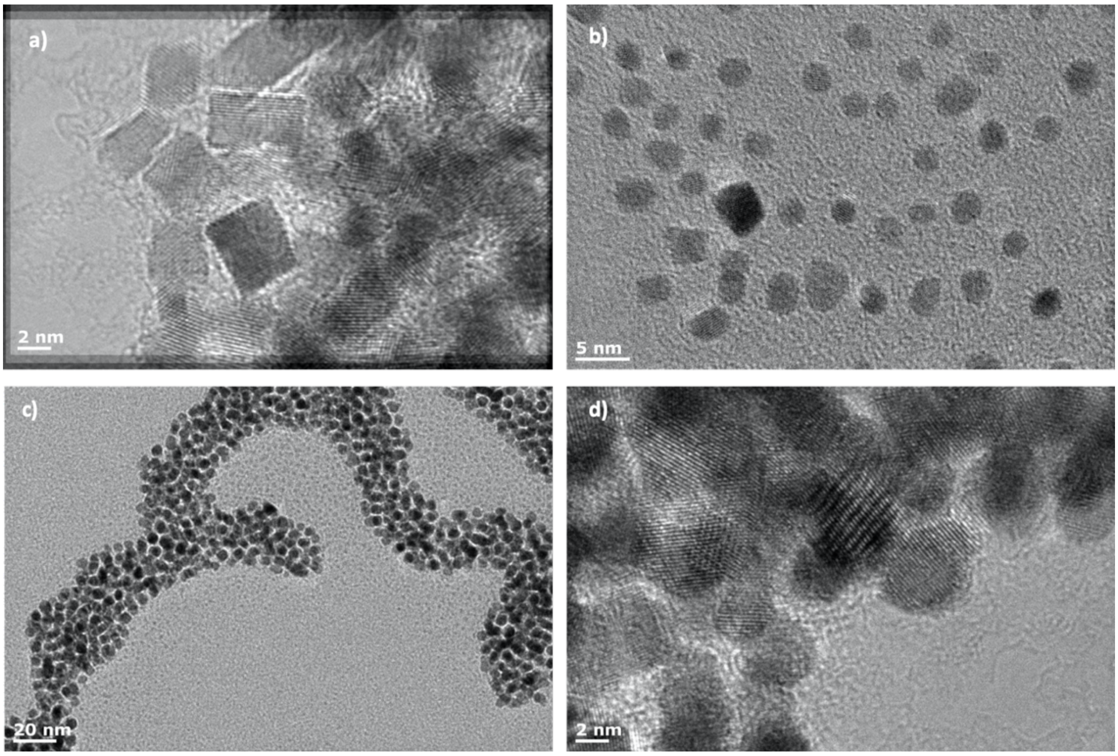

Figure 20. TEM images of a) RuSePt High, b) RuSePt Low, c) PtRu, and d) Pt nanoparticles.

Another interesting comparison to make between the four samples is in regards to the morphology adopted by the nanoparticles in each. These are compared side by side in Figure 20. The RuSePt Low, PtRu and Pt nanoparticles each adopted a broadly spherical morphology. Meanwhile, the RuSePt High particles prepared via this method were observed to generally form cuboidal nanostructures. Significant research effort has been devoted to scrutinising the drivers underpinning shape control in nanoparticle systems. Indeed, as has already been noted, differing surfactants and/or capping agents have been reported to preferentially adsorb onto specific nanoparticle facets, directing the growth of those particles [94] in favour of given facets.

Of significant relevance to the current work is a substantial body of research focussed on the role of oleylamine in directing (Pt) nanoparticle shape during growth [123, 143–146]. One report concerned the capacity to prepare predictably shaped Pt nanoparticles from a wide range of possible morphologies using oleylamine as surfactant, with relatively minor changes in precursor or reaction conditions [143]. For example, the researchers described the formation of nanostructures with higher branching in response to raising the reaction temperature, as higher temperatures favoured faster growth [143]. Further research demonstrated the preferred formation of Pt nanocubes in instances of low precursor concentration due to the associated slow growth favouring the termination of the crystal with (100) faces [144]. In the context of this work, however, the most insightful observation was that of the role played by carbon monoxide (CO) molecules liberated from acetylacetonate (acac) ligands during solvothermal nanoparticle syntheses involving $Pt[acac]_2$. The CO molecules released upon dissociation of acac precursors during thermal reduction were noted to preferentially adsorb onto Pt (111) faces, encouraging growth of Pt nanoparticles with cuboidal morphologies [94, 123]. With these observations in mind, referring back to the morphologies observed for the nanoparticles prepared in this work, as shown in Figure 20, a number of possibilities emerge. The RuSePt High nanoparticles are the only ones under study which adopted a truly cuboidal morphology, though the emergence of some cube-like facets can be observed in the images of the other systems. In the context of these reports, it is likely that CO molecules liberated from the acetylacetonate precursor encouraged the growth of those cube morphologies during synthesis. It is curious though, given that the same precursor and reaction conditions were used for all syntheses, that the same effect is not observed across all of the systems studied. The concentration of Se in the precursor solutions is the only material variable modified between all of the samples concerned, so it seems likely that this variable is the driving force behind the shape direction observed. One explanation could be that the coordination of Se to the growing Pt surfaces in the RuSePt High case competed with the adsorption of oleylamine surfactant molecules in a manner not seen in the other systems, and that the oleylamine layer prevented substantial CO adsorption onto those same surfaces. Interrogating this conclusion further would require mechanistic study. A simpler explanation refers to the composition of the compounds formed; in the RuSePt High case, as already referenced in discussing the XPS analysis, it is likely that $PtSe_2$ formed in the product. $PtSe_2$ is known to adopt a cubic morphology, as seen in RuSePt High, Figure 20, a. Given the relative clarity of the lattice fring structures in the

TEM images discussed in this section, Figure 18 and Figure 20, further analysis was carried out to evaluate the d-spacing evident in the images. The RuSePt High sample, Figure 20, a, has interlayer distances of 5.05 Å, relative to measured distances of 4.20 Å and 4.01 Å for the RuSePt Low and Pt nanoparticle systems, Figure 18, and Figure 20, d, respectively. The 5.05 Å figure measured for the RuSePt High particles aligns closely to the reported theoretical value (5.08 Å) for $PtSe_2$ [147]. Thus, analysis of both interlayer distances and morphology in the RuSePt High nanoparticle system would seem to suggest that $PtSe_2$ has formed in the sample. Further experimental analysis using XRD would be required to verify these conclusions.

A further variety of morphological control exerted upon nanoparticle systems relates to diffusion-mediated segregation of components within nanoalloys. Researchers have reported taking advantage of thermodynamic effects to reliably prepare Pt-Ni nanostructures with catalytically-optimal morphologies and configurations [148]. Niu *et al* adopted this approach in their report of Pt-Ni nanoframe catalysts [79], from which the synthetic method thus far described (method 3.3.1.1) was adapted. In the Niu protocol, star-shaped, dodecahedral nanostructures are described, with Pt-rich facets emerging at surface sites over the course of the synthesis reaction through phase migration. The authors note that the degree of segregation of the two elemental phases – Pt and Ni – within the nanostructures, and the morphology adopted, can be predicted by comparing either the surface energy of the constituent elements, the differences in their atomic radii, or a combination of the two factors. There is a thermodynamic driver for atoms of the element with the lowest surface energy to segregate to the surface, however if there is a disparity in atomic radii then likewise atoms of the element with the largest radii will segregate to the surface to mitigate strain. In the reported case, the (110) facets of the Ni atoms have a lower surface energy of 2.368 J m^{-2}, relative to 2.819 J m^{-2} for the Pt atoms. However, the Pt atoms are much larger than the Ni atoms, with atomic radii of 1.39 Å and 1.24 Å, respectively. The Pt atoms are expected to segregate towards the surface, as was observed [79]. The authors then also reported an acid treatment protocol which was used to leach Ni atoms from the nanoframes, to increase the concentration of Pt in the clusters, and enhance the porosity of the structures, for enhanced catalytic activity [79].

In the present case, the surface energies are 2.819 J m^{-2} and 4.236 J m^{-2} for the Pt (110) Ru (1010) facets, respectively [149]. The atomic radii are 1.39 Å and 1.33 Å for Pt and Ru, respectively [150]. Both features would indicate a thermodynamic drive for Pt atoms to segregate to the surface of the nanoparticles prepared. With this in mind, a focus for this work was on establishing the degree to which the thermodynamic domain had elicited control over the nanoparticles prepared. STEM-EELS experiments were thus carried out on as prepared RuSePt High and RuSePt Low nanoparticles, as described in method 3.3.2.4. The images and EELS maps acquired in these experiments are collated in Figure 21. At first glance it is evident that the configuration of the RuSePt High nanoparticles (maps a-j) is very different to that of the RuSePt Low nanoparticles (maps k-t). In the former case, rather than being incorporated into the nanoparticles, the Ru and Se atoms appear (d,e and i,j) to have decorated the Pt surfaces to varying degrees. There is substantial correlation between the Ru and

Se signals, suggesting that RuSe molecules may have formed during the synthesis reaction. Distinct, kinetically-driven formation of RuSe molecules could have precluded the formation of RuSe@Pt-like alloys predicted thermodynamically, as expected from the comparison of surface energy and atomic radii. A different scenario is observed for the RuSePt Low nanoparticles, however. Turning to the maps n and o, as well as s and t, the Pt and Ru components seemed much more clearly correlated, indicating the formation of nanoparticles either alloyed or at least of mixed composition. In this case the Se appears to have sporadically adsorbed onto the surface of those particles. Given the stated aim of this work to develop a protocol towards the preparation of core-shell RuSe@Pt nanoparticles, it is worth stating explicitly that one of the key insights derived from Figure 21 was that neither system adopted a core-shell morphology.

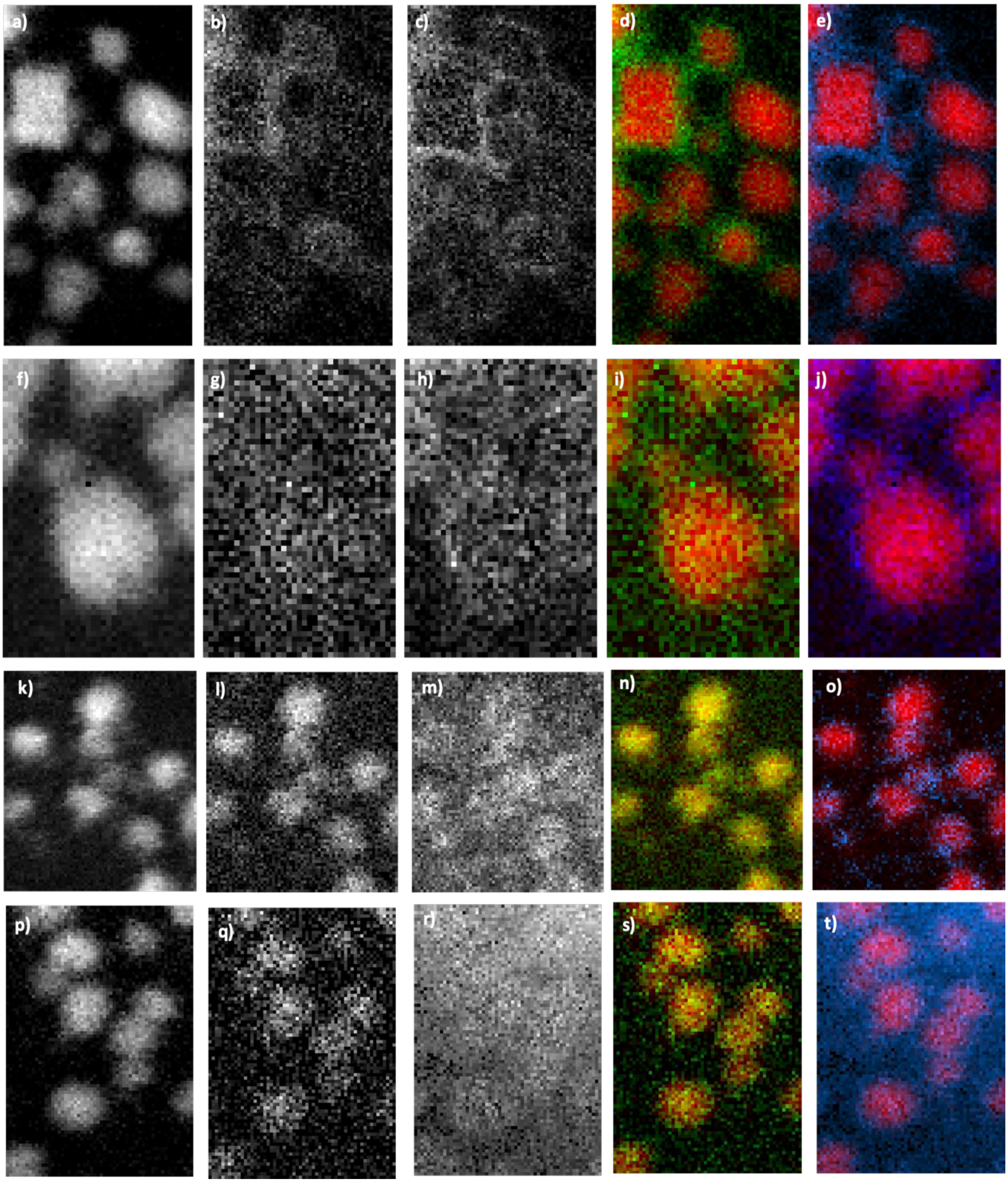

Figure 21. STEM-EELS maps of Pt, Ru and Se signals from RuSePt High and RuSePt Low nanoparticle samples. Where a-j are RuSePt High maps, and k-t are RuSePt Low maps. Maps a), b), and c) show Pt, Ru and Se density, respectively, as do f), g) and h), k) l) and m), and p), q) and r), respectively.. Maps d) and e) show composite Pt-Ru and Pt-Se maps, respectively, and again, so do i) and j), n) and o), and s) and t). In the composites, Pt is coloured red, Ru is coloured green, and Se is coloured blue.

3.4.2 Supporting the Nanoparticles on Carbon

For the purposes of subsequent catalytic testing, and to improve the ease of their handling in the meantime for the steps which follow, the nanoparticle samples under study were deposited on carbon black (TKK), as described in protocol 3.3.1.3. Briefly, TEM images of the carbon supported catalysts were recorded for reference and these are shown in Figure 22. Average sizes of 4.5 ± 0.4 and 4.4 ± 1.1 nm recorded for the RuSePt High/C and RuSePt Low/C nanoparticles, shown in image a and b, respectively. Limited agglomeration is observed in both systems though the broadly cubic and spherical morphologies of the two particles is maintained. The histogram shows the size of the RuSePt Low particles tending lower than the average, but with some larger, agglomerated particles observed.

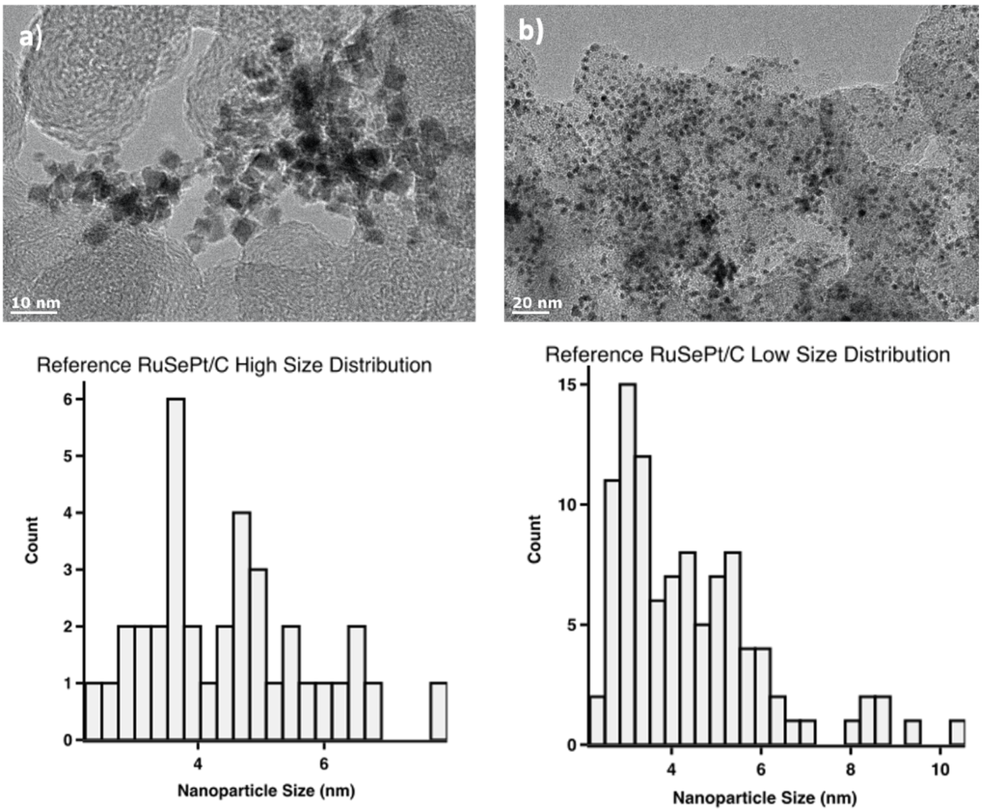

Figure 22. TEM images and histograms of recorded sizes for a) RuSePt High/C and b) RuSePt Low/C nanoparticles.

3.4.3 Acid Treatment

Initial acid treatment experiments were carried out on as prepared, non-carbon supported RuSePt High nanoparticles, with a view to removing surface-bound Se. Acid treatment was carried out according to procedure 3.3.1.2. The impact of the treatment was ascertained using XPS and inherent electrochemistry measurements. Table 6 collates the insight gained from XPS survey scans on the as prepared and acid treated samples.

Table 6. Summary of atomic percentage values calculated from XPS survey spectrum on as prepared and acid treated RuSePt High nanoparticles. Each value is an average, calculated from data collected in three measurements per specimen, with two specimens prepared per sample.

	Atomic % of each Element						
Sample	**C 1s**	**O 1s**	**N 1s**	**Si 2p**	**Pt 4f**	**Ru 3p**	**Se 3d**
RuSePt High	50.81 ± 2.31	17.59 ± 1.31	2.20 ± 0.31	22.55 ± 2.41	1.26 ± 0.21	0.68 ± 0.13	4.90 ± 0.80
RuSePt High Acid	52.82 ± 3.67	21.29 ± 1.10	1.94 ± 0.30	21.44 ± 2.51	0.98 ± 0.19	0.48 ± 0.09	1.05 ± 0.21

A significant reduction in Se content was observed, from 4.90 atomic % to 1.05 atomic %. The percentages measured for Pt and Ru concentration also reduced, though this is likely also associated with the increase observed in carbon and oxygen concentration, which could relate to measurement observing adsorbed acid molecules on the surface of the sample. The reduction in nitrogen concentration is likely associated with corrosive removal of some oleylamine surfactant from the particles.

Relatively straightforward interpretation of the inherent electrochemistry measurements conducted suggests that the acid treatment delivered a more Pt-like catalyst surface. The results of these experiments are summarised in Figure 23. The inherent electrochemical character of the surface as measured for the acid treated sample conforms much more closely to that of the Pt electrode surface, as noted in the shape of the peak at −1 V (vs Ag/AgCl).

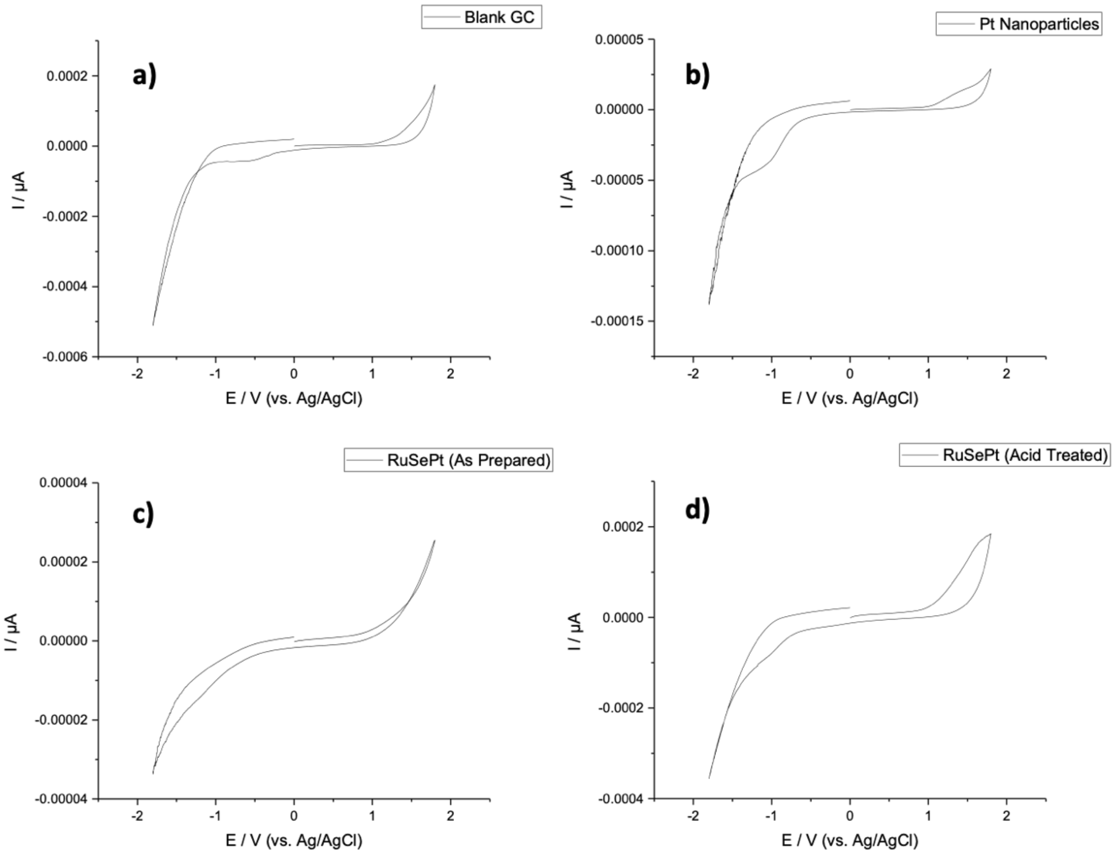

Figure 23. Inherent electrochemical measurements conducted in buffer solution using a) a blank glassy carbon electrode, b) as prepared Pt nanoparticles, c) as prepared RuSePt High nanoparticles and d) acid treated RuSePt High nanoparticles.

As a result of these findings, the acid treatment protocol was applied further to carbon-supported catalyst powders prepared with RuSePt High and RuSePt Low nanoparticle suspensions. Treated samples were studied using TEM and XPS, prior to full catalytic testing as described in the proceeding chapter. TEM images of the treated catalyst powders are shown in Figure 24. As shown, some agglomeration of the particles is observed, with average particle sizes of 4.2 ± 0.5 and 3.7 ± 0.7 nm determined for the acid treated RuSePt High/C and RuSePt Low/C nanoparticles, respectively. A slight loss of morphology is also noted in the RuSePt High case, a.

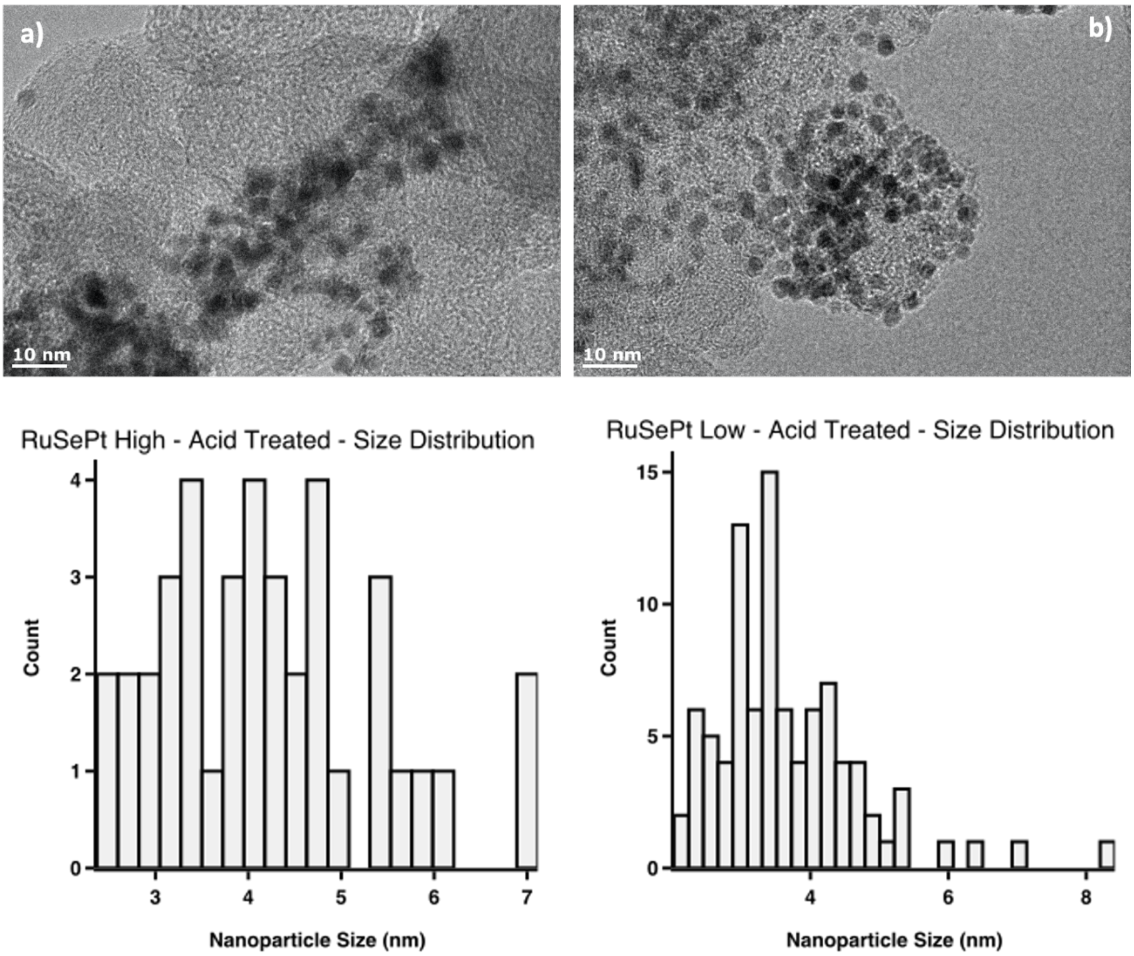

Figure 24. TEM images and accompanying histograms showing measured nanoparticle sizes for acid treated samples of a) RuSePt High and b) RuSePt Low nanoparticles.

Insight from XPS survey measurements on these samples is summarised in Table 7. In this case Se content appears to increase for both samples, alongside a concomitant reduction in Ru content. These results are likely explained by the variance in the atomic percentages of the other component elements, however. In all four cases the Si content can be taken to be an indication of film quality, where high Si content is associated with the emission of electrons from the Si wafer upon which the samples have been deposited. In samples with high quality films, low Si concentrations would be measured due to limited emission from the substrate surface, relative to the deposited sample layer. As the support wafers are composed of silicon dioxide, the same observation is true of the variability of oxygen concentrations between the samples. However the increase in carbon concentration in the RuSePt high case can provide some insight into the impact of the treatment, and is likely explained by the removal by the corrosive acid of oxygen-rich groups from the surface of the carbon support material upon which the nanoparticles are deposited. Meanwhile, the opposite observation for the RuSePt Low samples suggests that surfactant molecules have been removed from the nanoparticle surface in the acid treated case. The verity of this observation is supported by the decrease in measured nitrogen concentration, alongside an increase in platinum concentration in the treated sample. Having said that, it is difficult to draw substantial conclusions from the variations in metal concentrations, given that the non-metal components make up a much bigger contribution to the spectrum for the overall sample.

Table 7. Summary of atomic percentage values calculated from XPS survey spectrum on as prepared and acid treated RuSePt High/C and RuSePt Low/C nanoparticles. Each value is an average, calculated from data collected in three measurements per specimen, with two specimens prepared per sample.

	Atomic % of each Element						
Sample	**C 1s**	**O 1s**	**N 1s**	**Si 2p**	**Pt 4f**	**Ru 3p**	**Se 3d**
RuSePt High/C	64.23 ± 7.58	12.07 ± 2.13	0.51 ± 0.21	22.79 ± 5.27	0.18 ± 0.02	0.14 ± 0.01	0.02 ± 0.02
RuSePt High/C Acid	90.63 ± 2.88	3.50 ± 0.88	0.92 ± 0.03	4.75 ± 2.09	0.15 ± 0.02	0.02 ± 0.02	0.05 ± 0.03
RuSePt Low/C	86.04 ± 4.86	4.25 ± 1.24	1.81 ± 0.10	7.98 ± 3.03	0.16 ± 0.02	0.16 ± 0.11	0.02 ± 0.01
RuSePt Low/C Acid	68.17 ± 1.50	12.45 ± 0.05	0.98 ± 0.13	17.91 ± 1.51	0.27 ± 0.05	0.14 ± 0.14	0.10 ± 0.01

Further interrogation of the impact of the acid treatment was pursued through evaluation of the high resolution spectra recorded in the Pt 4f region, for each of the samples. Given the challenges associated with interpreting the survey spectra in the context of relatively low metal loadings, the high resolution Pt spectra were a valuable resource in better understanding the phenomena affecting the metal component of the material. The spectra collected are collated in Figure 25. Evident in those spectra is the shift in the degree to which the Pt is present in higher oxidation states after acid treatment. In the as prepared case for the RuSePt High, a in Figure 25, the 'Pt Ox,' components, at ~74 and ~77 eV, are very broad, but notably make up a low overall contribution to the fit. In XPS, broader peaks, particularly those stretching to higher binding energies, suggest higher degrees of oxidation. This suggests a low percentage contribution of higher oxidation state Pt species, likely Pt IV, which could indicate the presence of $PtSe_2$ character in the sample. In the acid treated case, b in Figure 25, the 'Pt Ox' peaks, at slightly lower binding energies of ~73 and ~76 eV, are sharper and make a larger contribution to the wider fit, as the components are much bigger. This indicates a greater overall concentration of oxidised Pt species, made by atoms in lower oxidation states than those in the as prepared case. The doublet is less broad overall, with the spectrum returning to a background level at a lower binding energy, around 77 rather than 80 eV. This is also interpreted to suggest a lower contribution from higher oxidation state Pt species, suggesting Se has indeed been removed, likely replaced by the formation of a Pt-O layer at the surface of the nanoparticles. As before, opposite observations are made for the RuSePt Low spectra, c and d in Figure 25. The corrosive removal of surfactant molecules from the nanoparticle surface would expose it to greater oxidation, which could explain the broadening seen in the ‘Pt Ox’ peaks in the spectrum for the acid treated sample, d, at ~72 and 76 eV.

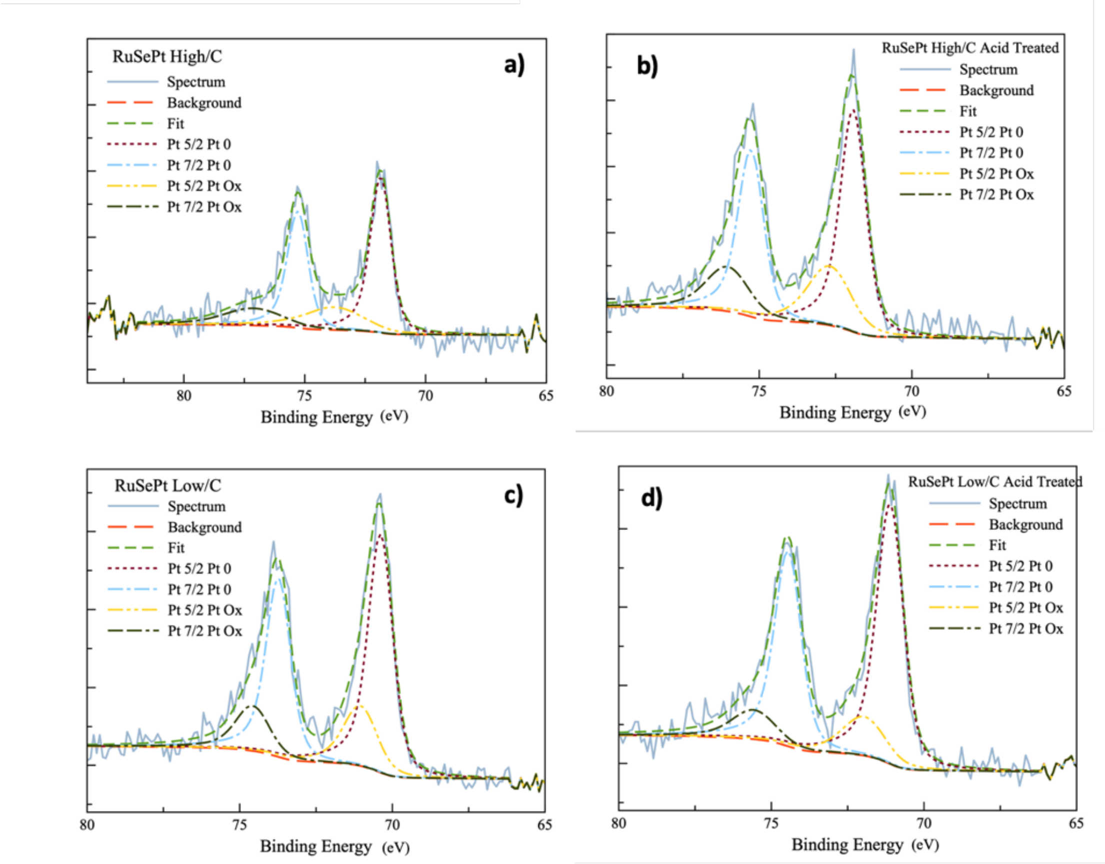

Figure 25. High resolution XPS scans in the Pt 4f region for a) as prepared RuSePt High/C nanoparticles, b) acid treated RuSePt High/C nanoparticles, c) as prepared RuSePt Low/C nanoparticles, and d) acid treated RuSePt Low/C nanoparticles.

The phenomena described are further interrogated in the proceeding chapter, in which the acid treated catalyst powders are tested electrochemically.

3.4.4 Heat Treatment

Samples of RuSePt High/C, RuSePt Low/C, PtRu/C and Pt/C were heat treated according to protocol 3.3.1.4 in two distinct temperature ranges, at 250 and 500 °C. Heat treatment was intended to modify the surface composition of the particles by affecting the chemical ordering of the nanoparticle components, and encouraging the adoption of the segregated composition indicated by the surface energy of those components, as noted earlier in this chapter. It was also anticipated that heat treatment would encourage removal of surfactant molecules from the carbon-supported nanoparticles. Prior work has suggested that this would enhance their eventual catalytic activity [127, 131].

The treated powders were characterised using TEM and XPS. Results from XPS survey scans carried out on all powders are summarised in Table 8. These results show a consistent and substantial decrease in carbon and nitrogen content, likely due to the removal of oleylamine molecules from the nanoparticle surfaces. A consistent reduction is Se concentration is also observed across the samples. The concomitant increase in oxygen concentrations observed may relate to the oxidation of newly exposed metal and carbon surfaces in the materials during or after the heat treatment, despite the use of a reducing gas flow, though this may be more of an indication of lower film quality as in previous cases. As with previous measurements, Si content can be interpreted as a proxy for film quality. As noted prior, the higher the Si content measured in the spectrum, the larger the extent to which the X-rays have impinged upon the substrate, rather than the material under study. Seemingly erroneous atomic percentages, particularly among the metallic components, may be explained by issues with sample preparation as these samples were generally less soluble than their untreated counterparts, or poor quality deposition on the Si wafer substrates. A general comment worth making regarding these results refers to the detection limits of XPS. A comprehensive overview of XPS detection limits was published in 2014 by Shard [151]. This work suggests a typical detection limit in the range 0.1-1 atomic %, varying depending upon which trace element is being studied, and within which matrix. With this noted, and acknowledging the uncertainty associated with standard deviations in the data recorded, there is limited statistical significance in the Pt, Ru and Se atomic % values recorded. The all-important impact of the heat treatment protocols on the metallic components and indeed nanoparticle surfaces is best explored by evaluating in detail the variations between the high resolution Pt 4f spectra recorded for each sample, which follow.

Table 8. Summary of atomic percentage values calculated from XPS survey spectrum on as prepared and heat treated RuSePt High/C, RuSePt Low/C, PtRu/C, and Pt/C nanoparticles. Each value is an average, calculated from data collected in three measurements per specimen, with two specimens prepared per sample.

	Atomic % of each Element						
Sample	**C 1s**	**O 1s**	**N 1s**	**Si 2p**	**Pt 4f**	**Ru 3p**	**Se 3d**
RuSePt High/C	78.20 ± 0.31	6.80 ± 0.34	0.63 ± 0.07	13.97 ± 0.20	0.20 ± 0.01	0.10 ± 0.09	0.10 ± 0.02
RuSePt High/C 250 ° C	24.44 ± 2.91	23.01 ± 1.16	0.57 ± 0.09	51.80 ± 1.71	0.03 ± 0.01	0.08 ± 0.03	0.08 ± 0.03
RuSePt High/C 500 ° C	68.63 ± 0.75	9.85 ± 0.27	0 ± 0.12	21.17 ± 0.52	0.17 ± 0.03	0.15 ± 0.00	0.04 ± 0.02
RuSePt Low/C	95.45 ± 0.05	1.13 ± 0.07	1.84 ± 0.14	1.54 ± 0.09	0.03 ± 0.01	0.00 ± 0.00	0.00 ± 0.00
RuSePt Low/C 250 ° C	59.22 ± 1.54	11.08 ± 0.30	1.03 ± 0.10	27.91 ± 0.83	0.54 ± 0.19	0.18 ± 0.05	0.05 ± 0.04
RuSePt Low/C 500 ° C	48.18 ± 2.27	16.02 ± 0.37	0.84 ± 0.08	34.37 ± 1.56	0.09 ± 0.05	0.50 ± 0.06	0.02 ± 0.02
PtRu/C	93.37 ± 1.31	2.78 ± 0.44	0.74 ± 0.14	3.00 ± 0.74	0.10 ± 0.01	0.01 ± 0.00	0.00 ± 0.00
PtRu/C 250 ° C	22.03 ± 4.94	19.79 ± 0.75	0.88 ± 0.09	57.29 ± 1.71	0.00 ± 0.00	0.03 ± 0.03	0.00 ± 0.00
PtRu/C 500 ° C	38.50 ± 1.94	21.68 ± 3.98	0.41 ± 0.14	38.36 ± 8.21	0.24 ± 0.07	0.73 ± 0.03	0.08 ± 0.02
Pt/C	82.93 ± 2.27	5.78 ± 0.75	0.00 ± 0.00	9.74 ± 1.56	1.25 ± 0.02	0.00 ± 0.00	0.29 ± 0.04
Pt/C 250 ° C	37.46 ± 2.01	24.68 ± 0.48	0.17 ± 0.14	37.61 ± 0.83	0.02 ± 0.01	0.00 ± 0.00	0.05 ± 0.01
Pt/C 500 ° C	51.55 ± 1.54	19.16 ± 0.37	0.00 ± 0.00	28.81 ± 1.42	0.38 ± 0.02	0.00 ± 0.00	0.12 ± 0.10

TEM images and high resolution XPS spectra measured within the Pt 4f region are summarised for each set of samples. Key areas of focus for evaluating these concerned ascertaining the degree to which heat treatment modified the morphology and dispersion of the nanoparticles, and analysing the impact of the treatments upon the particle surfaces by evaluating changes in the oxidation state of the Pt species present.

In the RuSePt High/C images, Figure 26, morphological changes were observed for both samples. In the 250 °C case, the average nanoparticle size recorded was 4.3 ± 0.4 nm, relative to the 4.5 ± 0.4 nm average size measured for the as prepared RuSePt High/C sample (Figure 22). This indicates that the individual particles were not agglomerated after treatment at this temperature, as is evident from image a, Figure 26. However, the particles are closer packed, suggesting that sintering and ripening may have begun during the heat treatment. Image b, Figure 26, shows a different outcome for the particles treated at 500 °C, however. Significant agglomeration is evident, with an average size of 9.9 ± 1.9 nm measured for these particles. The loss in catalyst surface area is clear, and the particles did not appear to retain clear morphologies.

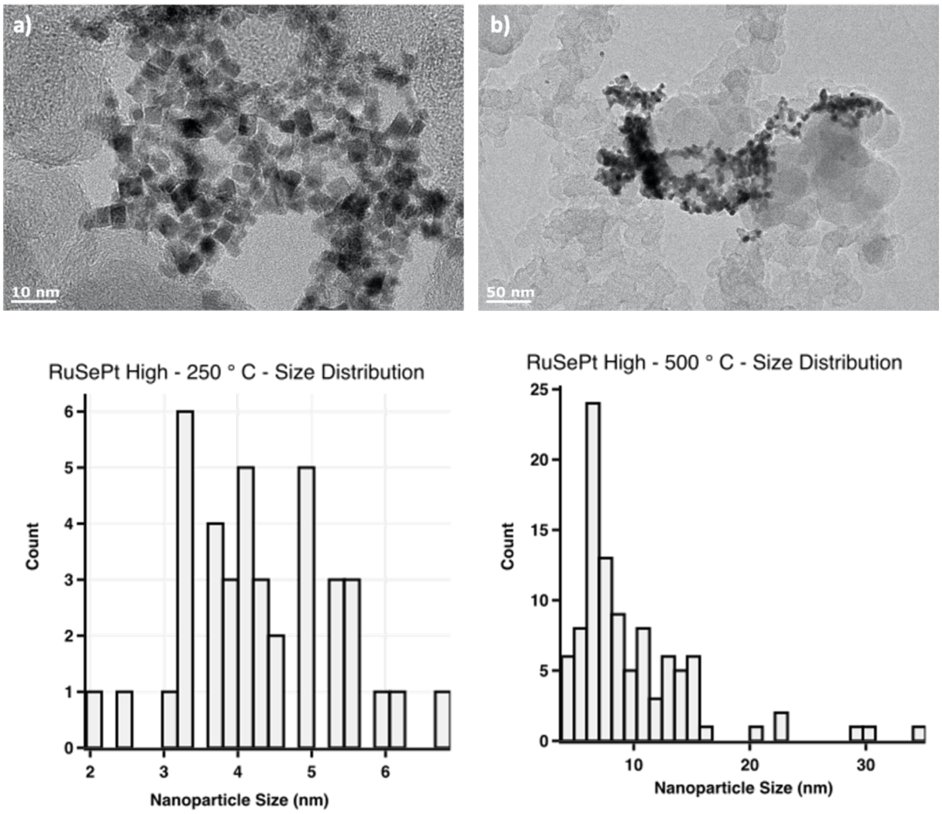

Figure 26. TEM images of heat treated RuSePt High/C nanoparticles, a) treated at 250 °C, and b) treated at 500 °C, with histograms of recorded nanoparticle sizes.

High resolution Pt 4f spectra recorded for the heat treated RuSePt High/C samples, Figure 27, show shifts in the oxidative environment of the Pt in the samples. In spectrum b, that of the sample treated at 250 °C, an increase in concentration of higher oxidation state Pt species is observed, indicated by peak broadening evident in the Pt Ox peaks at ~69 and ~73 eV, which are shallow and wide. The spectrum itself was broadened relative to the others, a and c, with a shoulder evident at ~74 eV. Referring back to the measured elemental concentrations summarised in Table 8, in which there is a significant increase in total oxygen concentration observed for this sample (23.01 atomic %, relative to 6.80 atomic % measured for the untreated sample), it is likely that rather than the surface having been reduced as intended, PtO_2 has formed. The same trend is not reflected in the 500 °C case, however, in which comparatively sharp peak components are retained, though the contribution from the oxidised Pt Ox components, at ~67 and ~72 eV, is higher. Given the boiling point of the oleylamine surfactant used is ~ 350 °C, it is likely that the increase in oxidised character in the 500 °C case relates to post-treatment Pt-O formation on nanoparticle surfaces from which oleylamine has been removed.

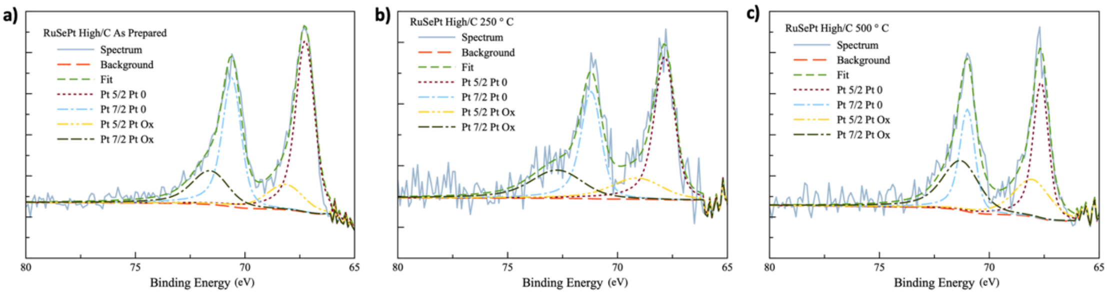

Figure 27. High resolution XPS scans in the Pt 4f region for a) as prepared RuSePt High/C nanoparticles, b) RuSePt High/C nanoparticles treated at 250 °C, and c) RuSePt High/C nanoparticles treated at 500 °C.

Broadly similar trends are observed for the PtRu/C and Pt/C control samples, with nanoparticle agglomeration observed due to a combination of the increase in system energy through heating, and the removal in parallel of stabilising surfactant molecules. The observations made during measurements and imaging on the two materials is discussed in turn.

Heat treatment caused significant agglomeration of the PtRu/C nanoparticles, with average sizes of 11.0 ± 1.4 and 13.6 ± 0.9 nm recorded in the 250 °C and 500 °C cases, respectively. TEM images and histograms for these are shown in Figure 28. High resolution XPS scans of the samples are also collated in Figure 29, though detailed discussion of these is impeded by the poor quality of the spectra collected in the heat treated cases. In the as prepared case, a, the Pt Ox components, at ~67 and ~71 eV, make a much larger contribution than is observed in the other samples, suggesting that in the absence of Se, greater Pt-O formation occurs following heat treatment.

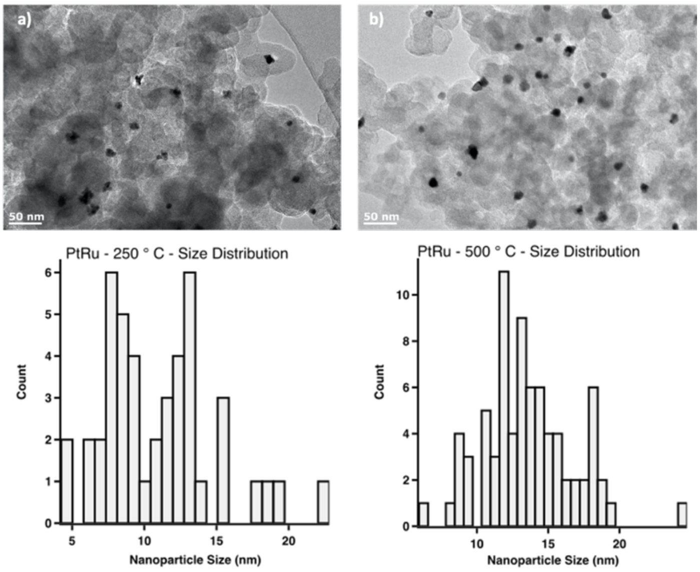

Figure 28. TEM images of PtRu/C nanoparticles heat treated at a) 250 °C, and b) 500 °C, with accompanying histograms showing measured size distribution.

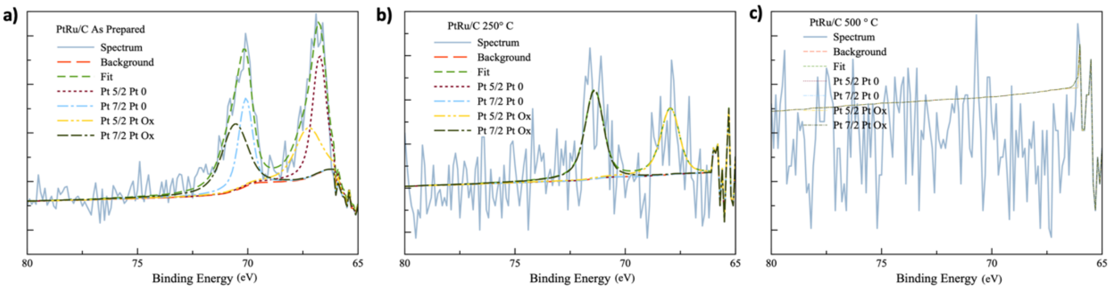

Figure 29. High resolution XPS scans in the Pt 4f region for a) as prepared PtRu/C nanoparticles, b) for PtRu/C nanoparticles treated at 250 °C, and c) for PtRu/C nanoparticles treated at 500 °C.

Average sizes recorded for the heat treated Pt/C nanoparticles were 5.9 ± 1.9 and 13.8 ± 0.7 nm for the samples heat treated at 250 °C and 500 °C, respectively. These were also subject to significant agglomeration during heat treatment. TEM images of the samples, and histograms of measured sizes, are shown in Figure 30.

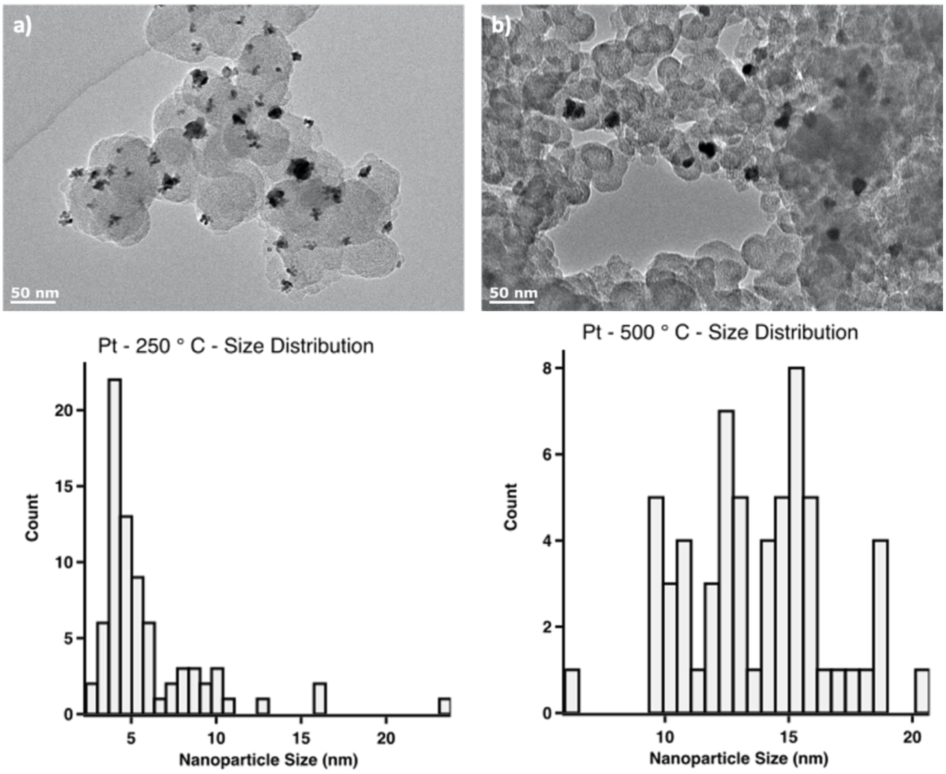

Figure 30. TEM images of Pt/C nanoparticles heat treated at a) 250 °C, and b) 500 °C, with accompanying histograms showing measured size distribution.

Insight from the high resolution Pt 4f scans for the Pt/C samples treated at 250 and 500 °C, shown in Figure 31 is relatively limited. The spectra obtained in the 250 °C case were poor quality. In the 500 °C case, c, a minor increase in the contribution made by Pt Ox components, at ~68 and ~72 eV, was observed, likely indicating the post-treatment formation of a PtO layer on exposed Pt surfaces. As with the as prepared PtRu/C sample, the platinic species in the as prepared Pt/C already appeared to be more oxidised than in the RuSePt cases, as indicated by the relatively large Pt Ox peaks in spectrum a.

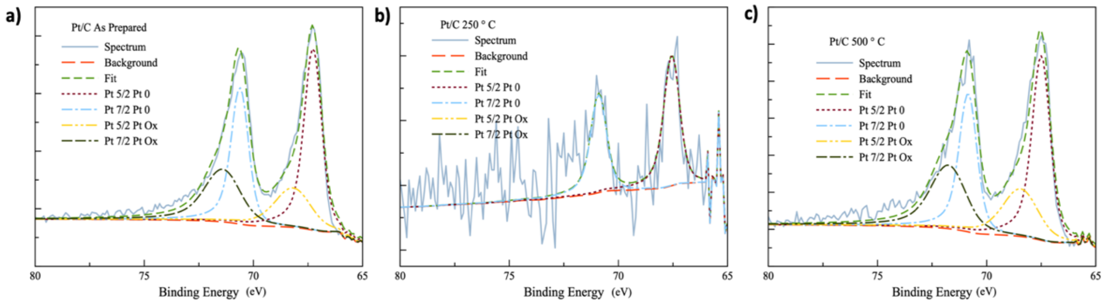

Figure 31. High resolution XPS scans in the Pt 4f region for a) as prepared Pt/C nanoparticles, b) for Pt/C nanoparticles treated at 250 °C, and c) for Pt/C nanoparticles treated at 500 °C.

The RuSePt Low/C nanoparticles were much less prone to agglomeration than the others, however. Average sizes of 4.2 ± 0.6 and 5.9 ± 0.9 nm were recorded for the samples treated at 250 and 500 °C, respectively. This compares to 4.4 ± 1.1 nm as measured for the as prepared RuSePt Low/C nanoparticles (Figure 22), highlighting the very limited growth in size seen, even in the 500 °C case. This sets the RuSePt Low/C material apart completely from the other materials studied, given the significant increases in size noted for the samples addressed prior, noting that the average size recorded for the RuSePt High/C nanoparticles doubled from 4.5 ± 0.4 nm as measured for the as prepared sample, to 9.9 ± 1.9 nm for the sample treated at 500 °C. This observation confirms that the RuSePt Low/C nanoparticles were particularly well stabilised, and likely also well anchored to the carbon support. TEM images and size histograms of the treated RuSePt Low/C nanoparticles are shown in Figure 32, which further highlight the retention of distinct particles with maintained spherical morphology.

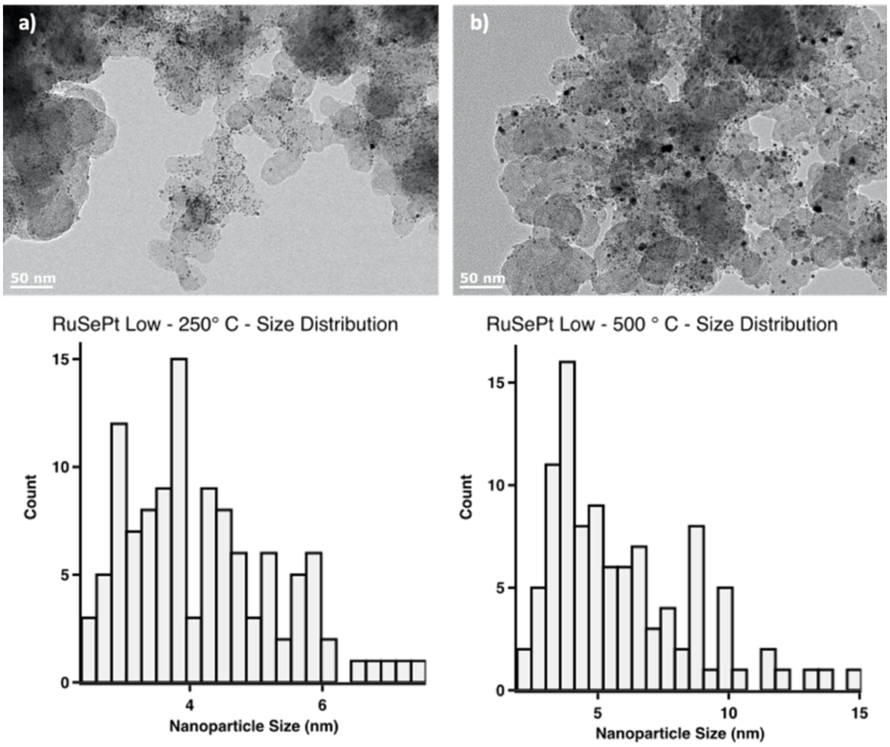

Figure 32. TEM images of heat treated RuSePt Low/C nanoparticles, a) treated at 250 °C, and b) treated at 500 °C, with histograms of recorded nanoparticle sizes.

Meanwhile, high resolution XPS scans in the Pt 4f region, Figure 33, conducted for the heat treated RuSePt Low/C samples, indicate a similarly contrary evolution in chemical characteristics through heat treatment for that system. Some peak broadening was observed in the 250 °C case in the Pt Ox peaks, at ~68 and ~72 eV, as noted for the previous samples, perhaps due to the formation of PtO_2 on newly exposed Pt surfaces. As highlighted in the discussion of the Pt4f spectrum for the RuSePt High/C 250°C sample, b in Figure 27, the whole spectrum was broadened in the RuSePt Low 250 °C spectrum, b in Figure 33. A shoulder is evident in the spectrum at ~74 eV. This feature suggests a broad increase in oxidation of the Pt species present, relative to the other samples. In the 500 °C case, however, given the assumed removal of oleylamine from the system, it is curious that significant oxidation was not observed. As Figure 32 showed, this was the only nanoparticle system studied to retain good dispersion following heat treatment, with distinct, spherical RuSePt Low/C particles retained. It is likely therefore that the observed post-heating increase in oxidation noted for the other samples (spectrum c in Figure 27 and Figure 31) occurred on exposed, agglomerated surfaces, with a Pt-O (or Pt-O and Ru-O) oxide film forming across the mixed catalyst surface.

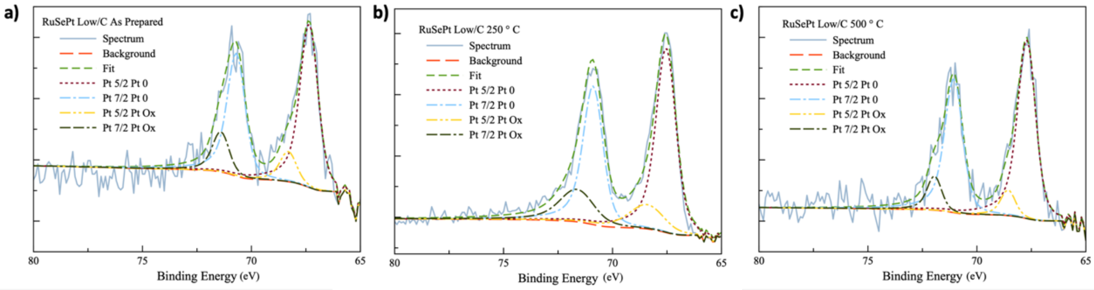

Figure 33. High resolution XPS scans in the Pt 4f region for a) as prepared RuSePt Low/C nanoparticles, b) for RuSeP Lowt/C nanoparticles treated at 250 °C, and c) for RuSePt Low/C nanoparticles treated at 500 °C.

To summarise, then, it is worth noting that almost all of the treated samples, whether acid or heat treated, were subject to agglomeration of the catalyst particles, and a concomitant loss of the morphologies described for the as prepared nanoparticles. The obvious exception to that rule was the RuSePt

Low/C nanoparticles, which were retained in a spherical morphology without significant loss in dispersion following acid or heat treatment (at either 250 °C or 500 °C). The chapter which follows focusses on the electrochemical characterisation and testing, which was used to further elaborate on understanding these trends and the impact of the treatment protocols on the utility of the nanoparticles prepared.

3.5 Conclusions

This chapter concerned efforts to control and modify the surface configuration of the catalyst nanoparticles under development. To that end, a further synthetic procedure was iterated and the particles prepared were subject to acid and heat treatment. TEM, XPS and STEM-EELS experiments were conducted to characterise the product particles, to gain an understanding of the impact of the synthetic and post-synthetic interventions developed.

A further iteration of the RuSePt system, 'RuSePt Low', was prepared with a comparatively low concentration of Se (with Se precursor molarity 10 times lower than RuSePt High), in order to evaluate the effect of varying Se content on particle morphology and configuration. Following full characterisation, the RuSePt Low nanoparticles prepared were found to be smaller and more well dispersed than the other systems under study. These nanoparticles were studied alongside the previously prepared RuSePt High particles in STEM-EELS experiments, aimed at evaluating the configuration of the constituent elements within the nanoparticles. STEM-EELS measurements confirmed that the the two systems differed widely. The RuSePt High nanoparticles formed broadly cuboidal arrays of Pt nanoparticles, coated to varying degrees with adsorbed RuSe molecules. Meanwhile, particles within the RuSePt Low system were found to have adopted spherical morphologies with mixed, potentially alloyed PtRu structures decorated with Se. Neither particle had been prepared in a core-shell morphology as had been intended, however the resulting morphologies provided insight into the dynamics controlling the assembly of the particles. A substantial body of prior work aiming to understand control mechanisms at play in oleylamine-mediated Pt nanoparticle synthesis had ascertained that in syntheses involving acetylacetonate precursors, liberated CO molecules adsorbed preferentially onto Pt 111 surfaces, driving and directing growth of particles with cuboidal morphologies [123, 143–146]. That the RuSePt High particles prepared appeared indeed to preferentially adopt this morphology, while the RuSePt Low particles did not, suggested that the Se content in the particles played a role in mediating this effect. This phenomenon requires further study, however the observation indicates that researchers seeking to direct the growth of Pt-containing nanoparticles towards certain morphologies could consider including ad-atoms in their synthetic protocols, including Se.

The synthetic protocol developed for the preparation of both High and Low RuSePt was intended to deliver a Pt shell, or surface-segregated Pt layer over the Ru(Se) core material. In predicting this outcome, the surface energy and atomic radii of the two elements was consulted. The reality that the product particles failed to adopt the intended or expected morphology could serve as an example to other researchers that the factors at play in determining nanoparticle configuration are indeed complex, and that surfactant effects and the influence of the precursor(s) and their molarity must be considered in designing experiments and protocols. This warrants further study.

In further work aimed at modifying the surface configuration of the nanoparticle catalysts, acid treatment and heat treatment protocols were developed and implemented, and their impact upon the particles was interrogated using physical and chemical characterisation methods. Both protocols were found to encourage agglomeration and loss of morphology of the nanoparticles treated, although this effect was much less pronounced for the RuSePt Low particles. A range of effects were also noted in terms of the configuration and surface chemistry of the particles, largely as a result of the removal of surfactant molecules in the course of the treatment reactions. These effects were primarily observed in terms of shifts in oxidative environment of the Pt atoms in the samples, as measured using high resolution XPS spectra in the Pt 4f region, and indicated that following acid and heat treatment the particle surfaces were generally subject to increased oxidation. It is difficult to determine whether this effect arose as a result of, or was a driving factor in, the loss of morphology and agglomeration described in these instances. This also warrants further study.

The following chapter concerns the electrocatalytic testing of the nanoparticles, through which the understanding of these phenomena was further elaborated.

4 Electrocatalytic Oxygen Reduction at RuSePt Nanoparticle Surfaces

4.1 Background and Context

Nanoparticles and indeed nanoalloys have long been of interest to researchers pursuing novel and enhanced routes to developing catalysts for a wide range of reactions now considered essential to life as we know it. As has already been noted, and as is well known, catalyst particles in the nanoscale possess different reactivities than bulk samples of the same material. Further, the opportunity to finely tune the structure, composition and morphology of the particles prepared, as has been described in the preceding sections, offers the researcher routes to tailor the selectivity of the particles to a specified reaction. These observations are particularly true of nanoalloy particles, which are known to adopt configurations unlike the two (or more) parent metals incorporated, with ensuing influence on their catalytic reactivities, activities and selectivities [152]. In an oxygen reduction reaction (ORR) context, this feature gives rise to the so-called ‘volcano plot’ as referred to in Figure 5 [44], which describes the ORR activities for a series of alloy nanoparticles.

As already noted, the ORR is essential to the function of many fuel cell variants, including the polymer electrolyte fuel cell (PEFC). The mechanisms of this reaction were discussed in an earlier section and are demonstrated graphically in Figure 3. The slow kinetics of this reaction, partly influenced by the mechanisms noted, can impede wider fuel cell utility and result in voltage loss

[153]. As such, the development of novel catalysts with enhanced ORR activities is a key target for researchers. Progress towards preparing novel alloy and core@shell nanoparticle catalyst materials was surveyed in section 1.2.

A key priority for those researchers working in this area is benchmarking the activity of their catalysts against those reported by other scientists. Accurately determining those activities, and comparing the potential for the prepared particles to offer a realistic commercial alternative, is crucial to advancing in this field. As such, electrochemical characterisation methods are integral tools in this endeavour. Electrochemical methods are useful for studying electron transfer processes, and in particular oxidation and reduction reactions. While controlling the driving force behind these reactions in purely chemical contexts can be challenging, in electrochemical experiments these driving forces can be controlled simply. As a result, researchers can gain insight into the kinetic and thermodynamic features of the systems under study [154].

One of the most popular electrochemical methods is cyclic voltammetry (CV). CV experiments are particularly well placed for the study of reduction and oxidation reactions. In CV measurements, either a potential (or voltage) (E) or current (i) is applied to the system using a potentiostatic (or galvanostatic) instrument, and responding evolution in the other variable is measured. All of the experiments described hereafter involve the application of a potential, and the measurement of the current produced as a result of the reaction which ensues. The focus in this section is on the measurement of oxygen reduction during the

ORR, and the redox equilibrium observed in solution in the course of the reaction. That equilibrium is described by the Nernst equation, (Equation 2) which relates an electrochemical cell's potential (E) to the standard potential (E^0) of an analyte, and the activities of its oxidised (Ox) and reduced (Red) species in the solution.

$$E = E^0 + \frac{RT}{nF} \, ln \frac{(Ox)}{(Red)}$$

Equation 2. The Nernst equation, which relates the potential of a cell to the standard potential of an analyte and the activities of its reduced and oxidised species.

Where R is the universal gas constant, T is the temperature, n is the number of electrons and F is Faraday's constant. As the cell potential is scanned during a CV experiment, the activities, or rather the analogous concentrations, of the oxidised or reduced species in solution evolve as predicted by the equation, generating positive or negative currents, respectively, which are measured. In the course of a scan, diffusion limitations dictate that the concentration of reactant in the vicinity of the electrode is depleted [154]. As such, a key consideration in experimental design is managing diffusion control, with a common approach being the use of rotating electrodes [155], as will be discussed in detail.

In terms of instrumentation and experimental setup, an electrochemical cell is typically used as a reaction vessel. These items of glassware are typically optimised with a holed lid or with multiple necks designed to keep the electrodes stable. Three electrodes are typically used; the working electrode, the counter electrode and the reference electrode. A cell is depicted in Figure 34.

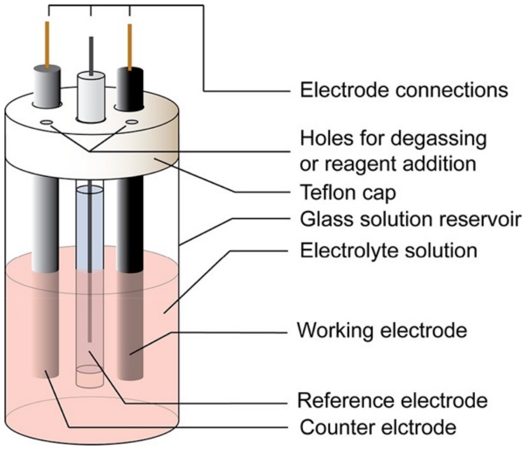

Figure 34. A typical three electrode electrochemical cell. Reproduced from [151] with permission. Copyright © 2017 The American Chemical Society and Division of Chemical Education, Inc.

The working electrode is typically composed of an inert but highly conductive material such as platinum or glassy carbon. The working electrode is the site of the reaction of interest. A potentiostat is used to control the potential applied at the working electrode in order to facilitate the reaction, and the working electrode is also used to measure the current generated [154]. In the case of ORR testing, the catalyst powders prepared are deposited onto the working electrode surface. Glassy carbon is the working electrode of choice for such testing, given the common use of platinum as a catalyst material. Glassy carbon electrodes must first be cleaned and activated through a polishing procedure, in which adsorbed species are removed from the electrode surface, typically using alumina slurry and cloth polishing pads. A reference electrode is used to relate the measured potential to a well-defined and stable standard such as the saturated calomel electrode or the Ag/AgCl electrode, which have been well characterised. The applied potential is reported “vs” the reference electrode, for example “x V vs Ag/AgCl,” in order to denote the reference used. The counter electrode, typically wire, disk or mesh of an inert metal such as platinum, is used to complete the circuit within the cell in order to facilitate the flow of current [154].

A number of ORR electrocatalysis testing protocols have been reported by researchers through the years [156–159]. Noting the elusive nature of practical details on how best to carry out these measurements, Garsany and colleagues published a robust and detailed guide in 2010 [157], which has since become a reference text for many researchers working in this area. The first step in the procedure concerns electrode preparation, and in particular the cleaning and polishing of the working electrode, and the casting of catalyst thin films onto its surface. The recommended approach to cleaning and polishing conforms to the prior description, in terms of the use of distilled water, alumina slurry and polishing pads. In preparing the catalyst film for testing, a dropcasting method is recommended, in which a known volume of well sonicated catalyst ink is pipetted onto the electrode surface. Garsany et al focussed in their initial publication [157] on the importance of the quality of the film deposited, and the strong influence that this had on measured catalytic activities. Indeed in their work the researchers draw attention to measurements of “good” and “bad” quality films of the same catalyst, noting very significant divergences. In further work aiming to account for and manage this feature, the researchers proposed a drying technique in which thin films are deposited onto electrodes connected to inverted rotating disk electrode arms, and are subsequently dried under rotation in order to avoid the “coffee ring effect,” observed in static drying, in which surface tension drives catalyst particles in the pipetted suspension to dry around the edges of an electrode surface. The researchers reported significant improvements in catalyst film quality and thereafter in measured catalyst activities [160] and the protocol has since been widely adopted, including in the work which follows.

The experimental methodology adopted for ORR experiments in this work is described in detail in the next section. Briefly, though, it is worth highlighting some theoretical concepts and background information pertinent to this work. As noted previously, the use of rotating disk electrodes (RDE) in ORR experiments is common, in order to mitigate diffusion limitations on the supply of reactant oxygen. Thus the working electrode of choice for most ORR measurements is an RDE tip in which a glassy carbon disk is embedded in a Teflon holder, which can be screwed into the rotator arm in order to establish electrical contact. The electrode surface is typically prepared as described previously and then immersed in electrolyte. A dilute perchloric acid ($HClO_4$) electrolyte is preferred because this is the electrolyte most representative of the environment found in real world fuel cells, due to the use of a perfluoro-sulfonic acid Nafion ionomer membrane [157], in which the bound sulfonic acid groups adsorb only very weakly into the surrounding humidified environment. Prior to carrying out any measurements, the electrolyte must be purged using nitrogen in order to create a de-oxygenated environment in which background measurements can be recorded [157]. Thereafter, the catalyst is first electrochemically cleaned and conditioned over the course of a high number of slow scans, cycling from low to high potentials, in order to remove surface-bound organic molecules and adsorbed species ahead of conducting measurements [161]. As is described in detail in the section which follows, measurements of electrochemically active surface area (ECSA) and background activity measurements can then be carried out, prior to bubbling oxygen into the solution and repeating the procedure to measure ORR activity. Data derived from these measurements can thus be normalised in order to facilitate easy comparison of catalyst activities, processed using Equation 3, Equation 4, and Equation 5. Three parameters are of interest in terms of benchmarking the catalysts; namely their ECSA, their area-specific activity, and the mass-specific activity [157]. The ECSA is calculated using Equation 3, with reliance on measurement of the charge associated with hydrogen absorption onto the electrode during measurement, as follows.

$$ECSA = [\frac{Q_H}{(210 \times L_{Cat} \times A_g)}]10^5$$

Equation 3. Calculation of the catalyst electrochemically active surface area, where Q_H is the charge arising due to hydrogen adsorption on the electrode, L_{Cat} is the catalyst loading in mg per cm^2, and A_g is the geometric area of the electrode surface in cm^2 [154].

Q_H is the charge associated with hydrogen adsorption onto the electrode, calculated by integrating to find the area under the curve in the hydrogen adsorption region of the CV, between 0.15 and −0.2 V (both vs Ag/AgCl). 210 refers to the 210 μC per cm^2 conversion factor which represents the standard charge associated with monoatomic hydrogen adsorption onto a clean, polycrystalline, Pt cuboidal surface. This parameter derives surface coverage from the charge. L_{Cat} is the catalyst loading in mg per cm^2, and A_g is the geometric area of the electrode surface in cm^2 [157].

Catalyst ORR activities are quantified using linear sweep voltammetry measurements (LSVs), which are conducted in the same manner as CV scans, only without the backwards scan. In ORR measurements, the LSV scan is carried out from high potential down to low, and the ORR activity can be calculated from the currents recorded. Specifically, the activity is calculated using currents recorded in the potential region during which the reaction is under mixed kinetic and diffusion limited control in the range 0.3 - 0.5 V, and also that in diffusion limited range, 0.0 - −0.2 V, both vs Ag/AgCl. The calculation used is described by Equation 4.

$$I_k = \frac{I_{lim} \times I}{(I_{lim} - I)}$$

Equation 4. Mass transport correction, used to calculate the kinetic current arising. Where I_k is the kinetic current, I_{lim} is the current recorded in the diffusion limited region, and I is the current recorded at the half-wave potential.

Where I_k is the kinetic current, I is the current measured at the half wave potential, the mid point in the non-diffusion limited region of the curve, around 0.4 V, and I_{lim} is the current at E = −0.1 V, both potentials vs Ag/AgCl. Catalyst mass-specific activities are estimated through normalisation of the calculated kinetic current to the known mass of catalyst deposited on the electrode [157].

Area-specific activities can also be estimated from the kinetic current, normalised to the electrochemically active surface area of catalyst on the electrode using Equation 5.

$$I_s = \frac{I_k}{(\frac{Q_H}{210})}$$

Equation 5. Calculation of catalyst area-specific activity, where I_s is area-specific activity, I_k is the previously calculated kinetic current, Q_H is the hydrogen absorption charge, as noted previously, and 210 refers to the 210 µC per cm^2 conversion factor previously mentioned [154].

A potential pitfall in using these equations for the work described here is the observation that the standard 210 µC per cm^2 conversion charge factor thus far referenced refers to the charge associated with hydrogen absorption onto a purely Pt polycrystalline surface. In mixed alloy nanoparticles it is unlikely that the catalyst surface measured will absorb hydrogen in a manner analogous to a pure Pt surface. However, other researchers cognisant of this challenge have already addressed the potential discrepancy. In a recent publication describing a novel cleaning protocol for mixed Ru@Pt nanocatalyst testing, Jackson and colleagues reported measurements on their mixed particles which aligned closely to anticipated hydrogen absorption charges for polycrystalline Pt surfaces following extended potential window cycling [161] during the electrochemical activation step. Crediting the success of their intervention to surface reorganisation following cleaning cycling, the researchers noted that in these instances it was reasonable to use the Pt Q_H value for their ORR activity benchmarking calculations. Their cleaning protocol was adopted for the experiments which are described hereafter.

Despite widespread recognition of the protocols described within the fuel cell electrocatalyst research community, standardisation and accurate benchmarking of catalyst activity reporting is still a challenge. A further work from

Garsany and colleagues looked to quantify this by comparing like for like protocols and measured results in two laboratories. In their comparison the authors highlighted the many variables which can influence electrochemically determined catalyst activities, including glassware cleanliness, the film preparation methods adopted, the choice of electrolyte and electrodes and the potential windows used for measurements [158]. The recommendations from this report have been adopted in developing the measurement protocols which followed.

In addition to the techniques and experiments described in prior sections, a further physical characterisation technique was drawn upon in order to contextualise some of the electrochemical work which follows. Thermogravimetric analysis (TGA) is a useful technique for materials characterisation, and relies upon measuring the mass of a sample as a function of temperature and time, as the sample is heated in a controlled manner. In TGA, a sample is weighed out onto a mass balance and heated to high temperatures under a controlled gaseous atmosphere. The mass balance is used to measure changes in mass which occur as a result of the heating process. These measurements can provide a range of useful information on the composition of the sample under study, for example in monitoring losses of solvent (including water) from the sample, in evaluating its degradation and decomposition mechanisms, and in measuring the contribution of plasticiser components in the thermal properties of polymeric materials [162]. In the present work, TGA has been used to measure metal nanoparticle loading on the carbon black molecules in the catalyst powders prepared. This is a fundamental requirement for accurate comparison of electrochemical testing of catalysts, in that cognisance of the mass of catalyst in a given sample is essential in communicating its relative efficacity.

4.2 Aims and Objectives

The work described thus far focussed on developing optimised protocols intended to deliver nanoparticle catalysts with high activity and durability for application in polymer electrolyte fuel cell electrocatalysis. This section relates to subsequent work to test and benchmark those nanoparticle catalysts against prepared standards and commercial catalyst products. The work described here aims to;

- Confer an understanding of the relative catalytic activity of the prepared catalysts with respect to each other, as well as to catalysts which are available from commercial manufacturers;
    - verify work by other researchers in developing enhanced electrochemical conditioning and testing protocols, and in particular to ensure conformance with efforts towards standardising reporting of determined catalytic activities;
    - and, in so doing, contextualise the wider work described thus far in terms of its progress towards the ultimate and fundamental goal of designing and developing an optimised novel catalyst.

4.3 Methods

4.3.1 Chemical and Physical Characterisation

This section relates to physical characterisation measurements aimed at understanding the total metal loading in the catalyst powders prepared, which is an essential parameter in determining the activity of the catalyst per given unit of mass.

4.3.1.1 Thermogravimetric Analysis (TGA)

~2 mg samples of as prepared carbon-supported nanoparticle catalyst powders were weighed into alumina crucibles for thermogravimetric analysis (TGA) measurements. A Perkin Elmer TGA 8000 at the University of Durham Department of Chemistry was used. The instrument was operated by William Douglas Carswell. Air was used as the purge gas, with 30 mL flowed across the sample per minute. The runs were carried out between 30 and 700 °C, at a heating ramp rate of 10 °C per minute. The mass of the sample was recorded as a function of time and temperature, in order to monitor changes in mass through heating. The residual mass remaining after the run was completed was taken to be the mass of metal nanoparticles loaded on the carbon support material, with this loading value used for subsequent calculations.

4.3.2 Electrochemical Characterisation

The work reported in this section relates to each stage of the process towards conducting electrochemical testing aimed at verifying and benchmarking the activity of the catalysts prepared.

4.3.2.1 Catalyst Ink Preparation

A Nafion solution was prepared by pipetting 20 µL of Nafion into 5 mL of a 20:80% v/v isopropyl alcohol:deionised water solution, which was mixed thoroughly by sonicating for 10 minutes. This solution was prepared freshly each day. Catalyst inks were prepared by dispersing 1 mg of catalyst powder in 1 mL of this Nafion solution. The subsequent ink solutions were then sonicated for 30 minutes to ensure even mixing and dispersion, prior to dropcasting. Inks were prepared for all of the nanoparticle preparations thus far described, as well as two commercial standards against which those nanoparticles were benchmarked. Those standards were manufactured by Johnson Matthey and obtained from Sigma Aldrich. Namely, the standards were HiSpec 3000 Pt (20% loading) and HiSpec 12100 PtRu (48% Pt, 24% Ru).

4.3.2.2 Electrode Preparation

A standard three electrode electrochemical setup was used. The platinum mesh counter electrode and double junction Ag/AgCl (saturated) reference electrode were cleaned using distilled water. The mesh counter electrode was also flamed using a Bunsen burner, to remove any solid species. These electrodes were then set aside, ready for the assembly of the electrochemical cell. Meanwhile, the working electrode was prepared. A 5 mm glassy carbon (GC) rotating disk electrode tip was used. To ensure an even surface and to remove adsorbed species, the electrode was polished before use on Microcloth^{TM} polishing paper, using three successive grades of alumina slurry (1 µm, 0.3 µm and 0.05 µm, sequentially). Both the polishing paper pads and slurry were sourced from Buhler. Once polished, the electrode was rinsed with deionised water and dried under a lamp. As prepared catalyst inks could then be dropcast onto the electrode surface, as per a published procedure [160]. The procedure was developed to ensure even drying of the catalyst film on the electrode substrate. Briefly, the electrode tip was screwed into an inverted Pine Instruments rotating disk electrode arm. With rotation set to 0 RPM, a micropipette was used to drop 10 µL of sonicated catalyst ink onto the electrode surface. Slowly, the rotation was raised to 400 RPM, and under continued rotation the film was left to dry for around 30 minutes.

4.3.2.3 Electrolyte Preparation

Perchloric acid ($HClO_4$) electrolyte was used for all measurements. The electrolyte was prepared by dissolving 2.156 mL $HClO_4$ (Sigma Aldrich) in 62.5 mL of deionised water in a 250 mL calibration flask. Further deionised water was then added to bring the volume up to the 250 mL calibration mark. The flask was agitated to ensure mixing.

4.3.2.4 Electrochemical Testing Protocol

A three neck, 150 mL glass electrochemical cell was used for all measurements. The cell was acid washed between uses with sulphuric acid, which was left to soak overnight, to remove any adsorbed species, in a manner as described in a published method [157]. Thereafter the cell would be rinsed well, five times, with deionised water before use. 100 mL of electrolyte was then measured out using a measuring cylinder, and added to the cell. The electrodes could then be assembled. Crocodile clips were used to connect the platinum counter and

Ag/AgCl (saturated) double junction reference electrodes to the potentiostat, an Autolab PGSTAT302N, which had been acquired from Metrohm. The working electrode rotating disk tip was screwed into a Pine Instruments rotating arm, which also connected to the potentiostat. Measurements were carried out at room temperature (25 °C). Prior to commencing any measurements, the electrolyte was purged and degassed with flowing nitrogen gas for 30 minutes.

Nova 2.0 software was used to control the potentiostat and record the currents generated in response to the potentials applied. All potentials referred to here and reported hereafter are relative to Ag/AgCl. Once the electrolyte had been fully degassed, the rotator was used to remove any bubbles from the working electrode surface, by rotating it at 800 RPM. Thereafter, electrochemical conditioning and cleaning cycles were commenced, following a protocol adapted from a published method [161]. 50 cleaning cycles were undertaken, between potentials of 0.3 V to 1.4 V, at a scan rate of 500 mV per second. Thereafter, following a standardised method optimised for comparing electrocatalytic activity data between catalysts [158], electrochemical surface area and catalyst activity measurements were made. Surface area measurements were taken by carrying out three cyclic voltammogram scans, between potentials of −0.3 and 1.2 V, at a scan rate of 50 mV per second. Further purging and degassing was undertaken before and between activity measurements, which were carried out in a nitrogen environment to establish background measurements, and thereafter in an oxygen environment to measure catalyst activity towards oxygen reduction. First, linear sweep voltammograms were measured at rotation rates of 400, 800, 1200, 1600 and 2000 RPM, sequentially, with flowing nitrogen used to purge the electrolyte for 20 minutes between scans. Thereafter, an oxygen flow was supplied to the electrolyte for 30 minutes, before commencing further linear sweep voltammogram measurements under rotation, also at 400, 800, 1200, 1600 and 2000 RPM, and again with further oxygen flowed for 20 minutes between measurements.

4.4 Results and Discussion

4.4.1 Thermogravimetric Analysis (TGA)

TGA measurements were used to determine the metal loading on the catalyst nanoparticles prepared, as described in method 4.3.1.1. Six runs were carried out in total on samples of the as prepared RuSePt High, RuSePt Low, PtRu and Pt nanoparticles so far described. Measurements were also carried out on oleylamine and blank carbon black powder, both as controls. These measurements were primarily used to ascertain the loading of metal nanoparticles onto the carbon support powder, in order to inform subsequent electrochemical calculations. The results of those measurements are summarised in Table 9. Single measurements were carried out for each sample due to instrument availability constraints, limiting the reliability of the results.

Table 9. Summary of catalyst metal loading insights arrived at using TGA measurements, where the (nanoparticle) catalyst mass per mg refers to the mass of metal nanoparticles per mg of catalyst powder.

Sample	**Mass at 700 ℃ (%)**	**Metal Loading (%)**	**Catalyst Mass per mg (mg)**
RuSePt High	9.05	9.05	0.091
RuSePt Low	5.24	5.24	0.052
PtRu	4.89	4.89	0.049
Pt	9.04	9.04	0.090
Oleylamine	0.00	0.00	0.000
Carbon Black	66.02	0.00	0.000

Figure 35 also collates the plots acquired from the runs, which show relatively comparable combustion patterns for the non-metal components in the catalyst samples a-d. It is worth highlighting that the carbon black sample shows very different combustion behaviour to the carbon black in the catalyst-containing samples. The mass loss observed in the bare carbon black sample, f, is much lower and slower, with a final mass of 66% measured at 700 °C. The noble metals in the catalyst-containing samples are known to catalyse the combustion of carbon black [110], explaining the much faster and indeed complete combustion observed in plots a-d.

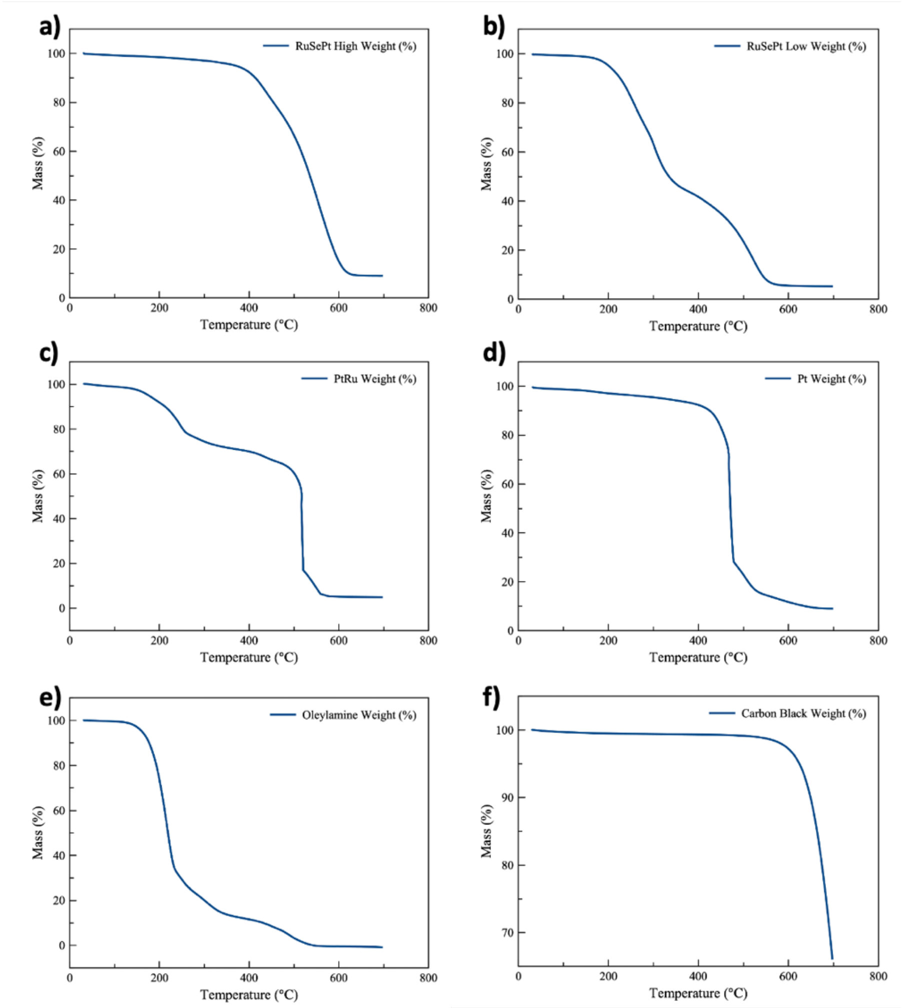

Figure 35. Plots of TGA measurements on a) RuSePt High/C, b) RuSePt Low/C, c) PtRu/C, and d) Pt/C nanoparticle catalyst powders, as well as oleylamine, e), and bare carbon black, f).

4.4.2 Electrochemical Testing

The metal loading values calculated previously were used to determine catalyst loading per electrode, Table 10, using a straightforward calculation given the consistent dropcasting method (method 4.3.2.2) used to deposit catalyst films onto the working electrode. Known catalyst ink volumes were pipetted onto the electrode surface in all cases. Electrochemical testing was carried out as described in method 4.3.2.4, on all of the nanoparticle catalyst samples thus far described, including the as prepared nanoparticles, the acid treated nanoparticles, the heat treated nanoparticles, and as received commercial standards HiSpec 3000 Pt and HiSpec 12100 PtRu, as noted in Table 10. Results from these tests are summarised below in successive figures and tables according to the categories described. In each case, data from cyclic voltammogram (CV) and linear sweep voltammogram (LSV) measurements is shown and discussed. The CV measurements were used to calculate the catalyst electrochemically active surface area (ECSA), while the LSV tests provided the data required to ascertain catalyst activity for the oxygen reduction reaction (ORR).

Table 10. Catalyst metal loading as calculated from prior TGA results, using known volumes of catalyst ink pipetted on to electrodes.

Sample	**Metal Loading (%)**	**Catalyst Mass per mg (mg)**	**Metal Loading per Electrode (mg per cm^2)**
RuSePt High	9.05	0.091	4.64E−03
RuSePt Low	5.24	0.052	2.65E−03
PtRu	4.89	0.049	2.50E−03
Pt	9.04	0.090	4.59E−03
HiSpec 3000 Pt	20.00	0.200	1.02E−02
HiSpec 12100 PtRu	72.00	0.720	3.67E−02

The first batch of measurements concerned the as prepared and as received particles. The voltammograms recorded are collated in Figure 36.

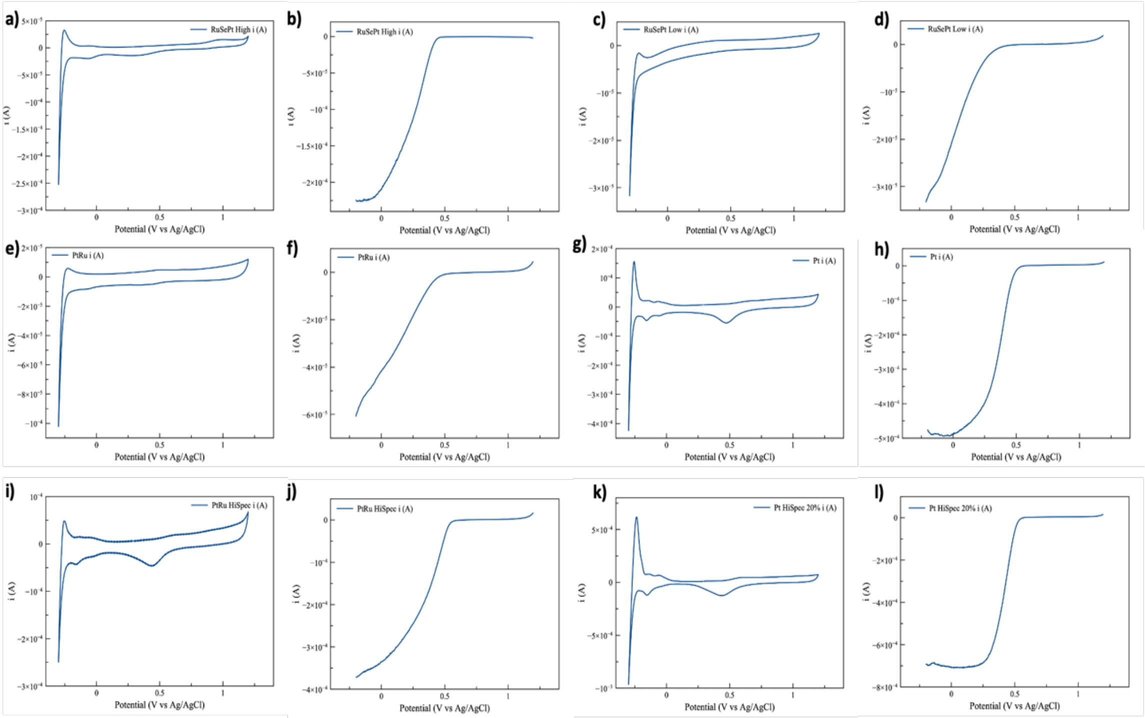

Figure 36. CV measurements for a) RuSePt High/C, c) RuSePt Low/C, e) PtRu/C, g) Pt/C, i) HiSpec PtRu/C, and k) HiSpec Pt/C catalysts. LSV measurements for b) RuSePt High/C, d) RuSePt Low/C, f) PtRu/C, h) Pt/C, j) HiSpec PtRu/C, and l) HiSpec Pt/C catalysts.

Comparing the CV measurements, Figure 36, a, c, e, g, i and k, a few qualitative observations are apparent. The RuSePt High/C, RuSePt Low/C and PtRu/C CVs, a-e, are broadly similar, although more defined peaks are visible in the RuSePt/ High/C case, a. The CVs of the as prepared Pt/C catalyst, g, and those of the commercial Pt and PtRu catalysts, i and k respectively, are more similar to one another, with clearer peaks, particularly in the of-interest hydrogen adsorption/desorption region 0 - −0.2 V (vs Ag/AgCl). The as prepared Pt/C scan, g, is so similar, in fact, to the commercial Pt/C scan, k, that it highlights the difference in surface character between these and the other samples prepared.

This observation reinforces the conclusion noted in earlier sections that surfaces of the as prepared RuSePt High/C, RuSePt Low/C and PtRu/C are not composed of segregated Pt, but are mixed surfaces composed of varying combinations of the three elements. Turning to the LSV scans, still Figure 36, b, d, f, h, j, l, once again the distinction between the purely Pt systems and those which include the other elements is clear. The plots of the scans for the as prepared Pt/C catalyst and the commercial Pt/C catalyst, h and l, respectively, are very similar in shape, with well defined diffusion limited regions, in the potential window below 0 V (vs Ag/AgCl). This observation reflects the comparatively high activity and selectivity of these catalysts for the ORR, given that the diffusion limitation indicates that all of the oxygen available to that electrode surface has been reduced, exhausting the reactant supply. Meanwhile, the plots for the other catalysts, the as prepared RuSePt High/C, RuSePt Low/C, and PtRu/C, b, d, f, respectively, and indeed the plot for the commercial PtRu catalyst, j, show varying degrees of diffusion limitation, clear in the change in curve gradient, but none seem to have reached the same plateau shown in the cases of the Pt catalysts. This indicates that the catalysts did not exhaust the supply of oxygen during those measurements, as a result of their lower overall activites for the target reaction.

Reflecting on the activity values calculated for the catalysts using data from the above measurements enables quantitative analysis of the trends described. Those values are collated in Table 11.

Table 11. Summary of ECSA and activity values calculated for the as prepared nanoparticles and as received commercial catalysts.

Sample	ECSA (m^2 per g Pt)	I_k (A)	Mass Activity (mA per mg Pt)	Specific Activity (uA per cm^2 Pt)
RuSePt High	48.64 ± 3.68	−2.81E−04	60.58	115.18
RuSePt Low	22.58 ± 1.45	−5.72E−05	21.55	95.58
PtRu	45.07 ± 4.08	−8.41E−05	33.65	74.65
Pt	91.29 ± 6.34	−7.06E−04	153.82	168.57
HiSpec 3000 Pt	52.21 ± 2.41	−9.42E−04	92.35	34.68
HiSpec 12100 PtRu	17.65 ± 6.11	−6.57E−04	17.87	151.83

Surfactant load is known to strongly influence calculated ECSAs [127, 163, 164] for nanoparticle catalysts which have been prepared colloidally. Naturally, surfactant molecules coordinated to the nanoparticle surfaces will influence the degree to which reactants can access those surfaces, and the corresponding active sites, within a reactant solution. This context has informed the development of electrochemical cleaning protocols, with varying degrees of success. Pointing to the values calculated for the systems under study, Table 11, this phenomenon is well reflected in the low ECSA value of 22.58 m^2 per g Pt calculated for the as prepared RuSePt Low/C, which as noted in the previous chapter was associated with high surfactant load. It is notable that the highest activity values calculated, 153.82 mA per mg Pt mass activity and 168.57 μA per cm^2 Pt area-specific activity, were for the as prepared Pt/C system. This finding demonstrates clearly the pedigree of Pt-based materials in catalysing the ORR, and the challenge facing researchers who seek to develop novel alternatives. These values serve predominantly in this work as benchmarks for the subsequent studies which follow, which aimed to establish the degree to which the additional post-synthesis treatment protocols could deliver enhanced catalytic activities for the materials studied.

With this in mind, acid treated samples were also tested in the same manner. The voltammograms recorded are summarised in Figure 37, with calculated ECSA and activity values summarised in Table 12.

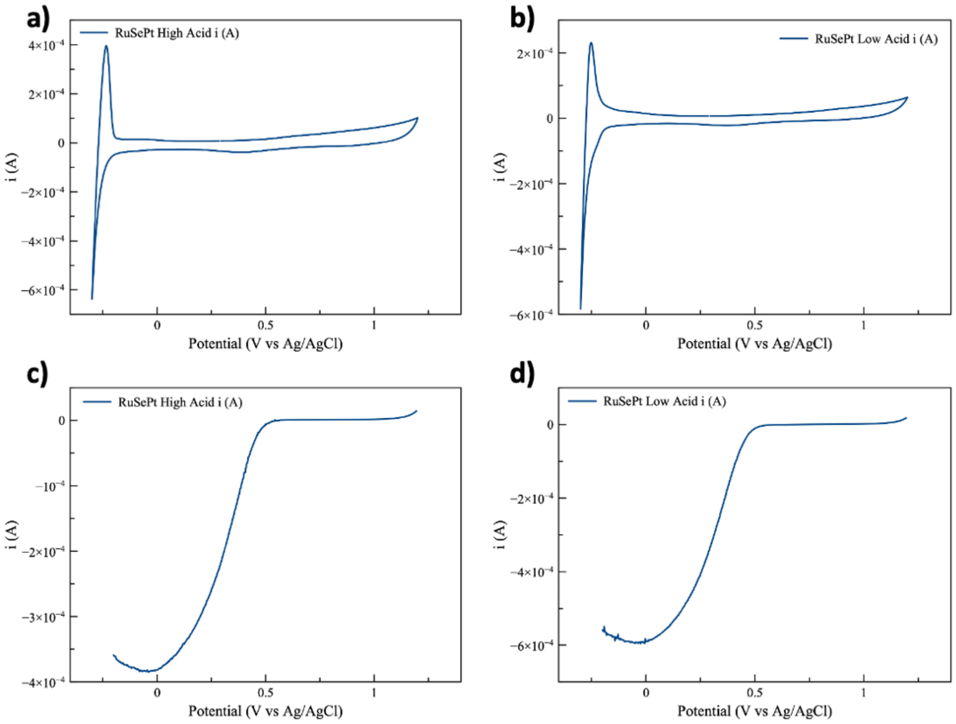

Figure 37. CV ECSA measurements for a) RuSePt High/C Acid Treated and b) RuSePt Low/C Acid Treated nanoparticle catalysts. LSV measurements c) for RuSePt High/C Acid Treated and d) RuSePt Low Acid Treated nanoparticles.

It is worth comparing the CVs and LSVs plotted for these acid treated samples, Figure 37, to those discussed above for the as prepared samples, Figure 36. In the acid treated case, Figure 37, the LSVs in particular show an immediate qualitative change as a result of the treatment step; these curves (c and d) are much closer in configuration to those for the pure Pt systems shown in Figure 36, h and l. Importantly, following acid treatment, these measurements (c and d, Figure 37) show that ORR reactions catalysed by these materials are reaching the diffusion limited plateau described previously; this indicates that the catalytic activity and/or selectivity of the acid treated samples has indeed been improved, relative to the untreated samples.

Analysis of the mass and specific activities calculated (Table 12) for the acid treated catalysts further contextualises this conclusion. Significant increases were observed in mass activity for both systems, with the RuSePt High/C mass activity increasing from 60.58 to 115.43 mA per mg Pt following acid treatment, and a bigger increase from 21.55 to 307.42 mA per mg Pt recorded for the acid treated RuSePt Low/C material. These increases are likely attributed to the removal of surface bound surfactant molecules and Se atoms, improving reactant access to the catalyst active sites. This observation makes clear the merit of an acid treatment protocol in conditioning nanocatalyst surfaces.

The impact of acid treatment on the calculated specific activities is less straightforward, however. The specific activity recorded for acid treated RuSePt High/C fell from 115.18 to 112.91 µA per cm^2 Pt, due to a decrease in recorded ECSA from 48.64 to 20.22 m^2 per g Pt. Nanoparticle agglomeration in catalysts is known to lower ECSA [163, 165] due to obvious reduction in the size of the potentially reactive surface which follows as a result. As noted in the prior chapter, acid treatment caused some agglomeration of both sets of particles, due presumably to the removal of stabilising surfactant molecules. The relationship between mass and specific activities is explored in more detail further in this chapter given its impact on all of the results concerned.

Table 12. Summary of ECSA and activity values calculated for the acid treated catalysts.

Sample	**ECSA (m^2 per g Pt)**	**I_k (A)**	**Mass Activity (mA per mg Pt)**	**Specific Activity (uA per cm^2 Pt)**
RuSePt High	48.64 ± 3.68	−2.81E−04	60.58	115.18
RuSePt High Acid	20.22 ± 4.11	−5.36E−04	115.43	112.91
RuSePt Low	22.58 ± 1.45	−5.72E−05	21.55	95.58
RuSe Pt Low Acid	21.87 ± 2.91	−8.16E−04	307.42	275.52

All of the as prepared catalysts were also heat treated, as described in method 3.3.1.4. They were also all subsequently tested to determine the impact of those treatments on their ECSA and catalytic activity. The findings from these experiments are discussed below, with the voltammograms depicted in Figure 38 and the data collated in Table 13.

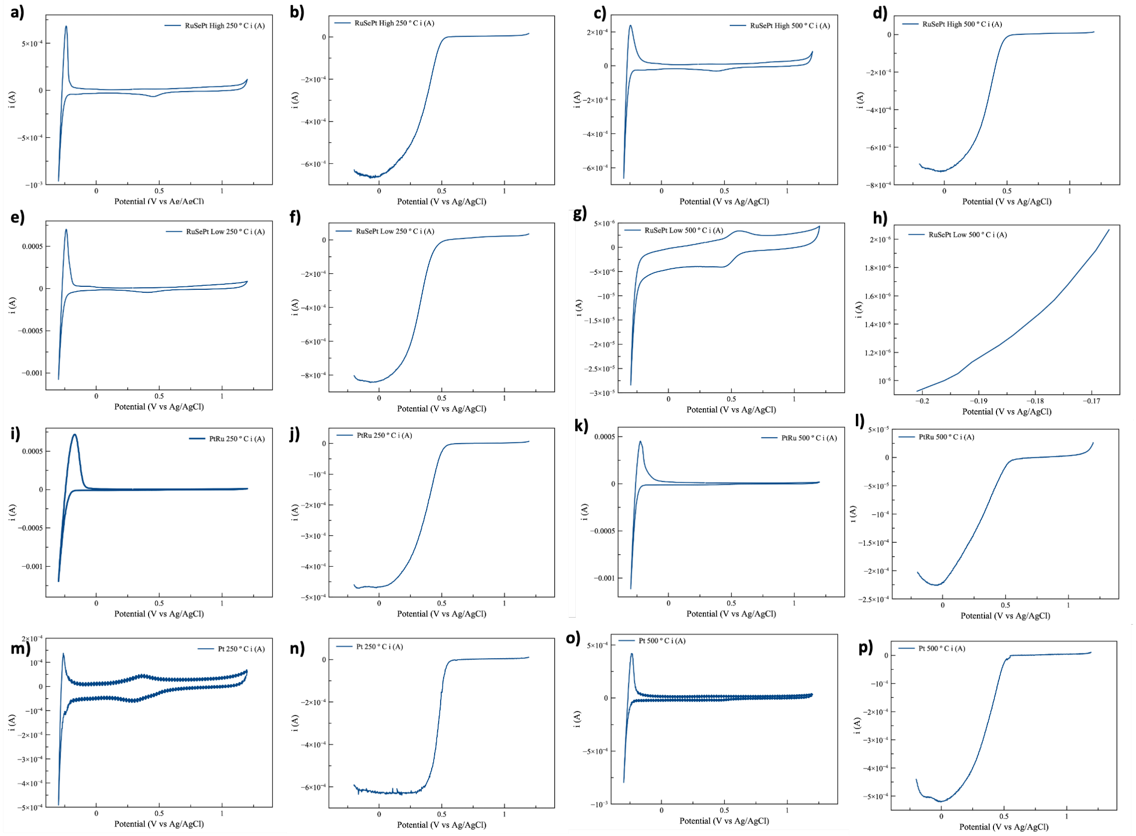

Figure 38. CV ECSA measurements for a) RuSePt High/C 250 °C, c) RuSePt High/C 500 °C, e) RuSePt Low/C 250 °C, g) RuSePt Low/C 500 °C, i) PtRu 250/C °C, k) PtRu/C 500 °C, m) Pt/C 250 °C, o) Pt/C 500 °C, and LSV measurements for b) RuSePt High/C 250 °C, d) RuSePt High/C 500 °C, f) RuSePt Low/C 250 °C, h) RuSePt Low/C 500 °C, j) PtRu 250/C °C, l) PtRu/C 500 °C, n) Pt/C 250 °C, p) Pt/C 500 °C.

As with the discussion up to this point, straightforward qualitative observations can be made in comparing the CVs and LSVs for the heat treated samples, summarised in Figure 38, with those plotted for the measurements on the as prepared samples, Figure 36. In Figure 38, the LSV plots in particular show that all of the heat treated samples with the exception of RuSePt Low 500 °C, h, show improved ORR activity over the non-heat treated plots, Figure 36. This conclusion is two-fold in nature; the plots show that a diffusion limited plateau was reached in each reaction, indicating higher activity than in the as prepared cases, and the currents recorded were higher. The outlying nature of the RuSePt Low 500 °C plots, g and h, Figure 38, is explained by challenges in preparing inks for this catalyst, associated with poor solubility of the catalyst powder, which resulted in the preparation of poor quality catalyst films across successive batches. Both the wholesale improvement in activities observed for the other samples, and the poor performance of the RuSePt Low 500 °C sample are reflected in the values obtained from subsequent calculations, tabulated in Table 13.

The significant activity improvements observed are very clear when compared on both a mass and activity basis. Heat treatment delivered substantially enhanced activities across the board, despite the reduced ECSAs which arose due to agglomeration of the particles. For the RuSePt Low/C, PtRu/C and Pt/C samples, the highest mass activities were recorded for the samples treated at 250 °C, with values of 405.99, 254.58 and 199.74 mA per mg Pt recorded, respectively. This temperature presumably represented a balance between removing sufficient surfactant and/or improving the chemical ordering of the metal atoms while not encouraging too much agglomeration of the particles, which as discussed reduces the surface area and thus availability of active sites. In the RuSePt High/C case the mass activity for the sample treated at 500 °C was the highest recorded, however, perhaps due to the added dynamic of the potential at that temperature to remove surface-bound Se atoms and influence the configuration of the Pt and Ru components of the nanoparticles.

Table 13. Summary of values calculated using data from the above measurements, characterising the catalytic activity of the heat treated nanoparticle catalysts prepared.

Sample	**ECSA (m^2 per g Pt)**	**I_k (A)**	**Mass Activity (mA per mg Pt)**	**Specific Activity (uA per cm^2 Pt)**
RuSePt High	48.64 ± 3.68	−2.81E−04	60.58	115.18
RuSePt High 250 ℃	21.36 ± 5.07	−9.20E−04	198.20	182.01
RuSePt High 500 ℃	13.18 ± 4.29	−9.54E−04	359.64	305.75
RuSePt Low	22.58 ± 1.45	−5.72E−05	21.55	95.58
RuSePt Low 250 ℃	25.85 ± 2.23	−1.08E−03	405.99	308.15
RuSePt Low 500 ℃	5.37 ± 3.66	−8.77E−06	3.30	12.07
PtRu	45.07 ± 4.08	−8.41E−05	33.65	74.65
PtRu 250 ℃	13.05 ± 3.13	−6.36E−04	254.58	382.38
PtRu High 500 ℃	14.02 ± 2.89	−2.83E−04	113.13	158.19
Pt	91.29 ± 6.34	−7.06E−04	153.82	168.57
Pt 250 ℃	32.86 ± 4.54	−9.17E−04	199.74	119.19
Pt 500 ℃	13.66 ± 2.74	−6.28E−04	136.86	196.42

As highlighted in the literature review which introduced this thesis, much research has been carried out on the use of heat treatments to optimise nanocatalyst chemistries and thus tweak measured activities. Of particular relevance to this work is similar activity enhancements reported for Pt_3Co alloy [54] and Ru@Pt [67] nanoparticles, which the authors ascribed to improved chemical ordering in their alloys. This phenomenon has likely been replicated in the work described, with ordering enhancement an additional explanation (in addition to surfactant and Se layer removal) for the activity improvements observed in the catalyst nanoparticles under study. Given the alloy-like configuration observed for the RuSePt Low nanoparticles during STEM-EELS experiments (Figure 21), this would in particular explain the substantially increased activities measured in the RuSePt Low 250 °C case.

4.5 Conclusions

The RuSePt Low 250 °C sample is the standout leader from the above discussion, but in drawing further conclusions it bears comparing the activities measured across the board as a result of the range of treatments described. As such, the mass activities of all catalysts tested is collated in Table 14.

Table 14. Summary of mass activities measured for all catalysts, arranged in descending order.

Sample	Mass Activity (mA per mg Pt)
RuSePt Low 250 ℃	405.99
RuSePt High 500 ℃	359.64
RuSe Pt Low Acid	307.42
PtRu 250 ℃	254.58
Pt 250 ℃	199.74
RuSePt High 250 ℃	198.20
Pt	153.82
Pt 500 ℃	136.86
RuSePt High Acid	115.43
PtRu High 500 ℃	113.13
HiSpec 3000 Pt	92.35
RuSePt High	60.58
PtRu	33.65
RuSePt Low	21.55
HiSpec 12100 PtRu	17.87
RuSePt Low 500 ℃	3.30

Mass activity was chosen as the key metric because normalising the reported activity using a physically determined attribute (metal loading) is helpful in comparing the values measured with those reported by other researchers. There is an (obvious) correlation between ECSA and specific activity. Normalising the activity measured to the catalyst area can appear to exaggerate the activities reported for catalysts with particularly low ECSAs, which can make benchmarking difficult.

In terms of general trends from this work, Table 14 succinctly highlights the overall utility of heat treatment as a means of enhancing catalyst activities. That is likely due first and foremost to the removal of active site-blocking surfactant molecules, but also to the influence that heat treatment can exert on the chemical configuration of the alloy nanoparticles. As highlighted, the RuSePt Low/C sample treated at 250 °C has a measured mass activity that is 18.8 times higher than that of the as prepared sample (405.99 vs 21.55 mA per mg Pt). This measured mass activity is also 4.4 times higher than that of the commercial HiSpec Pt/C powder, which is a significant benchmark. Notable further activity enhancements are those observed for the RuSePt High 500 °C and PtRu 250 °C systems, which both have six times higher activities than the as prepared analogues (359.64 vs 60.58 and 254.58 vs 33.65 mA per mg Pt, respectively).

The acid treatment protocol also fares well in the comparison to the as prepared catalysts, with mass activities for both treated samples higher than the respective as prepared materials. With an activity of 307.42 mA per mg Pt, the RuSePt Low acid treated sample ranks as the third most active catalyst studied. These activity enhancements are also assumed to have been delivered due to the effect of the protocol on the nanoparticle surface configuration, likely through the removal of adsorbed surfactant and Se molecules and atoms, respectively, which would have obscured active sites in the as prepared catalysts.

In designing the experiments described in this chapter, close attention was paid to work already cited by researchers aiming to improve standardisation of catalyst activity measurements and reporting [157, 158, 160]. In two particular reports [157, 158], those authors drew attention to the wide range of activities reported, even for commercial catalysts, with selected mass activities reported for commercial Pt ranging from ~200-600 mA per mg Pt. Other authors have highlighted reported activities for similar commercial materials in the range 28-266 mA per mg Pt [156]. Using these ranges as a reference point and benchmark, it is clear that the mass activities summarised in Table 14 are within conceivable realms and indeed that the heat and acid treated materials studied represent good candidate materials for potentially enhanced fuel cell ORR electrocatalysis.

As well as validating the merit of the acid and heat treatment protocols adopted in this study, these results also suggest that incorporating Se in the precursor mixtures studied contributed to enhanced catalysis, given the higher activities measured for the Se-containing materials. The unique properties of transition metal chalcogenide materials is a field of chemical study unto itself, and researchers have characterised $PtSe_2$ films electrochemically [137], as noted already, and explored the utility of the same material for use in semiconductor applications [166, 167]. The development of CdSe@Pt [109] and RuSe [81, 82, 84] catalysts has already been surveyed, too. However, as far as the researcher can tell from surveying the academic literature, this work is the first attempt to leverage the benefits of a system combining Pt, Ru and Se. Given the favourable catalytic activities reported, there is scope for interested parties to further explore the phenomena described in pursuit of the development of optimised catalysts.

5 Conclusions and Recommendations

5.1 Conclusions

This report has focussed on efforts to develop a range of protocols to prepare, optimise and characterise a series of nanoparticle catalyst materials composed of varying ratios of Pt, Ru and Se. The intended application for these nanoparticles was fuel cell electrocatalysis, with a specific focus on the oxygen reduction reaction (ORR) that is integral to the operation of many fuel cell types, including the polymer electrolyte fuel cell. The aim of this work at inception was to prepare and test core-shell RuSe@Pt nanoparticles, with robust and stable RuSe cores layered with thin Pt shells. The rationale behind this aim of targeting a core@shell morphology was relatively straightforward; Ru is a significantly cheaper metal than Pt (and Se is even cheaper), so displacing most of Pt mass in the product particle with these other materials would lower the cost of the product particle. An idealised core@shell particle has a very thin outer layer of the shell material, ensuring a high surface area of that material using very little mass. The introduction to this thesis considered in detail the means through which countless researchers have pursued the goal of developing just such an idealised Pt-shell particle for fuel cell ORR. Work has been reported in which Pt has been combined with just about every possible transition metal element, with claims made about the ensuing benefits achieved in terms of catalyst activity, economy and durability. Many of these efforts prove to deliver very promising results against one of these aims, but fall short against the other benchmarks, for example with highly active catalysts that are prone to corrosive degradation in the chemical environment inherent to the application, or in complex alloys of platinum group metals which deliver active and durable catalysts which would likely be more expensive to produce commercially than the standard Pt/C. This context informed the design of the system described in this work; as a well characterised, stable catalyst in its own right, RuSe was expected to provide a stable and reliable core material at low cost, onto which a highly active Pt layer could be deposited. Ru is (relatively) close to Pt in atomic radii and electronegativity, at least when compared to many of the other candidate core materials studied by others. With this in mind, it was anticipated that an electronics/strain balance could be struck, where the Ru core could confer sufficient electronic influence and physical lattice strain on atoms in the Pt shell such as to lower the Pt d band energy, and improve the reactivity of the product surface for the ORR, without exerting such strain as to undermine the stability of the product particles.

Naturally the execution of the strategy devised prove to be less than straightforward. Analogous materials, CdSe and CdSe@Pt, and synthetic approaches to their preparation, were identified in the process of developing synthetic protocols intended to deliver the target RuSe@Pt particles. These protocols were adapted to the target system, with limited success. Although RuSe particles were prepared and isolated, attempts to coat those with Pt failed, likely due to handling issues associated with the complex nature of the two step procedure adopted. This procedure required a phase transfer step, and involved further heating of the supernatant RuSe solution, which seemed to result in further growth of those particles. This prevented the deposition of a controlled Pt layer. A key conclusion at this stage in the work concerned the value of simplifying the synthetic approach as far as possible, given the inherent complexities of attempting to exert control over processes occurring at atomic scales.

Further efforts thereafter focussed on developing a one step method, to improve handling of the particles. This method relied on migration of the atoms constituent to the nanoparticles towards the thermodynamically determined configuration, namely with Ru in the core and Pt in the shell. This method was further optimised, to consider the impact of the type of precursors and surfactants used, with acetylacetonate Ru and Pt precursors proving to be the most reliable in the oleylamine medium adopted, in which oleylamine was used as solvent, reducing agent and surfactant. This optimised method was then used to prepare mixed RuSePt nanoparticles, and was further adapted to also prepare standard particles composed just of Pt and PtRu, to aid in characterising the target particles. To the author’s knowledge, this is the first instance in which the preparation of nanoparticles composed of these three elements has been reported. The significant conclusion from this aspect of the work concerned the vital role that the precursor chemistry and surfactant molarity played in determining the outcome of the synthesis procedures developed. There is clearly significant scope for researchers to optimise their protocols in this regard.

Preliminary characterisation of the prepared RuSePt particles suggested that the product particles contained more Se than had been intended, with the likely formation of an Se shell layer on the particle surfaces. This was anticipated to impede optimal catalysis on those surfaces, so a further synthetic protocol in which reduced molarities of Se precursors were used. This gave rise to the RuSePt High and RuSePt Low systems taken forward and fully characterised and tested in the later stages of the work described. The RuSePt High particles were prepared with 0.02 molar equivalent of Se precursor, relative to the 0.002 molar equivalent used in the RuSePt Low case. In both cases, 0.04 molarities of Ru and Pt precursors were incorporated. The RuSePt Low particles exhibited completely different morphologies and dispersion patterns to the previously prepared RuSePt High particles. The former particles were spherical, small and very well dispersed, with little to no agglomeration observed, while the latter were broadly cuboidal in shape, slightly larger, and more prone to agglomeration. This observation indicated a significant role for Se in the mechanism of assembly of the product nanoparticles, which was interrogated using STEM-EELS experiments. These experiments showed that the RuSePt High particles formed as Pt particles with adsorbed RuSe layers, with varying degrees of coordination seen between particles, where as the RuSePt Low particles formed as mixed PtRu particles, with light surface decoration of Se. These distinctions clearly influenced the shape of the particles concerned. Prior research had shown that CO molecules liberated from the acetylacetonate precursor ligands used in these syntheses had coordinated to Pt surfaces, directing growth of morphologically cuboidal Pt nanostructures. This observation suggests that this effect was minimised in the RuSePt Low case, perhaps due to enhanced coordination to the PtRu surfaces of oleylamine surfactant molecules, which could have blocked the surfaces and prevented CO adsorption. Further mechanistic work would be required to verify this assertion and to aid in better understanding the phenomena at play. However, this finding suggests that researchers wishing to drive or direct nanoparticles to adopt certain morphologies could consider the role of adsorbed atoms and surfactant molecules in influencing those reactions.

Further to the adoption of a novel, low Se synthesis protocol, acid and heat treatment steps were developed to contribute to efforts to optimise the surfaces of the particles for enhanced catalysis. A significant body of research exists which has shown the merits of such procedures, in modifying catalyst surfaces through the removal of excess active site blocking surfactant molecules and adsorbed species, as well as through modifying the chemical or electronic configuration of the alloyed surfaces. Drawing on these prior works, all of the product particles thus far described were acid and heat treated, with the impacts of these treatments verified through chemical and physical characterisation, as well as subsequent electrochemical testing. The physical and chemical characterisation suggested that both treatments encouraged agglomeration of the particles and loss of individual particle morphology, to varying degrees depending on the manner in which the particle-surfactant dynamics were affected. Chemical characterisation suggested that post-treatment the particles were subject to varying degrees of oxidation. These findings in and of themselves were not especially insightful, given all of these effects could have been predicted; the removal of surfactant molecules and the supply of energy in the form of heat are both known to encourage nanoparticles to sinter and agglomerate. However, of interest was the role that these treatment steps played in determining the catalytic activity of the product particles.

The particles described were tested to determine their utility as ORR catalysts, and benchmarked against commercial standard catalyst materials. These experiments showed that a number of the particles prepared, and in particular those that had been acid and heat treated, had the potential to deliver enhanced catalysis, relative to the commercial standards. The best performing catalyst studied, the RuSePt Low material heat treated at 250 °C, had a measured mass activity more than four times higher than the Pt/C standard used. This activity improvement likely arises due to a complex combination of factors. Firstly, in line with the theoretical context set out, it is likely that within the alloy nanoparticles, the Ru atoms tweak the electronic character of the Pt atoms such as to lower their overall affinity towards the reactant oxygen molecules, facilitating enhanced catalysis. Further, the heat treatment protocol described was anticipated to optimise those parameters by improving the chemical ordering within the alloy, while also removing surfactant molecules which may have been obscuring catalyst active sites in the as prepared materials. These findings have several implications in terms of their validation of the theoretical concept for the nanoparticle design, and indeed the verification of the utility and value of the post-synthesis treatments described. The RuSePt system warrants further study as a candidate catalyst material, and the investigation of acid and/or heat treatment protocols for colloidally prepared nanoparticle catalyst materials is recommended.

5.2 Recommendations for Further Work

Three main areas remain outstanding following the work described, and would benefit from further investigation. The first refers to the need to improve understanding of the mechanistic aspects of the shape control described for the nanoparticle systems explored. Subsequently, given the utility of the acid and heat treatment protocols discussed, further study is indicated in elaborating on the chemical and physical impacts of their use, in order to ensure future reproducibility of the effects noted. Finally, the candidate catalyst materials should be evaluated in actual fuel cells, to verify the degree to which the activity enhancements envisaged could translate to the operational fuel cell environment. These measurements should be accompanied by ex- and in-situ durability testing, to ascertain the degree to which the measured activities are sustainable over the operational life of a catalyst. These areas are discussed in more detail below.

Given the conclusions described regarding the influencing factors determining the shape of the product particles in the systems under study, further work to understand the mechanistic underpinnings driving these phenomena would undoubtedly be very insightful. In-situ synchrotron X-ray studies [98, 146, 168] have been used to great effect to follow the dynamics of nanoparticle synthesis reactions as they progress, in order to observe the emergence of given lattice planes and facets. More recently, liquid phase TEM experiments have also been reported, in which nanoparticle growth processes can be followed in real time [169]. The challenges associated with such experiments are clear, and these measurements require specialised equipment and expertise. However, this insight would prove invaluable in better understanding how and why the nanoparticles studied in this work formed in such different morphologies and dispersions.

In a situation in which resources and instrument availability were infinite, it would also have been extremely useful to have conducted STEM-EELS experiments on all of the nanoparticle systems described in the preceding chapters. Discussion on the impacts of the heat and acid treatment protocols on the nanoparticle surfaces would have been aided immeasurably by being able to visualise the changes realised in the configuration, alignment and segregation behaviour of the elements contained within the particles, and indeed on the eventual fate of the Se atoms in the relevant cases. The SuperSTEM time used to carry out the STEM-EELS experiments described in this work was secured via competitive application, and strictly limited. In an idealised case, the opportunity to conduct further STEM-EELS experiments would have been very constructive to elucidating the phenomena underpinning the electrochemical characteristics subsequently identified for the nanoparticles.

In terms of their electrochemistry, wholesale enhancements in catalytic activity were observed for many of the nanoparticle systems described, particularly in the acid and heat treated cases, relative to commercial Pt/C and PtRu/C standards. These enhancements show promise, and a key conclusion from this work is recognising that further investigation of the merits of these systems is warranted. The first aspect worth exploring further is the durability of the catalysts described, and both ex- and in-situ accelerated stress testing protocols should be developed to measure the degree to which the catalysts maintain the measured activities through prolonged cycling. A recent paper noted the significant challenges associated with benchmarking ORR catalysts, given the dizzying array of reports in the literature, with Pt-based alloy catalyst mass activities reported within the huge range of 230-6980 mA per mg Pt [170]. Issues in standardising electrochemical testing have also already been discussed [157, 158, 160], with key issues arising due to the significant variations in electrochemical testing practices, conditions and environments between laboratories. With this in mind, an approach towards improved benchmarking of catalyst activities is in translating the testing regime to in-situ testing, in conditions better representing an actual fuel cell electrode working environment [171]. Such in-situ testing of catalysts is routine, though typically indicated only for those catalysts with promising ex-situ test results. In-situ testing requires specialist fuel cell test stand equipment and expertise, and was beyond the scope of this current work. This would be a natural next step, however, to better ascertain the real world potential of the catalysts prepared.

6 References

[1] British Petroleum. *Energy Outlook 2019*; London, 2019.

[2] Mackay, D. J. *Sustainable Energy — Without the Hot Air*, 1st ed.; UIT Cambridge Ltd: Cambridge, 2009. https://doi.org/10.1119/1.3246485.

[3] United Nations Framework Convention; on Climate Change. *Paris Agreement*; 2015. https://doi.org/FCCC/CP/2015/L.9.

[4] IRENA. *Global Energy Transformation: A Roadmap to 2050*; Abu Dhabi, 2018. https://doi.org/10.4324/9780429320071-4.

[5] European Commission. Renewable Energy Statistics https://ec.europa.eu/eurostat/statistics-explained/index.php/Renewable_energy_statistics#Renewable_energy_produced_in_the_EU_increased_by_two_thirds_in_2007-2017 (accessed Jan 14, 2020).

[6] The Scottish Government. *Annual Energy Statement 2019*; Edinburgh, 2019.

[7] Department for Business Energy and Industrial Strategy. *Digest of United Kingdom Energy Statistics 2019*; London, 2019.

[8] Committee on Climate Change. *Net Zero: The UK's Contribution to Stopping Global Warming*; London, 2019.

[9] Department for Business Energy and Industrial Strategy. UK becomes first major economy to pass net zero emissions law.

[10] Scottish Government. Scotland to become a net-zero society

https://www.gov.scot/news/scotland-to-become-a-net-zero-society/ (accessed Jan 16, 2020).

[11] United Nations Framework Convention on Climate Change. Climate Ambition Alliance: Nations Renew their Push to Upscale Action by 2020 and Achieve Net Zero CO2 Emissions by 2050 https://cop25.cl/#/cop-news/RAAeacl2BQcY5P3Tze4w (accessed Jan 11, 2020).

[12] Boulby, G. *The Future of Heat in the UK: The UK's Vision for Heat Networks*; 2015.

[13] Bloomberg New Energy Finance. *Electric Vehicle Outlook 2019*; London, 2018.

[14] Committee on Climate Change. *Hydrogen in a Low Carbon Economy*; 2018.

[15] World Energy Council. *Power-to-X Roadmap*; 2018.

[16] Hy4Heat. *Hy4Heat Progress Report*; 2019.

[17] Cadent. *HyNet North West*; 2018.

[18] Isaac, T. HyDeploy: The UK's First Hydrogen Blending Deployment Project. *Clean Energy*, **2019**, *3* (2), 114–125. https://doi.org/10.1093/ce/zkz006.

[19] E4tech. *Scenarios for Deployment of Hydrogen in Contributing to Meeting Carbon Budgets and the 2050 Target*; London, 2015.

[20] Toyota. Toyota Mirai: The Future has Arrived https://blog.toyota.co.uk/toyota-mirai-the-future-has-arrived (accessed Apr

2, 2019).

[21] Hydrogen Mobility Europe. *Emerging Conclusions from H2ME*; 2018.

[22] National Energy Technology Laboratory. *Fuel Cell Handbook*; Morgantown, West Virginina, 2004.

[23] Fuel Cell Technologies Office. *Comparison of Fuel Cell Technologies*; 2014.

[24] International Organization for Standardization. ISO/TS 80004-2:2015.

[25] De Jong, W. H.; Borm, P. J. a. Drug Delivery and Nanoparticles: Applications and Hazards. *Int. J. Nanomedicine*, **2008**, *3* (2), 133–149. https://doi.org/10.2147/IJN.S596.

[26] Calavia, R.; Ionescu, R.; Cindemir, U.; Topalian, Z.; Llobet, E.; Granqvist, C.-G.; Welearegay, T. G.; Haddi, Z. Fabrication of Ultra-Pure Gold Nanoparticles Capped with Dodecanethiol for Schottky-Diode Chemical Gas Sensing Devices. *Sensors Actuators B Chem.*, **2016**, *239*, 455–461. https://doi.org/10.1016/j.snb.2016.07.182.

[27] Stieberova, B.; Zilka, M.; Ticha, M.; Freiberg, F.; Caramazana-González, P.; McKechnie, J.; Lester, E. Application of ZnO Nanoparticles in a Self-Cleaning Coating on a Metal Panel: An Assessment of Environmental Benefits. *ACS Sustain. Chem. Eng.*, **2017**, *5* (3), 2493–2500. https://doi.org/10.1021/acssuschemeng.6b02848.

[28] Chorkendorff, I.; Dickens, C. F.; Seh, Z. W.; Kibsgaard, J.; Jaramillo, T. F.; Nørskov, J. K. Combining Theory and Experiment in Electrocatalysis: Insights into Materials Design. *Science (80-.).*, **2017**, *355* (6321),

eaad4998. https://doi.org/10.1126/science.aad4998.

[29] Markovic, N. M.; Ross Jr., P. N. Surface Science Studies of Model Fuel Cell Electrocatalysts. *Surf. Sci. Rep.*, **2002**, *45* (4–6), 117–229. https://doi.org/10.1016/S0167-5729(01)00022-X.

[30] Rabis, A.; Rodriguez, P.; Schmidt, T. J. Electrocatalysis for Polymer Electrolyte Fuel Cells: Recent Achievements and Future Challenges. *ACS Catal.*, **2012**, *2* (5), 864–890. https://doi.org/10.1021/cs3000864.

[31] Wang, M.; Wang, X.; Chen, M.; Yang, Z.; Dong, C. Nanostructured Electrocatalytic Materials and Porous Electrodes for Direct Methanol Fuel Cells. *Cuihua Xuebao/Chinese J. Catal.*, **2016**, *37* (7), 1037–1048. https://doi.org/10.1016/S1872-2067(16)62477-4.

[32] Vignarooban, K.; Lin, J.; Arvay, A.; Kolli, S.; Kruusenberg, I.; Tammeveski, K.; Munukutla, L.; Kannan, A. M. Nano-Electrocatalyst Materials for Low Temperature Fuel Cells: A Review. *Cuihua Xuebao/Chinese J. Catal.*, **2015**, *36* (4), 458–472. https://doi.org/10.1016/S1872-2067(14)60175-3.

[33] Johnson Matthey Precious Metals Management. *Price Charts - Platinum Group Metals*; Royston, Hertfordshire, 2016.

[34] Martin, S.; Garcia-Ybarra, P. L.; Castillo, J. L. High Platinum Utilization in Ultra-Low Pt Loaded PEM Fuel Cell Cathodes Prepared by Electrospraying. *Int. J. Hydrogen Energy*, **2010**, *35* (19), 10446–10451. https://doi.org/10.1016/j.ijhydene.2010.07.069.

[35] Fabbri, E.; Taylor, S.; Rabis, A.; Levecque, P.; Conrad, O.; Kötz, R.; Schmidt, T. J. The Effect of Platinum Nanoparticle Distribution on Oxygen

Electroreduction Activity and Selectivity. *ChemCatChem*, **2014**, *6* (5), 1410–1418. https://doi.org/10.1002/cctc.201300987.

[36] Debe, M. K. Electrocatalyst Approaches and Challenges for Automotive Fuel Cells. *Nature*, **2012**, *486* (7401), 43–51. https://doi.org/10.1038/nature11115.

[37] Shao, M.; Chang, Q.; Dodelet, J. P.; Chenitz, R. Recent Advances in Electrocatalysts for Oxygen Reduction Reaction. *Chem. Rev.*, **2016**, *116* (6), 3594–3657. https://doi.org/10.1021/acs.chemrev.5b00462.

[38] Hwang, S. J.; Yoo, S. J.; Shin, J.; Cho, Y.-H.; Jang, J. H.; Cho, E.; Sung, Y.-E.; Nam, S. W.; Lim, T.-H.; Lee, S.-C.; et al. Supported Core@shell Electrocatalysts for Fuel Cells: Close Encounter with Reality. *Sci. Rep.*, **2013**, *3* (MI), 1309. https://doi.org/10.1038/srep01309.

[39] Brankovic, S. R.; Wang, J. X.; Adžić, R. R. Metal Monolayer Deposition by Replacement of Metal Adlayers on Electrode Surfaces. *Surf. Sci.*, **2001**, *474* (1–3). https://doi.org/10.1016/S0039-6028(00)01103-1.

[40] Zhang, J.; Mo, Y.; Vukmirovic, M. B.; Klie, R.; Sasaki, K.; Adzic, R. R. Platinum Monolayer Electrocatalysts for O2 Reduction: Pt Monolayer on Pd(111) and on Carbon-Supported Pd Nanoparticles. *J. Phys. Chem. B*, **2004**, *108* (30), 10955–10964. https://doi.org/10.1021/jp0379953.

[41] Zhang, J.; Lima, F. H. B.; Shao, M. H.; Sasaki, K.; Wang, J. X.; Hanson, J.; Adzic, R. R. Platinum Monolayer on Nonnoble Metal-Noble Metal Core-Shell Nanoparticle Electrocatalysts for O2 Reduction. *J. Phys. Chem. B*, **2005**, *109* (48), 22701–22704. https://doi.org/10.1021/jp055634c.

[42] Xu, Y.; Mavrikakis, M.; Vukmirovic, M. B.; Adzic, R. R.; Zhang, J. Controlling the Catalytic Activity of Platinum-Monolayer Electrocatalysts for Oxygen Reduction with Different Substrates. *Angew. Chemie Int. Ed.*, **2005**, *44* (14), 2132–2135. https://doi.org/10.1002/anie.200462335.

[43] Chorkendorff, I.; Malacrida, P.; Stephens, I. E. L.; Verdaguer-Casadevall, A.; Escudero-Escribano, M. Enhanced Activity and Stability of Pt–La and Pt–Ce Alloys for Oxygen Electroreduction: The Elucidation of the Active Surface Phase. *J. Mater. Chem. A*, **2014**, *2* (12), 4234. https://doi.org/10.1039/c3ta14574c.

[44] Greeley, J.; Stephens, I. E. L.; Bondarenko, A. S.; Johansson, T. P.; Hansen, H. A.; Jaramillo, T. F.; Rossmeisl, J.; Chorkendorff, I.; Nørskov, J. K. Alloys of Platinum and Early Transition Metals as Oxygen Reduction Electrocatalysts. *Nat. Chem.*, **2009**, *1* (7), 552–556. https://doi.org/10.1038/nchem.367.

[45] Jennings, P. C.; Pollet, B. G.; Johnston, R. L. Theoretical Studies of Pt-Ti Nanoparticles for Potential Use as PEMFC Electrocatalysts. *Phys. Chem. Chem. Phys.*, **2012**, *14* (9), 3134–3139. https://doi.org/10.1039/c2cp23430k.

[46] Wang, P.; Tooriyama, H.; Yokoyama, K.; Ohtani, M.; Asahara, H.; Konishi, T.; Nishiwaki, N.; Shimoda, M.; Yamashita, Y.; Yoshikawa, H.; et al. Smart Decoration of Mesoporous TiO2 Nanospheres with Noble Metal Alloy Nanoparticles into Core-Shell, Yolk-Core-Shell, and Surface-Dispersion Morphologies. *Eur. J. Inorg. Chem.*, **2014**, *2014* (26), 4254–4257.

https://doi.org/10.1002/ejic.201402646.

[47] Blackmore, C. E.; Rees, N. V; Palmer, R. E. Modular Construction of Size-Selected Multiple-Core Pt-TiO2 Nanoclusters for Electro-Catalysis. *Phys. Chem. Chem. Phys.* , **2015**, *17*, 28005–28009. https://doi.org/10.1039/c5cp00285k.

[48] Gupta, G.; Iqbal, P.; Yin, F.; Liu, J.; Palmer, R. E.; Sharma, S.; Leung, K. C. F.; Mendes, P. M. Pt Diffusion Dynamics for the Formation Cr-Pt Core-Shell Nanoparticles. *Langmuir*, **2015**, *31* (24), 6917–6923. https://doi.org/10.1021/acs.langmuir.5b01410.

[49] Gupta, G.; Sharma, S.; Mendes, P. M. Nafion-Stabilised Bimetallic Pt–Cr Nanoparticles as Electrocatalysts for Proton Exchange Membrane Fuel Cells (PEMFCs). *RSC Adv.*, **2016**, *6* (86), 82635–82643. https://doi.org/10.1039/C6RA16025E.

[50] Zhu, H.; Li, X.; Wang, F. Synthesis and Characterization of Cu@Pt/C Core-Shell Structured Catalysts for Proton Exchange Membrane Fuel Cell. *Int. J. Hydrogen Energy*, **2011**, *36* (15), 9151–9154. https://doi.org/10.1016/j.ijhydene.2011.04.224.

[51] Guterman, V. E.; Belenov, S. V.; Pakharev, A. Y.; Min, M.; Tabachkova, N. Y.; Mikheykina, E. B.; Vysochina, L. L.; Lastovina, T. a. Pt-M/C (M=Cu, Ag) Electrocatalysts with an Inhomogeneous Distribution of Metals in the Nanoparticles. *Int. J. Hydrogen Energy*, **2016**, *41* (3), 1609–1626. https://doi.org/10.1016/j.ijhydene.2015.11.002.

[52] Antolini, E. Iron-Containing Platinum-Based Catalysts as Cathode and

Anode Materials for Low-Temperature Acidic Fuel Cells: A Review. *RSC Adv.*, **2016**, *6* (4), 3307–3325. https://doi.org/10.1039/c5ra22035a.

[53] Jang, J. H.; Lee, E.; Park, J.; Kim, G.; Hong, S.; Kwon, Y. U. Rational Syntheses of Core-Shell Fe x @Pt Nanoparticles for the Study of Electrocatalytic Oxygen Reduction Reaction. *Sci. Rep.*, **2013**, *3*, 1–8. https://doi.org/10.1038/srep02872.

[54] Yu, Y.; DiSalvo, F. J.; Wang, D.; Wang, H.; Hovden, R.; Xin, H. L.; Abruña, H. D.; Muller, D. A. Structurally Ordered Intermetallic Platinum–Cobalt Core–Shell Nanoparticles with Enhanced Activity and Stability as Oxygen Reduction Electrocatalysts. *Nat. Mater.*, **2012**, *12* (1), 81–87. https://doi.org/10.1038/nmat3458.

[55] Chen, Y.; Liang, Z.; Yang, F.; Liu, Y.; Chen, S. Ni-Pt Core-Shell Nanoparticles as Oxygen Reduction Electrocatalysts: Effect of Pt Shell Coverage. *J. Phys. Chem. C*, **2011**, *115* (49), 24073–24079. https://doi.org/10.1021/jp207828n.

[56] Strasser, P.; Kühl, S. Dealloyed Pt-Based Core-Shell Oxygen Reduction Electrocatalysts. *Nano Energy*, **2016**, *29*, 166–177. https://doi.org/10.1016/j.nanoen.2016.04.047.

[57] Gan, L.; Heggen, M.; Rudi, S.; Strasser, P. Core−Shell Compositional Fine Structures of Dealloyed Pt. *Nano Lett.*, **2012**, *12*, 5423–5430. https://doi.org/10.1021/nl302995z.

[58] Gan, L.; Cui, C.; Rudi, S.; Strasser, P. Core-Shell and Nanoporous Particle Architectures and Their Effect on the Activity and Stability of Pt ORR

Electrocatalysts. *Top. Catal.*, **2014**, *57* (1–4), 236–244. https://doi.org/10.1007/s11244-013-0178-z.

[59] Li, M.; Lei, Y.; Sheng, N.; Ohtsuka, T. Preparation of Low-Platinum-Content Platinum-Nickel, Platinum-Cobalt Binary Alloy and Platinum-Nickel-Cobalt Ternary Alloy Catalysts for Oxygen Reduction Reaction in Polymer Electrolyte Fuel Cells. *J. Power Sources*, **2015**, *294*, 420–429. https://doi.org/10.1016/j.jpowsour.2015.06.084.

[60] Jennings, P. C. Computational Studies of Mono- and Bimetallic Nanoclusters for Potential Polymer Electrolyte Fuel Cell Applications, Thesis, University of Birmingham, 2014.

[61] Ogasawara, H.; Yu, C.; Liu, Z.; Koh, S.; Strasser, P.; Kaya, S.; Toney, M. F.; Greeley, J.; Anniyev, T.; Nilsson, A.; et al. Lattice-Strain Control of the Activity in Dealloyed Core–Shell Fuel Cell Catalysts. *Nat. Chem.*, **2010**, *2* (6), 454–460. https://doi.org/10.1038/nchem.623.

[62] Fusy, J.; Menaucourt, J.; Alnot, M.; Huguet, C.; Ehrhardt, J. J. Growth and Reactivity of Evaporated Platinum Films on Cu(111): A Study by AES, RHEED and Adsorption of Carbon Monoxide and Xenon. *Appl. Surf. Sci.*, **1996**, *93* (3), 211–220. https://doi.org/10.1016/0169-4332(95)00340-1.

[63] Jennings, P. C.; Aleksandrov, H. A.; Neyman, K. M.; Johnston, R. L. Oxygen Dissociation on M@Pt Core-Shell Particles for 3d, 4d, and 5d Transition Metals. *J. Phys. Chem. C*, **2015**, *119* (20), 11031–11041. https://doi.org/10.1021/jp511598e.

[64] Lu, Y.; Du, S.; Steinberger-Wilckens, R. Three-Dimensional Catalyst

Electrodes Based on PtPd Nanodendrites for Oxygen Reduction Reaction in PEFC Applications. *Appl. Catal. B Environ.*, **2016**, *187* (March), 108–114. https://doi.org/10.1016/j.apcatb.2016.01.019.

[65] Qi, K.; Zheng, W.; Cui, X. Supersaturation-Controlled Surface Structure Evolution of Pd@Pt Core-Shell Nanocrystals: Enhancement of the ORR Activity at a Sub-10 Nm Scale. *Nanoscale*, **2016**, *8* (3), 1698–1703. https://doi.org/10.1039/c5nr07940c.

[66] Karan, H. I.; Sasaki, K.; Kuttiyiel, K.; Farberow, C. a.; Mavrikakis, M.; Adzic, R. R. Catalytic Activity of Platinum Monolayer on Iridium and Rhenium Alloy Nanoparticles for the Oxygen Reduction Reaction. *ACS Catal.*, **2012**, *2* (5), 817–824. https://doi.org/10.1021/cs200592x.

[67] Hsieh, Y. C.; Zhang, Y.; Su, D.; Volkov, V.; Si, R.; Wu, L.; Zhu, Y.; An, W.; Liu, P.; He, P.; et al. Ordered Bilayer Ruthenium-Platinum Core-Shell Nanoparticles as Carbon Monoxide-Tolerant Fuel Cell Catalysts. *Nat. Commun.*, **2013**, *4* (August 2015), 1–9. https://doi.org/10.1038/ncomms3466.

[68] Caballero-Manrique, G.; Velazquez-Palenzuela, A.; Brillas, E.; Centellas, F.; Garrido, J. A.; Rodriguez, R. M.; Cabot, P. L. Electrochemical Synthesis and Characterization of Carbon-Supported Pt and Pt-Ru Nanoparticles with Cu Cores for CO and Methanol Oxidation in Polymer Electrolyte Fuel Cells. *Int. J. Hydrogen Energy*, **2014**, *39* (24), 12859–12869. https://doi.org/10.1016/j.ijhydene.2014.06.089.

[69] Caballero-Manrique, G.; Brillas, E.; Centellas, F.; Garrido, J.; Rodríguez,

R.; Cabot, P.-L. Electrochemical Oxidation of the Carbon Support to Synthesize Pt(Cu) and Pt-Ru(Cu) Core-Shell Electrocatalysts for Low-Temperature Fuel Cells. *Catalysts*, **2015**, *5* (2), 815–837. https://doi.org/10.3390/catal5020815.

[70] Wang, X.; Zhu, Y.; Vasileff, A.; Jiao, Y.; Chen, S.; Song, L.; Zheng, B.; Zheng, Y.; Qiao, S.-Z. Strain Effect in Bimetallic Electrocatalysts in the Hydrogen Evolution Reaction. *ACS Energy Lett.*, **2018**, *3* (31), 1198–1204. https://doi.org/10.1021/acsenergylett.8b00454.

[71] Yang, L.; Vukmirovic, M. B.; Su, D.; Sasaki, K.; Herron, J. A.; Mavrikakis, M.; Liao, S.; Adzic, R. R. Tuning the Catalytic Activity of Ru@Pt Core-Shell Nanoparticles for the Oxygen Reduction Reaction by Varying the Shell Thickness. *J. Phys. Chem. C*, **2013**, *117*, 1748–1753.

[72] Kaplan, D.; Goor, M.; Alon, M.; Tsizin, S.; Burstein, L.; Rosenberg, Y.; Popov, I.; Peled, E. Comparison of Iridium- and Ruthenium-Based, Pt-Surface-Enriched, Nanosize Catalysts for the Oxygen-Reduction Reaction. *J. Power Sources*, **2016**, *306*, 219–225. https://doi.org/10.1016/j.jpowsour.2015.12.017.

[73] Jackson, A.; Strickler, A.; Higgins, D.; Jaramillo, T. Engineering Ru@Pt Core-Shell Catalysts for Enhanced Electrochemical Oxygen Reduction Mass Activity and Stability. *Nanomaterials*, **2018**, *8* (1), 38. https://doi.org/10.3390/nano8010038.

[74] Adzic, R. R.; Kuttiyiel, K. A.; Su, D.; Liu, P.; Park, G.-G.; Choi, Y.; Yang, T.-H.; Sasaki, K.; Hwang, S.-M. Enhancement of the Oxygen Reduction on

Nitride Stabilized Pt-M (M=Fe, Co, and Ni) Core–Shell Nanoparticle Electrocatalysts. *Nano Energy*, **2015**, *13*, 442–449. https://doi.org/10.1016/j.nanoen.2015.03.007.

[75] Delacôte, C.; Lewera, A.; Pisarek, M.; Kulesza, P. J.; Zelenay, P.; Alonso-Vante, N. The Effect of Diluting Ruthenium by Iron in RuxSey Catalyst for Oxygen Reduction. *Electrochim. Acta*, **2010**, *55* (26), 7575–7580. https://doi.org/10.1016/j.electacta.2010.01.029.

[76] Miecznikowski, K.; Kulesza, P. J.; Fiechter, S. Application of Black Pearl Carbon-Supported WO3 Nanostructures as Hybrid Carriers for Electrocatalytic RuSex Nanoparticles. *Appl. Surf. Sci.*, **2011**, *257* (19), 8215–8222. https://doi.org/10.1016/j.apsusc.2011.03.119.

[77] Chen, S.; Gasteiger, H. A.; Hayakawa, K.; Tada, T.; Shao-Horn, Y. Platinum-Alloy Cathode Catalyst Degradation in Proton Exchange Membrane Fuel Cells: Nanometer-Scale Compositional and Morphological Changes. *J. Electrochem. Soc.*, **2010**, *157* (1), A82. https://doi.org/10.1149/1.3258275.

[78] Jiang, K.; Zhao, D.; Guo, S.; Zhang, X.; Zhu, X.; Guo, J. Efficient Oxygen Reduction Catalysis by Subnanometer Pt Alloy Nanowires. *Sci. Adv.*, **2017**, No. February, 2–9. https://doi.org/10.1126/sciadv.1601705.

[79] Niu, Z.; Becknell, N.; Yu, Y.; Kim, D.; Chen, C.; Kornienko, N.; Somorjai, G. A.; Yang, P. Anisotropic Phase Segregation and Migration of Pt in Nanocrystals En Route to Nanoframe Catalysts. *Nat. Mater.*, **2016**, *1* (August), 1–21. https://doi.org/10.1038/nmat4724.

[80] Larsen, A. H.; Jackson, A.; Viswanathan, V.; Jaramillo, T. F.; Nørskov, J. K.; Forman, A. J. Climbing the Activity Volcano: Core-Shell Ru@Pt Electrocatalysts for Oxygen Reduction. *ChemElectroChem*, **2013**, *1* (1), 67–71. https://doi.org/10.1002/celc.201300117.

[81] Papageorgopoulos, D. C.; Liu, F.; Conrad, O. A Study of RhxSy/C and RuSex/C as Methanol-Tolerant Oxygen Reduction Catalysts for Mixed-Reactant Fuel Cell Applications. *Electrochim. Acta*, **2007**, *53* (2), 1037–1041. https://doi.org/10.1016/j.electacta.2007.09.037.

[82] Zehl, G.; Schmithals, G.; Hoell, A.; Haas, S.; Hartnig, C.; Dorbandt, I.; Bogdanoff, P.; Fiechter, S. On the Structure of Carbon-Supported Selenium-Modified Ruthenium Nanoparticles as Electrocatalysts for Oxygen Reduction in Fuel Cells. *Angew. Chemie - Int. Ed.*, **2007**, *46* (38), 7311–7314. https://doi.org/10.1002/anie.200701473.

[83] Cao, D.; Wieckowski, A.; Inukai, J.; Alonso-Vante, N. Oxygen Reduction Reaction on Ruthenium and Rhodium Nanoparticles Modified with Selenium and Sulfur. *J. Electrochem. Soc.*, **2006**, *153* (5), A869. https://doi.org/10.1149/1.2180709.

[84] Nagabhushana, K. S.; Dinjus, E.; Bönnemann, H.; Zaikovskii, V.; Hartnig, C.; Zehl, G.; Dorbandt, I.; Fiechter, S.; Bogdanoff, P. Reductive Annealing for Generating Se Doped 20 Wt% Ru/C Cathode Catalysts for the Oxygen Reduction Reaction. *J. Appl. Electrochem.*, **2007**, *37* (12), 1515–1522. https://doi.org/10.1007/s10800-007-9423-0.

[85] Jiang, X.; Gür, T. M.; Prinz, F. B.; Bent, S. F. Atomic Layer Deposition

(ALD) Co-Deposited Pt-Ru Binary and Pt Skin Catalysts for Concentrated Methanol Oxidation. *Chem. Mater.*, **2010**, *22* (10), 3024–3032. https://doi.org/10.1021/cm902904u.

[86] Belloni, J. Metal Nanocolloids. *Curr. Opin. Colloid Interface Sci.*, **1996**, *1*, 184–196. https://doi.org/10.1016/s1359-0294(96)80003-3.

[87] Michael Faraday; Faraday, M. Experimental Relations of Gold (and Other Metals) to Light. *Phil. Trans. R. Soc.*, **1857**, *147* (0), 145–181. https://doi.org/10.1098/rstl.1857.0011.

[88] Serpell, C. J.; Cookson, J.; Ozkaya, D.; Beer, P. D. Core@shell Bimetallic Nanoparticle Synthesis via Anion Coordination. *Nat. Chem.*, **2011**, *3* (6), 478–483. https://doi.org/10.1038/nchem.1030.

[89] Chen, Y.; Yang, F.; Dai, Y.; Wang, W.; Chen, S. Ni@Pt Core-Shell Nanoparticles: Synthesis, Structural and Electrochemical Properties. *J. Phys. Chem. C*, **2008**, *112* (5), 1645–1649. https://doi.org/10.1021/jp709886y.

[90] Wang, L.; Shen, M.; Wang, X.; Zheng, H.; Zhang, G. Green Synthesis and Characterization of Au@Pt Core–Shell Bimetallic Nanoparticles Using Gallic Acid. *J. Phys. Chem. Solids*, **2014**, *81*, 79–87. https://doi.org/10.1016/j.jpcs.2014.12.012.

[91] Lee, E.; Jang, J. H.; Matin, M. A.; Kwon, Y. U. One-Step Sonochemical Syntheses of Ni@Pt Core-Shell Nanoparticles with Controlled Shape and Shell Thickness for Fuel Cell Electrocatalyst. *Ultrason. Sonochem.*, **2014**, *21* (1), 317–323. https://doi.org/10.1016/j.ultsonch.2013.05.006.

[92] Liu, G.; Zhang, H.; Hu, J. Novel Synthesis of a Highly Active Carbon-Supported Ru85Se15 Chalcogenide Catalyst for the Oxygen Reduction Reaction. *Electrochem. commun.*, **2007**, *9* (11), 2643–2648. https://doi.org/10.1016/j.elecom.2007.08.018.

[93] Bernard, A.; Zhang, K.; Larson, D.; Tabatabaei, K.; Kauzlarich, S. M. Solvent Effects on Growth, Crystallinity, and Surface Bonding of Ge Nanoparticles. *Inorg. Chem.*, **2018**, *57* (9), 5299–5306. https://doi.org/10.1021/acs.inorgchem.8b00334.

[94] Xia, Y.; Xiong, Y.; Lim, B.; Skrabalak, S. E. Shape-Controlled Synthesis of Metal Nanocrystals: Simple Chemistry Meets Complex Physics? *Angew. Chemie - Int. Ed.*, **2009**, *48* (1), 60–103. https://doi.org/10.1002/anie.200802248.

[95] LaMer, V. K.; Dinegar, R. H. Theory, Production and Mechanism of Formation of Monodispersed Hydrosols. *J. Am. Chem. Soc.*, **1950**, *72* (11), 4847–4854. https://doi.org/10.1016/s0033-3506(55)80003-0.

[96] Moussa, S.; Abdelsayed, V.; El Shall, M. S. Chemical Synthesis of Metal Nanoparticles and Nanoalloys. In *Nanoalloys: From Fundamentals to Emergent Applications*; Elsevier B.V: Amsterdam, 2013; pp 1–37. https://doi.org/10.1016/b978-0-12-394401-6.00001-1.

[97] Newton, J. E.; Preece, J. A.; Pollet, B. G. Control of Nanoparticle Aggregation in PEMFCs Using Surfactants. *Int. J. Low-Carbon Technol.*, **2012**, *7* (1), 38–43. https://doi.org/10.1093/ijlct/ctr023.

[98] Boita, J.; Nicolao, L.; Alves, M. C. M.; Morais, J. Observing Pt Nanoparticle

Formation at the Atomic Level during Polyol Synthesis. *Phys. Chem. Chem. Phys.*, **2014**, *16* (33), 17640–17647. https://doi.org/10.1039/c4cp01925c.

[99] Abécassis, B.; Testard, F.; Spalla, O.; Barboux, P. Probing in Situ the Nucleation and Growth of Gold Nanoparticles by Small-Angle X-Ray Scattering. *Nano Lett.*, **2007**, *7* (6), 1723–1727. https://doi.org/10.1021/nl0707149.

[100] Mi, J. L.; Nørby, P.; Bremholm, M.; Becker, J.; Iversen, B. B. The Formation Mechanism of Bimetallic PtRu Alloy Nanoparticles in Solvothermal Synthesis. *Nanoscale*, **2015**, *7* (39), 16170–16174. https://doi.org/10.1039/c5nr04459f.

[101] Mejía-Rosales, S.; Ponce, A.; José–Yacamán, M. Experimental Techniques for Structural Characterization. In *Nanoalloys: From Fundamentals to Emergent Applications*; Elsevier B.V: Amsterdam, 2013; pp 113–145. https://doi.org/10.1016/b978-0-12-394401-6.00004-7.

[102] De Graef, M. The Transmission Electron Microscope. In *Introduction to Conventional Transmission Electron Microscopy*; Cambridge University Press: Cambridge, 2009; pp 136–234. https://doi.org/10.1017/cbo9780511615092.005.

[103] Smith, D. J. Characterization of Nanomaterials with Transmission Electron Microscopy. In *Nanocharacterisation*; Kirkland, A. I., Haigh, S. J., Eds.; Royal Society of CHemistry: Cambridge, 2015; pp 1–29. https://doi.org/10.1088/1757-899X/146/1/012001.

[104] Baer, D. R.; Gaspar, D. J.; Nachimuthu, P.; Techane, S. D.; Castner, D. G. Application of Surface Chemical Analysis Tools for Characterization of Nanoparticles. *Anal. Bioanal. Chem.*, **2010**, *396* (3), 983–1002. https://doi.org/10.1007/s00216-009-3360-1.

[105] Lee, H.-L.; Flynn, N. T. X-Ray Photoelectron Spectroscopy. In *Handbook of Applied Solid State Spectroscopy*; Springer: Boston, 2006; pp 485–507.

[106] Mourdikoudis, S.; Pallares, R. M.; Thanh, N. T. K. Characterization Techniques for Nanoparticles: Comparison and Complementarity upon Studying Nanoparticle Properties. *Nanoscale*, **2018**, *10* (27), 12871–12934. https://doi.org/10.1039/c8nr02278j.

[107] Moulder, J. F.; Stickle, W. F.; Sobol, P. E.; Bomben, K. D. *Handbook of X-Ray Photoelectron Spectroscopy*; Chastain, J., Ed.; Perkin-Elmer Corporation: Eden Prairie, 1992.

[108] Morrell, T. E.; Karagounis, T. K.; Wang, C.-Y.; Hsia, C.-H.; Landry, M. L. Simple Syntheses of CdSe Quantum Dots. *J. Chem. Educ.*, **2013**, *91* (2), 274–279. https://doi.org/10.1021/ed300568e.

[109] Yang, J.; Chen, X.; Ye, F.; Wang, C.; Zheng, Y.; Yang, J. Core-Shell CdSe@Pt Nanocomposites with Superior Electrocatalytic Activity Enhanced by Lateral Strain Effect. *J. Mater. Chem.*, **2011**, *21* (25), 9088–9094. https://doi.org/10.1039/c1jm11006c.

[110] Curnick, O. Ionomer-Stabilised Pt and Pt-Ti Bimetallic Electrocatalysts for the Proton Exchange Membrane Fuel Cell, University of Birmingham, 2012.

[111] Pons, M. N.; Vivier, H.; Delcour, V.; Authelin, J. R.; Paillères-Hubert, L.

Morphological Analysis of Pharmaceutical Powders. *Powder Technol.*, **2002**, *128* (2–3), 276–286. https://doi.org/10.1016/S0032-5910(02)00177-8.

[112] Surana, K.; Singh, P. K.; Rhee, H. W.; Bhattacharya, B. Synthesis, Characterization and Application of CdSe Quantum Dots. *J. Ind. Eng. Chem.*, **2014**, *20* (6), 4188–4193. https://doi.org/10.1016/j.jiec.2014.01.019.

[113] Bajwa, N.; Mehra, N. K.; Jain, K.; Jain, N. K. Pharmaceutical and Biomedical Applications of Quantum Dots. *Artif. Cells, Nanomedicine Biotechnol.*, **2016**, *44* (3), 758–768. https://doi.org/10.3109/21691401.2015.1052468.

[114] AbouElhamd, A. R.; Al-Sallal, K. A.; Hassan, A. Review of Core/Shell Quantum Dots Technology Integrated into Building's Glazing. *Energies*, **2019**, *12* (6). https://doi.org/10.3390/en12061058.

[115] Cao, D.; Babu, P. K.; Zelenay, P.; Garzon, F.; Johnston, C. M.; Choi, J.-H. Se-Modified Ru Nanoparticles as ORR Catalysts – Part 1: Synthesis and Analysis by RRDE and in PEFCs. *J. Electroanal. Chem.*, **2011**, *662* (1), 257–266. https://doi.org/10.1016/j.jelechem.2011.07.015.

[116] Choi, J. H.; Johnston, C. M.; Cao, D.; Babu, P. K.; Zelenay, P. Se-Modified Ru Nanoparticles as ORR Catalysts: Part 2: Evaluation for Use as DMFC Cathodes. *J. Electroanal. Chem.*, **2011**, *662* (1), 267–273. https://doi.org/10.1016/j.jelechem.2011.07.029.

[117] Morgan, D. J. Resolving Ruthenium: XPS Studies of Common Ruthenium

Materials. *Surf. Interface Anal.*, **2015**, *47* (11), 1072–1079. https://doi.org/10.1002/sia.5852.

[118] Biswal, J.; Ramnani, S. P.; Tewari, R.; Dey, G. K.; Sabharwal, S. Short Aspect Ratio Gold Nanorods Prepared Using Gamma Radiation in the Presence of Cetyltrimethyl Ammonium Bromide (CTAB) as a Directing Agent. *Radiat. Phys. Chem.*, **2010**, *79* (4), 441–445. https://doi.org/10.1016/j.radphyschem.2009.11.004.

[119] Khan, Z.; AL-Thabaiti, S. A.; Obaid, A. Y.; Khan, Z. A.; Al-Youbi, A. A. O. Shape-Directing Role of Cetyltrimethylammonium Bromide in the Preparation of Silver Nanoparticles. *J. Colloid Interface Sci.*, **2012**, *367* (1), 101–108. https://doi.org/10.1016/j.jcis.2011.10.014.

[120] Bakshi, M. S. How Surfactants Control Crystal Growth of Nanomaterials. *Cryst. Growth Des.*, **2016**, *16* (2), 1104–1133. https://doi.org/10.1021/acs.cgd.5b01465.

[121] Yong, K. T.; Sahoo, Y.; Swihart, M. T.; Prasad, P. N. Shape Control of CdS Nanocrystals in One-Pot Synthesis. *J. Phys. Chem. C*, **2007**, *111* (6), 2447–2458. https://doi.org/10.1021/jp066392z.

[122] Harris, R. A.; Shumbula, P. M.; Van Der Walt, H. Analysis of the Interaction of Surfactants Oleic Acid and Oleylamine with Iron Oxide Nanoparticles through Molecular Mechanics Modeling. *Langmuir*, **2015**, *31* (13), 3934–3943. https://doi.org/10.1021/acs.langmuir.5b00671.

[123] Mourdikoudis, S.; Liz-Marzán, L. M. Oleylamine in Nanoparticle Synthesis. *Chem. Mater.*, **2013**, *25* (9), 1465–1476.

https://doi.org/10.1021/cm4000476.

[124] Hinde, C. S.; Ansovini, D.; Wells, P. P.; Collins, G.; Aswegen, S. Van; Holmes, J. D.; Hor, T. S. A.; Raja, R. Elucidating Structure-Property Relationships in the Design of Metal Nanoparticle Catalysts for the Activation of Molecular Oxygen. *ACS Catal.*, **2015**, *5* (6), 3807–3816. https://doi.org/10.1021/acscatal.5b00481.

[125] Pryadchenko, V. V.; Srabionyan, V. V.; Mikheykina, E. B.; Avakyan, L. A.; Murzin, V. Y.; Zubavichus, Y. V.; Zizak, I.; Guterman, V. E.; Bugaev, L. A. Atomic Structure of Bimetallic Nanoparticles in PtAg/C Catalysts: Determination of Components Distribution in the Range from Disordered Alloys to “Core-Shell” Structures. *J. Phys. Chem. C*, **2015**, *119* (6), 3217–3227. https://doi.org/10.1021/jp512248y.

[126] Macarthur, K. E.; Slater, T. J. A.; Haigh, S. J.; Ozkaya, D.; Nellist, P. D.; Lozano-Perez, S. Compositional Quantification of PtCo Acid-Leached Fuel Cell Catalysts Using EDX Partial Cross Sections. *Mater. Sci. Technol. (United Kingdom)*, **2016**, *32* (3), 248–253. https://doi.org/10.1080/02670836.2015.1133021.

[127] Newton, J. E.; Preece, J. A.; Rees, N. V.; Horswell, S. L. Nanoparticle Catalysts for Proton Exchange Membrane Fuel Cells: Can Surfactant Effects Be Beneficial for Electrocatalysis? *Phys. Chem. Chem. Phys.*, **2014**, *16* (23), 11435–11446. https://doi.org/10.1039/c4cp00991f.

[128] Garcia-Ratés, M.; López, N.; Vilé, G.; Pérez-Ramírez, J.; Almora-Barrios, N. Electrochemical Effects at Surfactant-Platinum Nanoparticle Interfaces

Boost Catalytic Performance. *ChemCatChem*, **2016**, *9* (4), 604–609. https://doi.org/10.1002/cctc.201601134.

[129] Sung, Y.-E.; Park, H. Y.; Chung, D. Y.; Chung, Y.-H.; Yoo, S. J.; Jang, J. H.; Kim, S. J. Third-Body Effects of Native Surfactants on Pt Nanoparticle Electrocatalysts in Proton Exchange Fuel Cells. *Chem. Commun.*, **2015**, *51* (14), 2968–2971. https://doi.org/10.1039/c4cc09019e.

[130] Campisi, S.; Schiavoni, M.; Chan-Thaw, C.; Villa, A. Untangling the Role of the Capping Agent in Nanocatalysis: Recent Advances and Perspectives. *Catalysts*, **2016**, *6* (12), 185. https://doi.org/10.3390/catal6120185.

[131] Diroll, B. T.; Murray, C. B.; Gorte, R. J.; Doan-Nguyen, V. V. T.; Cargnello, M.; Chen, C. Efficient Removal of Organic Ligands from Supported Nanocrystals by Fast Thermal Annealing Enables Catalytic Studies on Well-Defined Active Phases. *J. Am. Chem. Soc.*, **2015**, *137* (21), 6906–6911. https://doi.org/10.1021/jacs.5b03333.

[132] Beermann, V.; Gocyla, M.; Kühl, S.; Padgett, E.; Schmies, H.; Goerlin, M.; Erini, N.; Shviro, M.; Heggen, M.; Dunin-Borkowski, R. E.; et al. Tuning the Electrocatalytic Oxygen Reduction Reaction Activity and Stability of Shape-Controlled Pt-Ni Nanoparticles by Thermal Annealing -Elucidating the Surface Atomic Structural and Compositional Changes. *J. Am. Chem. Soc.*, **2017**, *139* (46), 16536–16547. https://doi.org/10.1021/jacs.7b06846.

[133] Chen, H.; Yu, Y.; Xin, H. L.; Newton, K. A.; Holtz, M. E.; Wang, D.; Muller, D. A.; Abruña, H. D.; Disalvo, F. J. Coalescence in the Thermal Annealing of Nanoparticles: An in Situ STEM Study of the Growth Mechanisms of

Ordered Pt-Fe Nanoparticles in a KCl Matrix. *Chem. Mater.*, **2013**, *25* (8), 1436–1442. https://doi.org/10.1021/cm303489z.

[134] Eng, A. Y. S.; Ambrosi, A.; Chua, C. K.; Šaněk, F.; Sofer, Z.; Pumera, M. Unusual Inherent Electrochemistry of Graphene Oxides Prepared Using Permanganate Oxidants. *Chem. - A Eur. J.*, **2013**, *19* (38), 12673–12683. https://doi.org/10.1002/chem.201301889.

[135] Chua, C. K.; Sofer, Z.; Lim, C. S.; Pumera, M. Inherent Electrochemistry of Layered Post-Transition Metal Halides: The Unexpected Effect of Potential Cycling of PbI2. *Chem. - A Eur. J.*, **2015**, *21* (7), 3073–3078. https://doi.org/10.1002/chem.201405204.

[136] Nayak, P.; Jiang, Q.; Mohanraman, R.; Anjum, D.; Hedhili, M. N.; Alshareef, H. N. Inherent Electrochemistry and Charge Transfer Properties of Few-Layered Two-Dimensional Ti 3 C 2 T x MXene . *Nanoscale*, **2018**, *10* (36), 17030–17037. https://doi.org/10.1039/c8nr01883a.

[137] Chia, X.; Adriano, A.; Lazar, P.; Sofer, Z.; Luxa, J.; Pumera, M. Layered Platinum Dichalcogenides (PtS2, PtSe2, and PtTe2) Electrocatalysis: Monotonic Dependence on the Chalcogen Size. *Adv. Funct. Mater.*, **2016**, *26* (24), 4306–4318. https://doi.org/10.1002/adfm.201505402.

[138] Klein, N. D.; Hurley, K. R.; Feng, Z. V.; Haynes, C. L. Dark Field Transmission Electron Microscopy as a Tool for Identifying Inorganic Nanoparticles in Biological Matrices. *Anal. Chem.*, **2015**, *87* (8), 4356–4362. https://doi.org/10.1021/acs.analchem.5b00124.

[139] Thomas, J. M.; Leary, R. K.; Eggeman, A. S.; Midgley, P. A. The Rapidly

Changing Face of Electron Microscopy. *Chem. Phys. Lett.*, **2015**, *631–632*, 103–113. https://doi.org/10.1016/j.cplett.2015.04.048.

[140] Krivanek, O. L.; Lovejoy, T. C.; Dellby, N. Aberration-Corrected STEM for Atomic-Resolution Imaging and Analysis. *J. Microsc.*, **2015**, *259* (3), 165–172. https://doi.org/10.1111/jmi.12254.

[141] Slater, T. J. A.; Lewis, E. A.; Haigh, S. J. Energy Dispersive X-Ray Tomography for 3D Elemental Mapping of Individual Nanoparticles. *J. Vis. Exp.*, **2016**, *113*. https://doi.org/10.3791/52815.

[142] Wang, Y. C.; Engelhard, M. H.; Baer, D. R.; Castner, D. G. Quantifying the Impact of Nanoparticle Coatings and Nonuniformities on XPS Analysis: Gold/Silver Core-Shell Nanoparticles. *Anal. Chem.*, **2016**, *88* (7), 3917–3925. https://doi.org/10.1021/acs.analchem.6b00100.

[143] Ren, J.; Tilley, R. D. Shape-Controlled Growth of Platinum Nanoparticles. *Small*, **2007**, *3* (9), 1508–1512. https://doi.org/10.1002/smll.200700135.

[144] Ren, J.; Tilley, R. D. Preparation, Self-Assembly, and Mechanistic Study of Highly Monodispersed Nanocubes. *J. Am. Chem. Soc.*, **2007**, *129* (11), 3287–3291. https://doi.org/10.1021/ja067636w.

[145] Cheong, S.; Watt, J. D.; Tilley, R. D. Shape Control of Platinum and Palladium Nanoparticles for Catalysis. *Nanoscale*, **2010**, *2* (10), 2045–2053. https://doi.org/10.1039/c0nr00276c.

[146] Cheong, S.; Watt, J.; Ingham, B.; Toney, M. F.; Tilley, R. D. In Situ and Ex Situ Studies of Platinum Nanocrystals: Growth and Evolution in Solution. *J. Am. Chem. Soc.*, **2009**, *131* (40), 14590–14595.

https://doi.org/10.1021/ja9065688.

[147] Jiang, W.; Wang, X.; Chen, Y.; Wu, G.; Ba, K.; Xuan, N.; Sun, Y.; Gong, P.; Bao, J.; Shen, H.; et al. Large-area High Quality PtSe 2 Thin Film with Versatile Polarity . *InfoMat*, **2019**, No. May, 260–267. https://doi.org/10.1002/inf2.12013.

[148] Tilley, R. D.; Gooding, J. J. Electrocatalysis: Understanding Platinum Migration. *Nat. Energy*, **2016**, *1* (11). https://doi.org/10.1038/nenergy.2016.174.

[149] Vitos, L.; Ruban, A. V.; Skriver, H. L.; Kollár, J. The Surface Energy of Metals. *Surf. Sci.*, **1998**, *411* (1–2), 186–202. https://doi.org/10.1016/S0039-6028(98)00363-X.

[150] Suresh, C. H.; Koga, N. A Consistent Approach toward Atomic Radii. *J. Phys. Chem. A*, **2001**, *105* (24), 5940–5944. https://doi.org/10.1021/jp010432b.

[151] Shard, A. G. Detection Limits in XPS for More than 6000 Binary Systems Using Al and Mg K α X-Rays †. *Surf. Interface Anal.*, **2014**, *46* (January), 175–185. https://doi.org/10.1002/sia.5406.

[152] Bazin, D.; Fechete, I.; Garin, F. C.; Barcaro, G.; Negreiros, F. R.; Sementa, L.; Fortunelli, A. Reactivity and Catalysis by Nanoalloys. In *Nanoalloys: From Fundamentals to Emergent Applications*; Elsevier B.V: Amsterdam, 2013; pp 283–344. https://doi.org/10.1016/B978-0-12-394401-6.00009-6.

[153] Yoon, S. B.; Fang, B.; Kim, M.; Kim, J. H.; Yu, J. S. *Nanostructured Supported Catalysts for Low-Temperature Fuel Cells*; Elsevier Ltd, 2009;

Vol. 1. https://doi.org/10.1016/B978-0-08-044965-4.50007-9.

[154] Elgrishi, N.; Rountree, K. J.; McCarthy, B. D.; Rountree, E. S.; Eisenhart, T. T.; Dempsey, J. L. A Practical Beginner's Guide to Cyclic Voltammetry. *J. Chem. Educ.*, **2018**, *95* (2), 197–206. https://doi.org/10.1021/acs.jchemed.7b00361.

[155] Horswell, S. L.; O'Nei, I. A.; Schiffrin, D. J. Kinetics of Electron Transfer at Pt Nanostructured Film Electrodes. *J. Phys. Chem. B*, **2003**, *107* (20), 4844–4854. https://doi.org/10.1021/jp0340257.

[156] Takahashi, I.; Kocha, S. S. Examination of the Activity and Durability of PEMFC Catalysts in Liquid Electrolytes. *J. Power Sources*, **2010**, *195* (19), 6312–6322. https://doi.org/10.1016/j.jpowsour.2010.04.052.

[157] Garsany, Y.; Baturina, O. A.; Swider-Lyons, K. E.; Kocha, S. S. Experimental Methods for Quantifying the Activity of Platinum Electrocatalysts for the Oxygen Reduction Reaction. *Anal. Chem.*, **2010**, *82* (15), 6321–6328. https://doi.org/10.1021/ac100306c.

[158] St-Pierre, J.; Rocheleau, R.; Ge, J.; Garsany, Y.; Swider-Lyons, K. E. Analytical Procedure for Accurate Comparison of Rotating Disk Electrode Results for the Oxygen Reduction Activity of Pt/C. *J. Electrochem. Soc.*, **2014**, *161* (5), F628–F640. https://doi.org/10.1149/2.036405jes.

[159] Kocha, S. S.; Shinozaki, K.; Zack, J. W.; Myers, D. J.; Kariuki, N. N.; Nowicki, T.; Stamenkovic, V.; Kang, Y.; Li, D.; Papageorgopoulos, D. Best Practices and Testing Protocols for Benchmarking ORR Activities of Fuel Cell Electrocatalysts Using Rotating Disk Electrode. *Electrocatalysis*, **2017**,

8 (4), 366–374. https://doi.org/10.1007/s12678-017-0378-6.

[160] Garsany, Y.; Singer, I. L.; Swider-Lyons, K. E. Impact of Film Drying Procedures on RDE Characterization of Pt/VC Electrocatalysts. *J. Electroanal. Chem.*, **2011**, *662* (2), 396–406. https://doi.org/10.1016/j.jelechem.2011.09.016.

[161] Jackson, A.; Viswanathan, V.; Forman, A. J.; Nørskov, J.; Jaramillo, T. F. Effects of a New Electrochemical Cleaning Protocol on Ru@Pt Core-Shell ORR Catalysts. *Electrochem. Soc. Trans.*, **2013**, *58* (1), 929–936.

[162] PerkinElmer, I. *Thermogravimetric Analysis (TGA): A Beginner's Guide*; Waltham, 2010.

[163] Cao, M.; Wu, D.; Cao, R. Recent Advances in the Stabilization of Platinum Electrocatalysts for Fuel-Cell Reactions. *ChemCatChem*, **2014**, *6* (1), 26–45. https://doi.org/10.1002/cctc.201300647.

[164] Newton, J. Nanoparticle Catalysts for Proton Exchange Membrane Fuel Cells : A Study of Surfactant Effects on 111Dispersion and Catalysis. **2014**, No. June.

[165] Monzó, J.; Van Der Vliet, D. F.; Yanson, A.; Rodriguez, P. Elucidating the Degradation Mechanism of the Cathode Catalyst of PEFCs by a Combination of Electrochemical Methods and X-Ray Fluorescence Spectroscopy. *Phys. Chem. Chem. Phys.*, **2016**, *18* (32), 22407–22415. https://doi.org/10.1039/c6cp03795j.

[166] Wang, Z.; Li, Q.; Besenbacher, F.; Dong, M. Facile Synthesis of Single Crystal PtSe 2 Nanosheets for Nanoscale Electronics . *Adv. Mater.*, **2016**,

28 (46), 10224–10229. https://doi.org/10.1002/adma.201602889.

[167] Wang, Y.; Li, L.; Yao, W.; Song, S.; Sun, J. T.; Pan, J.; Ren, X.; Li, C.; Okunishi, E.; Wang, Y. Q.; et al. Monolayer PtSe<inf>2</Inf>, a New Semiconducting Transition-Metal-Dichalcogenide, Epitaxially Grown by Direct Selenization of Pt. *Nano Lett.*, **2015**, *15* (6), 4013–4018. https://doi.org/10.1021/acs.nanolett.5b00964.

[168] Schnepp, Z.; Danks, A. E.; Hollamby, M. J.; Pauw, B. R.; Murray, C. A.; Tang, C. C. In Situ Synchrotron X-Ray Diffraction Study of the Sol-Gel Synthesis of Fe<inf>3</Inf>N and Fe<inf>3</Inf>C. *Chem. Mater.*, **2015**, *27* (14), 5094–5099. https://doi.org/10.1021/acs.chemmater.5b01811.

[169] Kim, B. H.; Yang, J.; Lee, D.; Choi, B. K.; Hyeon, T.; Park, J. Liquid-Phase Transmission Electron Microscopy for Studying Colloidal Inorganic Nanoparticles. *Adv. Mater.*, **2018**, *30* (4), 1–20. https://doi.org/10.1002/adma.201703316.

[170] Wang, Y. J.; Long, W.; Wang, L.; Yuan, R.; Ignaszak, A.; Fang, B.; Wilkinson, D. P. Unlocking the Door to Highly Active ORR Catalysts for PEMFC Applications: Polyhedron-Engineered Pt-Based Nanocrystals. *Energy Environ. Sci.*, **2018**, *11* (2), 258–275. https://doi.org/10.1039/c7ee02444d.

[171] Sassin, M. B.; Garsany, Y.; Gould, B. D.; Swider-Lyons, K. E. Fabrication Method for Laboratory-Scale High-Performance Membrane Electrode Assemblies for Fuel Cells. *Anal. Chem.*, **2017**, *89* (1), 511–518. https://doi.org/10.1021/acs.analchem.6b03005.